LA-6841-T
Thesis

UC-34b

Issued: June 1977

Three-Dimensional Dynamics of Protosteliar Evolution

Thomas Leroy Cook

los alamos
scientific laboratory
of the University of California
LOS ALAMOS, NEW MEXICO 87545

UNITED STATES
ENERGY RESEARCH AND DEVELOPMENT ADMINISTRATION
CONTRACT W-7405-ENG. 36

This thesis was submitted to the Rice University, Houston, Texas, in partial fulfillment of the requirements for the degree of Doctor of Philosophy. It is the independent work of the author and has not been edited by the Technical Information staff.

Printed in the United States of America. Available from
National Technical Information Service
U.S. Department of Commerce
5285 Port Royal Road
Springfield, VA 22161
Price: Printed Copy $9.25 Microfiche $3.00

CONTENTS

TABLES

FIGURES

DEFINITION OF THE PHYSICAL PARAMETERS

r	radial coordinate
θ	azimuthal coordinate
z	axial coordinate
t	time
u	radial component of velocity
v	azimuthal component of velocity
w	axial component of velocity
V_r	radial component of the divergence of the viscous stress tensor
V_θ	azimuthal component of the divergence of the viscous stress tensor
V_z	axial component of the divergence of the viscous stress tensor
ρ	density
ψ	gravitational potential
p	pressure
ω	instantaneous angular velocity of rotating frame
A	entropy variable
I	specific internal energy
γ	ratio of specific heats
μ	bulk viscosity coefficient
ν	kinematic viscosity coefficient
λ	second viscosity coefficient; only in Eq. (II-9)
λ	free-scaling parameter
Λ	normalization parameter
Γ	dimensionless stability parameter
R	radius of toroid from central axis
a	characteristic cross-sectional radius of toroid
t_f	free-fall time

M	total mass
ρ'_{max}	interpolated maximum density
$R_{\rho'_{max}}$	radial position of ρ'_{max}
ρ_{max}	maximum cell density
$R_{\rho_{max}}$	radial position of ρ_{max}
W	total gravitational potential energy
KE	total kinetic energy of radial and axial motion
U	total internal energy
T	total rotational kinetic energy
E	total energy
J	total angular momentum
Θ	temperature
n_p	polytropic index

ABSTRACT

Three-Dimensional Dynamics of Protostellar Evolution

by

Thomas Leroy Cook

A three-dimensional finite difference numerical methodology has been developed for self-gravitating, rotating gaseous systems. The fully nonlinear equations for time-varying fluid dynamics are solved by high-speed computer in a cylindrical coordinate system rotating with an instantaneous angular velocity, selected such that the net angular momentum relative to the rotating frame is zero.

The time-dependent adiabatic collapse of gravitationally bound, rotating, protostellar clouds is studied for specified uniform and nonuniform initial conditions. Uniform clouds can form axisymmetric, rotating toroidal configurations. If the thermal pressure is high, nonuniform clouds can also collapse to axisymmetric toroids. For low thermal pressures, however, the collapsing cloud is unstable to initial perturbations.

The fragmentation of protostellar clouds is investigated by studying the response of rotating, self-gravitating, equilibrium toroids to non-axisymmetric perturbations. The detailed evolution of the fragmenting toroid depends upon a non-dimensional function of the initial entropy, the total mass in the toroid, the angular velocity of rotation, and the number of perturbation wavelengths around the circumference of the toroid. For low and intermediate entropies, the configuration

develops into co-rotating components with spiral streamers. In the spiral regions retrograde vortices are observed in some examples. For high levels of entropy, barred spirals can exist as intermediate states of the fragmentation.

I. INTRODUCTION

A. BINARY STARS

1. Historical Background

The Greek equivalent of the term *double star* was first used by Ptolemy to describe the appearance of γ Sagittarii.[1] Many double stars are optical pairs rather than true binary systems. In 1767 Rev. John Michell read a paper[2] before the Royal Society in London in which he presented a statistical argument suggesting that many of the double stars then known were the result of physical rather than optical association. His controversial paper prompted astronomers to intensify their search for double stars. In an address to the Royal Society in 1802, Sir William Herschel first used the term *binary star* to designate the physical union of two stars in one system.[3]

The first known observation of a *close binary* (e.g., component separation comparable in magnitude to component dimensions) may date back to the days of nomadic life in the Arabian peninsula.[4] The second brightest star in the constellation of Perseus was given the name *Al Ghūl*, which means "changing spirit." Although it is questionable whether one should assign any specific significance to the name, it is appropriate because Algol, as it is now called, is an eclipsing binary. In 1783 John Goodricke, Junior, made the first observations of a minimum of Algol and successfully measured its periodicity. He even conjectured that it might be an eclipsing double star system in which the components were physically bound.[5]

2. Significance

Conservative estimates indicate that 30 to 50% of the total star population in the vicinity of the solar system occurs in double or multiple systems.[6] Approximately .2% of these stars are eclipsing binaries.[7] If one considers the random distribution of orbital inclinations, approximately 1% of the stars may be in close binary systems. This argument implies that if a similar ratio holds for our galactic system as a whole, one might expect it to contain some 10^9 close binaries.

The astrophysical data that can be deduced from a study of eclipsing binary systems provide the theoretician with a method for looking into the very heart of stars. For a single star one has no way of gauging its external gravitational field or of learning anything about the distribution of its surface brightness. In close binaries, however, the properties of the combined gravitational field can be deduced from the characteristics of the motion. Knowing the gravitational field one can then check calculational models of internal pressure and density distributions. The variation of brightness caused by axial rotation of the distorted components or exhibited during their mutual eclipses permits one to measure the distribution of surface brightness. Non-radial tidal oscillations can demonstrate whether stellar configurations behave like perfect fluids.[8] These considerations and others demonstrate the important role that multiple star systems play in our understanding of astrophysical phenomena.

The theoretical complexities associated with the interpretation of data produced from such observations are non-trivial. Previous work has employed complicated models of the material properties and

and transport processes believed to be operative and has generally made extremely simplifying assumptions regarding the dynamics of the motion. The present work emphasizes the solution of the nonlinear dynamics while using less detailed models of the other physical processes. In the following chapters a fully three-dimensional finite difference methodology is developed specifically for application to rapidly rotating, highly distorted, self-gravitating binary systems.

B. PROTOSTARS

1. Early Stages of Star Formation

In 1692 Newton suggested that stars might form through gravitational condensation of diffuse matter in space. Although Newton's idea is widely accepted as being basically correct, many details of star formation remain highly speculative and controversial. The earliest stages of the star formation process are less well understood than the intermediate collapse stages. Thermal and magnetic instabilities as well as large scale galactic shock have been proposed as possible mechanisms through which interstellar clouds are formed of sufficient mass and density to be gravitationally bound.[10] Once a cloud is gravitationally bound it is called a protostar. It is at this point in the evolution that our investigation begins. A comprehensive review of this theory of the early stages of star formation is given by Spitzer,[11, 12] and shorter discussions are provided by Field[13] and Penston.[14] A somewhat different point of view is presented by McNally.[15]

If a cloud is to condense into a star or a cluster of stars, its self-gravity must exceed the forces working to disperse it. The principle dispersive mechanisms include

1) thermal gas pressure

2) magnetic pressure

3) centrifugal force if the cloud is rotating

4) the effects of internal turbulent motions

For simplicity one generally neglects the magnetic pressure and includes the turbulent effects as an added thermal pressure. Spitzer[16] states and derives the Jeans criterion in a number of ways; however, Larson[17] proposes the following succinct statement:

"In essence, the Jeans criterion simply states that in order for collapse to occur, the gravitational potential energy of a cloud must be comparable to or greater than the kinetic energy of thermal or turbulent motions within the cloud."

For a rotating cloud one makes a modification in the above statement to allow for the inclusion of the rotational kinetic energy as a dispersive mechanism.

2. Collapsing Protostars

a. Spherical models

In recent years a large number of authors have calculated the early stages of the collapse of a spherically symmetric, nonrotating gas cloud.[18-22] A brief review of these studies is given by Penston.[23] Although the various calculations are based upon assumptions that are considerably different from one another, there is remarkable agreement on the qualitative features of the collapse. For example the collapse is always found to be very nonhomologous, and the density distribution becomes very rapidly peaked at the center.[24]

To better understand the nature of the collapse one can consider the free fall time of a uniform density, zero pressure spheroid given

below.[25]

$$t_f = \left(\frac{3\pi}{32G\rho}\right)^{\frac{1}{2}} \qquad (I\text{-}1)$$

The free fall time varies inversely as the square root of the density. Therefore, as the local density increases, its free fall time decreases; and the collapse around a local center of condensation proceeds more rapidly than in the more diffuse regions of the cloud, producing a separation of the material into a central condensed region that is well separated from the outer regions of the cloud. If the system were not spherically symmetric, the resulting configuration would be strongly unstable, leading therefore to fragmentation.

b. Axisymmetric models

If the system is rotating, the most restrictive assumption in the above is the spherical symmetry constraint. In 1972 Larson[26] reported two-dimensional calculations in which he imposed only axial symmetry on the collapse. For the purposes of this present investigation it is useful to emphasize two of his conclusions. First, since one does not know what initial conditions and boundary conditions are appropriate for a condensing protostar, it is reassuring that Larson finds the qualitative features of the late time collapse to be insensitive to these details.[27] Second, Larson finds that in the presence of rapid rotation the central portion of the cloud always appears to condense into a rotating toroid with a density minimum at the center.

The formation of such a ring is physically reasonable, as demonstrated by the following scenario. Depending on the rate of rotation, central densities may or may not increase at first as the collapse proceeds. In either case conservation of angular momentum

requires that the azimuthal velocity of the material falling toward the axis of rotation increase; and eventually, the centrifugal forces exceed the forces of gravity. In the central regions the equatorial collapse near the axis of rotation ceases. Collapse along the axis of rotation continues unimpeded toward the center and finally rebounds outward into the equatorial plane. At the same time material from the outer part of the cloud continues to fall inward and to accumulate in a ring-shaped torois around the central region where collapse has been halted. Once the ring has formed, it becomes a center of accretion for the remaining inward falling material.

Subsequent to Larson's pioneering work two similar two-dimensional numerical studies have been published. Tscharnuter[29] has repeated the work of Larson using a different numerical scheme, and he has not found ring formation. His results indicate that for rapid rotation the cloud reexpands after the initial collapse. Black and Bodenheimer,[30] on the other hand, have also published calculations treating rapidly rotating collapsing protostars, and they obtain rotating toroids qualitatively similar to those of Larson.

To follow the collapse further one must study the fragmentation of these rotating toroids. The full three-dimensional equations of motion must therefore be solved. It is this aspect of protostellar evolution that forms the central theme of this research.

c. Additional models

The numerical work described above has not been the only source nor has it been the primary source suggesting the existence of rings in the universe. Modern observations show that rings commonly occur in spiral galaxies of both the ordinary and barred types.[31, 32]

Minkowski and Osterbrock[33] have observed rings in certain planetary nebulae. Underhill[34] mentions rings as possible models for the extended atmospheres of early-type stars, and Maltby and Moffet[35] suggest ring models in their extragalactic radio source studies.

The earliest work[36] on the theory of equilibrium rings dates back to Laplace (1789). Contributions have also been made by Maxwell[37] and Poincaré.[38] The comprehensive treatment of the equilibrium and stability of fluid rings by Dyson[39] in 1893 essentially completes this class of studies, which can be characterized by the following assumptions.

1) slender rings; i.e., minor axis < < major axis
2) uniform rotation
3) homogeneous liquid rings

In his 1964 study of equilibrium rings Ostriker[40] replaces the third and most restrictive assumption (liquid rings) with the requirement that the fluid be a polytropic gas. He finds that for certain mass-to-length ratios stable toroidal configurations should exist. Larson and Black and Bodenheimer find values of this ratio in their respective works that agree fairly well with the predictions of Ostriker.

C. THE PRESENT THREE-DIMENSIONAL MODEL

1. Basic Approach

The next improvement one might naturally make in the numerical studies of collapsing protostars is the extention to large amplitude non-axisymmetric motions. Most of the authors cited above comment that nothing definitive can really be concluded until one has investigated the stability of rotating toroids subjected to large non-axisymmetric perturbations. As is often the case, however, the most

obvious improvement is not always the easiest to implement. In this situation one must have access to the largest, fastest computers available today; and in addition one must develop a methodology made possible only through modern techniques in numerical fluid dynamics.

In order to facilitate the development of a fully three-dimensional numerical fluid dynamics capability for application to rotating, self-gravitating bodies, one chooses, at least initially, to simplify the models of the physical processes to the greatest possible degree while maintaining contact with reality. Such an approach also allows one to develop a thorough understanding of the methodology, which will prove useful as the complexity of the physical modelling progresses. With this motivation in mind, the following assumptions are made in the work described in this text.

1) adiabatic fluid motions
2) negligible physical viscosity
3) polytropic gases
4) no radiation effects
5) no electromagnetic effects

The first assumption permits one to avoid solving an energy equation. In the absence of strong sources and sinks, as is the case for the early stages of protostellar evolution, it is a reasonable constraint. The negligible physical viscosity assumption is likewise reasonable for the diffuse distributions involved here. Polytropic gas equations of state have been used rather successfully in many astrophysical applications over a wide range of densities. For a general discussion one is referred to texts such as those by Clayton[41]

and Chandrasekhar.[42] Larson and Black and Bodenheimer include radiation pressure in their respective calculations and find that this term is negligible over the range of densities occuring in this phase of protostar development. Each of the above assumptions can be replaced by more complicated modelling of the physical processes.

The fifth assumption can not be so easily dismissed. Because of the mathematical complexities involved, the possible role of frozen-in magnetic fields in collapsing clouds remains one of the principal unsolved problems in the theory of star formation.[43] During early stages of the collapse the field is thought to be frozen into the gas because of the ionization produced by high energy cosmic rays. However, as the density increases the cloud becomes optically thick to such radiation; and the ionization decreases, decoupling the cloud from the magnetic field.[44] Observations of magnetic field strengths in interstellar clouds are generally consistent with the hypothesis of the frozen-in field.[45] However, some dense clouds have magnetic fields that are much weaker than one would expect;[46] and in the dense Taurus dust cloud, a region of active star formation, no magnetic field has yet been detected.[47]

2. Numerical Solution of the Model Equations

KORYO is a three-dimensional Eulerian computer code designed to solve the equations of motion for rotating, self-gravitating fluids. The equations are written in cylindrical coordinates, and the plane at $z = 0$ is assumed to be a plane of symmetry. Densities and pressu are treated implicitly. Donor-cell fluxes are used throughout with the fluxes in the azimuthal direction being convected relative to a

frame rotating with an instantaneous angular velocity selected so that the net angular momentum relative to it is zero. A central core boundary region avoids pie-shaped cells and the resulting severe time step restrictions. Mass is allowed to leave the system through the outer radial boundary. To obtain the gravitational potential at each instant in time, Poisson's equation is relaxed iteratively. These characteristics of the methodology and others are developed in detail in Chapter III.

II. THEORY AND PROCEDURE

A. EQUATIONS OF FLUID DYNAMICS

1. Equation of Continuity

The motion and general behavior of the fluid are governed by the fundamental laws of mechanics and thermodynamics. The equation of continuity is developed by applying the law of conservation of mass to a small volume element within a moving fluid.[48] For a compressible fluid this equation takes the following form in cylindrical coordinates.[49]

$$\frac{\partial \rho}{\partial t} + \frac{1}{r}\frac{\partial \rho u r}{\partial r} + \frac{1}{r}\frac{\partial \rho v}{\partial \theta} + \frac{\partial \rho w}{\partial z} = 0 \quad . \tag{II-1}$$

2. Equations of Motion

a. Non-conservative form

The equations expressing the conservation of momentum are derived in a similar fashion.[50] For a fluid system moving under its own self-gravity, the components of the body forces in the equations are the respective gradients of the gravitational potential. Incorporating these and the other forces the equations in cylindrical coordinates[51] for a rotating, self-gravitating fluid system are customarily written

$$\rho\frac{\partial u}{\partial t} + \rho\left(u\frac{\partial u}{\partial r} + \frac{v}{r}\frac{\partial u}{\partial \theta} + w\frac{\partial u}{\partial z} - \frac{v^2}{r}\right) = -\rho\frac{\partial \psi}{\partial r} - \frac{\partial p}{\partial r} + V_r \tag{II-2}$$

$$\rho\frac{\partial v}{\partial t} + \rho\left(u\frac{\partial v}{\partial r} + \frac{v}{r}\frac{\partial v}{\partial \theta} + w\frac{\partial v}{\partial z} + \frac{uv}{r}\right) = -\frac{\rho}{r}\frac{\partial \psi}{\partial \theta} - \frac{1}{r}\frac{\partial p}{\partial \theta} + V_\theta \tag{II-3}$$

$$\rho\frac{\partial w}{\partial t} + \rho\left(u\frac{\partial w}{\partial r} + \frac{v}{r}\frac{\partial w}{\partial \theta} + w\frac{\partial w}{\partial z}\right) = -\rho\frac{\partial \psi}{\partial z} - \frac{\partial p}{\partial z} + V_z \quad . \tag{II-4}$$

The viscous stress components will be discussed below in conjunction with the physical viscosities.

b. Conservative form

The convective parts of the momentum equations given above are not written in conservative form. They should be expressed such that if one integrates over the total volume of the fluid, the change with time of any conserved quantity is just equal to the net gain or loss of that quantity through the boundaries. Multiplying Eq. (II-1) by the radial velocity and adding the result to the momentum equation, one obtains

$$\frac{\partial \rho u}{\partial t} + \frac{1}{r}\frac{\partial \rho u^2 r}{\partial r} + \frac{1}{r}\frac{\partial \rho uv}{\partial \theta} + \frac{\partial \rho uw}{\partial z} = \frac{\rho v^2}{r} - \rho \frac{\partial \psi}{\partial r} - \frac{\partial p}{\partial r} + V_r \ . \qquad \text{(II-5)}$$

This expression is the form of the radial momentum equation that furnishes the basis for the calculations presented in this paper. Equations (II-3) and (II-4) can be altered in an exactly analogous fashion to yield

$$\frac{\partial \rho v}{\partial t} + \frac{1}{r^2}\frac{\partial \rho uvr^2}{\partial r} + \frac{1}{r}\frac{\partial \rho v^2}{\partial \theta} + \frac{\partial \rho vw}{\partial z} = -\frac{\rho}{r}\frac{\partial \psi}{\partial \theta} - \frac{1}{r}\frac{\partial p}{\partial \theta} + V_\theta \qquad \text{(II-6)}$$

and

$$\frac{\partial \rho w}{\partial t} + \frac{1}{r}\frac{\partial \rho uwr}{\partial r} + \frac{1}{r}\frac{\partial \rho vw}{\partial \theta} + \frac{\partial \rho w^2}{\partial z} = -\rho \frac{\partial \psi}{\partial z} - \frac{\partial p}{\partial z} + V_z \ . \qquad \text{(II-7)}$$

The specific form of Eq. (II-6) combines the coriolis and convective terms in a manner that is conservative of angular momentum as discussed in Appendix B.

c. Viscous stress component

If adjacent layers of a fluid are in relative motion, a shear stress can develop. The constant of proportionality between the shear stress

and the velocity gradient is called the first viscosity. Since the fluid is compressible another viscous stress, which is proportional to the volumetric change, can arise. The proportionality coefficient for this stress is called the second or the bulk viscosity.[52] The viscous stress components for a compressible fluid are expressed in cylindrical coordinates as follows.[53]

$$V_r = \frac{\partial}{\partial r}\left[2\mu\frac{\partial u}{\partial r} + \lambda\left(\frac{1}{r}\frac{\partial ru}{\partial r} + \frac{1}{r}\frac{\partial v}{\partial \theta} + \frac{\partial w}{\partial z}\right)\right]$$
$$+ \frac{2\mu}{r}\left(\frac{\partial u}{\partial r} - \frac{u}{r} - \frac{1}{r}\frac{\partial v}{\partial \theta}\right) + \frac{1}{r}\frac{\partial}{\partial \theta}\left[\mu\left(\frac{\partial v}{\partial r} + \frac{1}{r}\frac{\partial u}{\partial \theta} - \frac{v}{r}\right)\right]$$
$$+ \frac{\partial}{\partial z}\left[\mu\left(\frac{\partial u}{\partial z} + \frac{\partial w}{\partial r}\right)\right] \qquad \text{(II-8)}$$

$$V_\theta = \frac{1}{r}\frac{\partial}{\partial \theta}\left[\frac{2\mu}{r}\frac{\partial v}{\partial \theta} + \lambda\left(\frac{1}{r}\frac{\partial ru}{\partial r} + \frac{1}{r}\frac{\partial v}{\partial \theta} + \frac{\partial w}{\partial z}\right)\right]$$
$$+ \frac{\partial}{\partial z}\left[\mu\left(\frac{1}{r}\frac{\partial w}{\partial \theta} + \frac{\partial v}{\partial z}\right)\right] + \frac{\partial}{\partial r}\left[\mu\left(\frac{\partial v}{\partial r} + \frac{1}{r}\frac{\partial u}{\partial \theta} - \frac{v}{r}\right)\right]$$
$$+ \frac{2\mu}{r}\left(\frac{\partial v}{\partial r} + \frac{1}{r}\frac{\partial u}{\partial \theta} - \frac{v}{r}\right) + \frac{2}{r^2}\frac{\partial \mu u}{\partial \theta} \qquad \text{(II-9)}$$

$$V_z = \frac{\partial}{\partial z}\left[2\mu\frac{\partial w}{\partial z} + \lambda\left(\frac{1}{r}\frac{\partial ru}{\partial r} + \frac{1}{r}\frac{\partial v}{\partial \theta} + \frac{\partial w}{\partial z}\right)\right]$$
$$+ \frac{1}{r}\frac{\partial}{\partial r}\left[r\mu\left(\frac{\partial u}{\partial z} + \frac{\partial w}{\partial r}\right)\right] + \frac{1}{r}\frac{\partial}{\partial \theta}\left[\mu\left(\frac{1}{r}\frac{\partial w}{\partial \theta} + \frac{\partial v}{\partial z}\right)\right]. \qquad \text{(II-10)}$$

The viscosity effects are negligible in the physical systems that are studied in this work. Nevertheless, for the incorporation of adequate dissipation in the numerical solutions, one has used a simplified model for the viscous stress components. The basis for the particular form is discussed in the numerical stability section of Chapter III. In

differential form these components are the following

$$V_r \equiv \nu \left[\frac{\partial}{\partial r} \left(\frac{\rho}{r} \frac{\partial ru}{\partial r} \right) + \frac{1}{r^2} \frac{\partial}{\partial \theta} \left(\rho \frac{\partial u}{\partial \theta} \right) - \frac{2\rho}{r^2} \frac{\partial v}{\partial \theta} + \frac{\partial}{\partial z} \left(\rho \frac{\partial u}{\partial z} \right) \right] \tag{II-11}$$

$$V_\theta \equiv \nu \left\{ \frac{1}{r^2} \frac{\partial}{\partial r} \left[\rho r^2 \left(\frac{\partial v}{\partial r} - \frac{v}{r} \right) \right] + \frac{1}{r^2} \left[\frac{\partial}{\partial \theta} \left(\rho \frac{\partial v}{\partial \theta} \right) + 2 \frac{\partial \rho u}{\partial \theta} \right] + \frac{\partial}{\partial z} \left(\rho \frac{\partial v}{\partial z} \right) \right\} \tag{II-12}$$

$$V_z \equiv \nu \left[\frac{1}{r} \frac{\partial}{\partial r} \left(\rho r \frac{\partial w}{\partial r} \right) + \frac{1}{r^2} \frac{\partial}{\partial \theta} \left(\rho \frac{\partial w}{\partial \theta} \right) + \frac{\partial}{\partial z} \left(\rho \frac{\partial w}{\partial z} \right) \right] \tag{II-13}$$

It is important to note that the density has been put into Eq. (II-12) in such a way as to maintain the conservative form; so that linear and angular momentum are neither gained nor lost.

3. The Equation of State

Contained within the four conservation equations, Eqs. (II-1), (II-2), (II-3), and (II-4), one has six unknowns. Two more equations are therefore needed to solve the system. One additional equation is provided by the equation of state of the fluid. The equation of state is usually expressed as some function relating pressure, density, and temperature. For an adiabatic system one has merely to connect the pressure and the density as for example in the polytropic equation of state.

$$p = A \rho^\gamma \tag{II-14}$$

For the reasons discussed in Chapter I one uses this very simplified description of the material in the present study.

B. GRAVITATIONAL POTENTIAL

Self-gravity provides the "container" for the fluids of astrophysics. The final equation needed to form a complete set is provided by Poisson's equation relating the gravitational potential to the fluid configuration. In cylindrical coordinates one has

$$\frac{1}{r}\frac{\partial}{\partial r}\left(r\frac{\partial \psi}{\partial r}\right) + \frac{1}{r^2}\frac{\partial^2 \psi}{\partial \theta^2} + \frac{\partial^2 \psi}{\partial z^2} = 4\pi G \rho \quad . \tag{II-15}$$

Many attempts have been made to construct models of rotating, self-gravitating bodies. In cases dealing with compressible masses almost every attempt has involved a series expansion of ψ in Legendre polynomials to account for departures from spherical symmetry.[54] These methods suffer from the uncertainties of truncating series and products of series after a finite number of terms.

The present work uses a finite difference approach, but avoids matrix inversion complexities[55] by relaxing Poisson's equation iteratively (Chapter III) subject to the boundary conditions at each boundary point $(r_\ell, \theta_\ell, z_\ell)$, calculated by performing a numerical integration over all mass points (r_m, θ_m, z_m).

$$\psi(r_\ell, \theta_\ell, z_\ell) = \iiint \frac{-\rho(r_m, \theta_m, z_m)\, r_m \, dr\, d\theta\, dz}{\left[r_\ell^2 + r_m^2 - 2 r_\ell r_m \cos|\theta_\ell - \theta_m| + (z_\ell - z_m)^2\right]^{\frac{1}{2}}} \tag{II-16}$$

C. ROTATING REFERENCE FRAME

1. Coordinate Transformations

The evolution of rapidly rotating asymmetric self-gravitating bodies can be most accurately studied with numerical techniques in a reference frame that is itself rotating with the average angular velocity of the system. Otherwise one would have a high mass transport through the calculational grid, resulting in the introduction of large diffusional effects. In a properly selected rotating frame the transport due solely to the rotation of the system is minimized. A further reason for choosing to work in a rotating frame is suggested by the nature of the iterative method used to relax Poisson's equation for the gravitational potential. If the mass motion relative to the calculational mesh is small, the convergence of the numerical solution is much more efficient.

The transformations to a frame (indicated by primes) rotating with the instantaneous angular velocity, ω, are given as follows.

$$\begin{aligned} r &= r' \\ \theta &= \theta' + \omega t' \\ z &= z' \\ t &= t' \end{aligned} \qquad \text{(II-17)}$$

so that

$$\begin{aligned} \frac{\partial}{\partial t} &= \frac{\partial}{\partial t'} - \omega \frac{\partial}{\partial \theta'} \\ \frac{\partial}{\partial r} &= \frac{\partial}{\partial r'} \\ \frac{\partial}{\partial \theta} &= \frac{\partial}{\partial \theta'} \end{aligned} \qquad \text{(II-18)}$$

$$\frac{\partial}{\partial z} = \frac{\partial}{\partial z'}$$

where

$$\omega \equiv \omega(t) \quad .$$

In the following section the primes are dropped from the independent variables. The value of ω is determined so that the instantaneous angular momentum of the system is zero in the rotating frame.

2. Transformed Equations

The transformations must now be applied to the equation of continuity, the momentum equations, and the Poisson equation. Using Eq. (II-18) to transform Eqs. (II-1), (II-5), (II-6), and (II-7) and rearranging so that the resulting expressions are conservative, one has

$$\frac{\partial \rho}{\partial t} + \frac{1}{r}\frac{\partial \rho u r}{\partial r} + \frac{1}{r}\frac{\partial \rho(v - r\omega)}{\partial} + \frac{\partial \rho w}{\partial z} = 0 \qquad \text{(II-19)}$$

$$\frac{\partial \rho u}{\partial t} + \frac{1}{r^2}\frac{\partial \rho u^2 r}{\partial r} + \frac{1}{r}\frac{\partial \rho u(v - r\omega)}{\partial \theta} + \frac{\partial \rho u w}{\partial z} = \frac{\rho v^2}{r} - \rho\frac{\partial \psi}{\partial r} - \frac{\partial p}{\partial r} + V_r \qquad \text{(II-20)}$$

$$\frac{\partial \rho v}{\partial t} + \frac{1}{r^2}\frac{\partial \rho u v r^2}{\partial r} + \frac{1}{r}\frac{\partial \rho v(v - r\omega)}{\partial \theta} + \frac{\partial \rho v w}{\partial z} = -\frac{\rho}{r}\frac{\partial \psi}{\partial \theta} - \frac{1}{r}\frac{\partial p}{\partial \theta} + V_\theta \qquad \text{(II-21)}$$

$$\frac{\partial \rho w}{\partial t} + \frac{1}{r}\frac{\partial \rho u w r}{\partial r} + \frac{1}{r}\frac{\partial \rho w(v - r\omega)}{\partial \theta} + \frac{\partial \rho w^2}{\partial z} = -\rho\frac{\partial \psi}{\partial z} - \frac{\partial p}{\partial z} + V_z \quad . \qquad \text{(II-22)}$$

Poisson's equation and the viscous stress terms remain unchanged under the transformation. It is important to emphasize that the azimuthal velocity appearing above is referred to the rest frame. Nevertheless the azimuthal convection takes place at a rate proportional to the net velocity of the fluid relative to the rotating frame, thereby reducing the net convection of the fluid to a minimum.

D. LIMITATIONS OF THE COORDINATE SYSTEM

For solving problems in a rotating frame it is valuable to use a fully three-dimensional cylindrical coordinate system. To visualize the restrictions imposed on the studies by such a coordinate system, one can first imagine that the investigations are confined to a cylindrical annulus; that is, a central core region has been excluded from the coordinate system along the z-axis. For such a region it is of course necessary to supply boundary conditions at every point on the confining surface. In contrast, the investigation of the dynamics in a Cartesian system would be free from the specification of boundary conditions along the inner region defined by the core. As a result the Cartesian calculations would allow for a general class of motions (e.g., those passing through the axis) that are precluded by the choice of a cylindrical system. Although this limitation is somewhat restrictive, it will become evident that for the large class of problems of interest in this research effort, the advantages of the cylindrical coordinate system are decissive.

In the discussion of the numerical solution techniques, it will emerge that the definition of a small central core is of great convenience with little resulting sacrifice of physical reality. In addition, we have chosen a class of problems at this stage of the investigation for which there is perfect symmetry across the equatorial plane. The

boundary conditions that represent the configuration of our domain of study are described as follows:

1) On the equatorial plane and on the core boundary, the normal velocity vanishes; and the normal derivative of any velocity is calculated from the requirement of vanishing viscous stress.

2) On the top and lateral boundaries the normal derivatives of the velocities are also determined by the condition of vanishing viscous stress. The normal component of velocity, however, is specified in such a way as to allow for the convective loss of mass in those circumstances in which appreciable mass loss results from explosive expansion and/or the necessity to expel excess angular momentum.

III. NUMERICAL METHODOLOGY

A. INTRODUCTION

The equations of motion are solved by the finite difference techniques developed in this chapter. To proceed one must decide on

1) the appropriate finite difference approximation to the equations of motion
2) the proper representation of the fluid within the context of these finite difference approximations
3) the establishment of a logical procedure for developing the appropriate solutions from prescribed initial conditions.

The first question is handled in the discussions that follow of how to represent various terms in the equations. The second question is answered by defining the calculational mesh. The third point is discussed in terms of a subdivision of time into a sequence of steps counted by the index n and of each step into a sequence of phases treating different parts of the necessary logic for the time advancement. Phase 2 of each cycle consists of an iterative process that requires an initial guess and that uses a corrective process to lead to convergence. Because of the way the variables appear in the equations of motion, the finite difference formulation can be termed implicit, and it is because of this implicit formulation that an iterative solution procedure is required. These ideas are further developed and expanded in the remainder of this chapter.

B. CALCULATIONAL MESH

KORYO is designed for the study of three-dimensional problems in cylindrical coordinates. The calculational mesh is described graphically by the two mutually perpendicular planes in Fig. 1. In Fig. 1a, one sees an r-θ slice perpendicular to the z-axis. The inner boundary

consists of a core of cells removed from the mesh to avoid the radial singularity as $r \to 0$. Figure 1b is a representation of an r-z plane. The cell size along any given coordinate is constant. The integer indices (i, j, k) define the cell centers while the half-integer indices ($i\pm\frac{1}{2}$, $j\pm\frac{1}{2}$, $k\pm\frac{1}{2}$) denote cell interfaces. The i index increases with increasing r; the j index, with increasing θ; and the k index, with increasing z.

A typical zone is enlarged in Fig. 2, and the centering of the variables is indicated. Densities, pressures, and scalar gravitational potentials are cell-centered quantities. The radial, azimuthal, and axial velocities and the r, θ, and z coordinates are interface variables.

CALCULATIONAL MESH

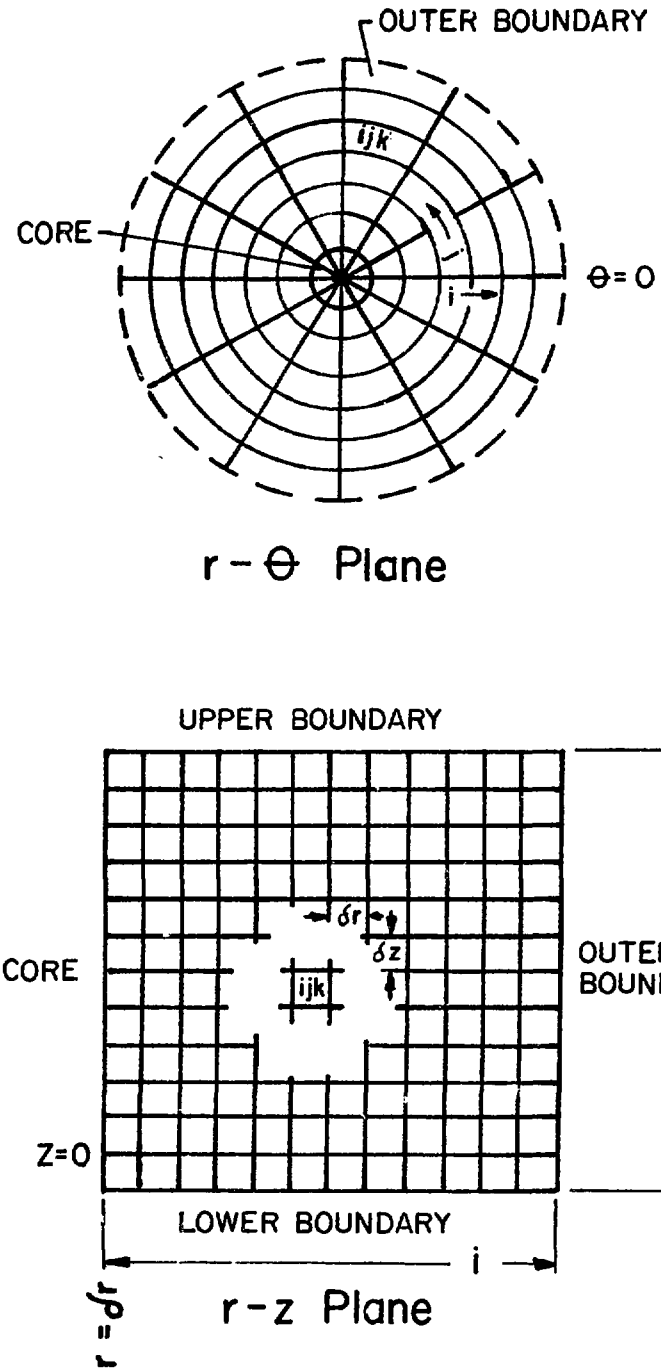

FIGURE 1

VARIABLE CENTERING

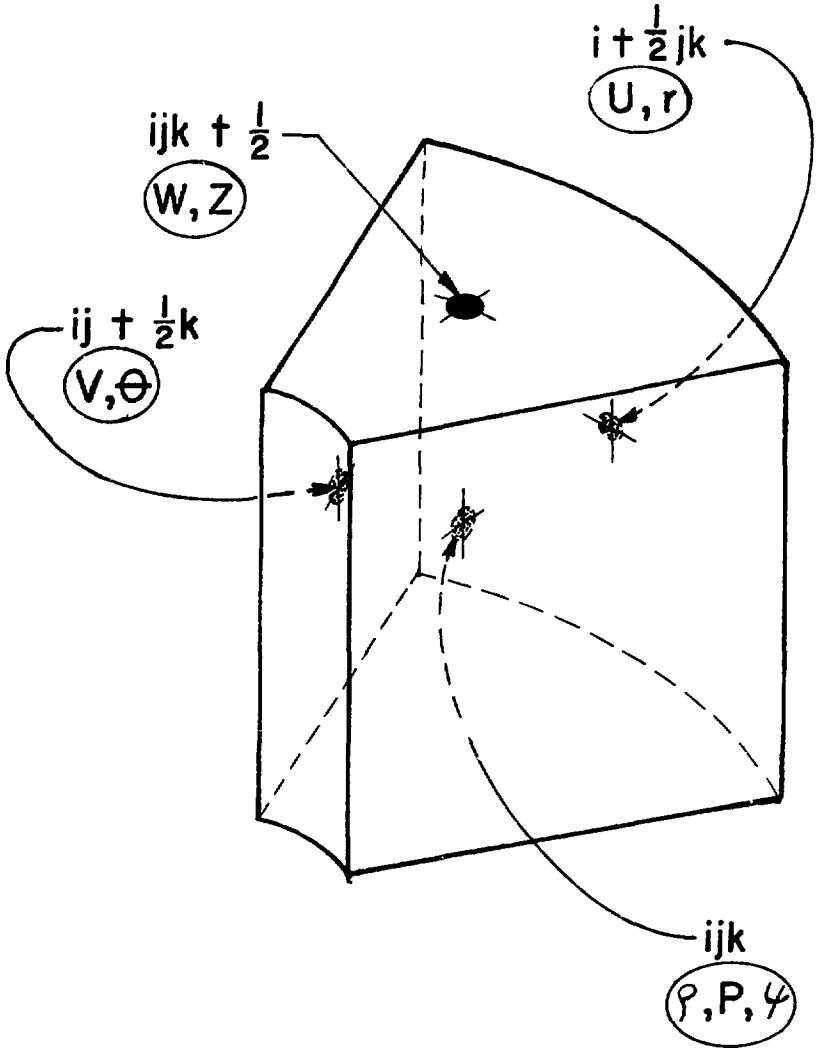

FIGURE 2

C. CALCULATIONAL SEQUENCE

The manner in which the variables are advanced in value from one computational cycle to the next is summarized schematically in Fig. 3. The gravitational potential for each cell to be used in advancing the other dependent variables to time cycle number n+1 are calculated at the beginning of each cycle, based on the mass distribution at time n. Given the scalar potential field at time n, the phase 1 portion of the calculation is commenced. In this section the so-called "bar" quantities are calculated. The "bar" quantities serve as initial guesses, when the pressure gradients are added, for the iterative solution of the axial, azimuthal and radial momenta of each cell at the next time level. In phase 2 of the calculation one solves for the pressures, the densities, and the three components of momentum by an iterative procedure.

Finally, in phase 3 the axial, azimuthal and radial velocities are separated from their respective momenta. The new average angular velocity of the system is determined in such a way as to reduce the average angular momentum relative to a rotating frame to zero. The entire cycle is then repeated.

CALCULATIONAL SEQUENCE

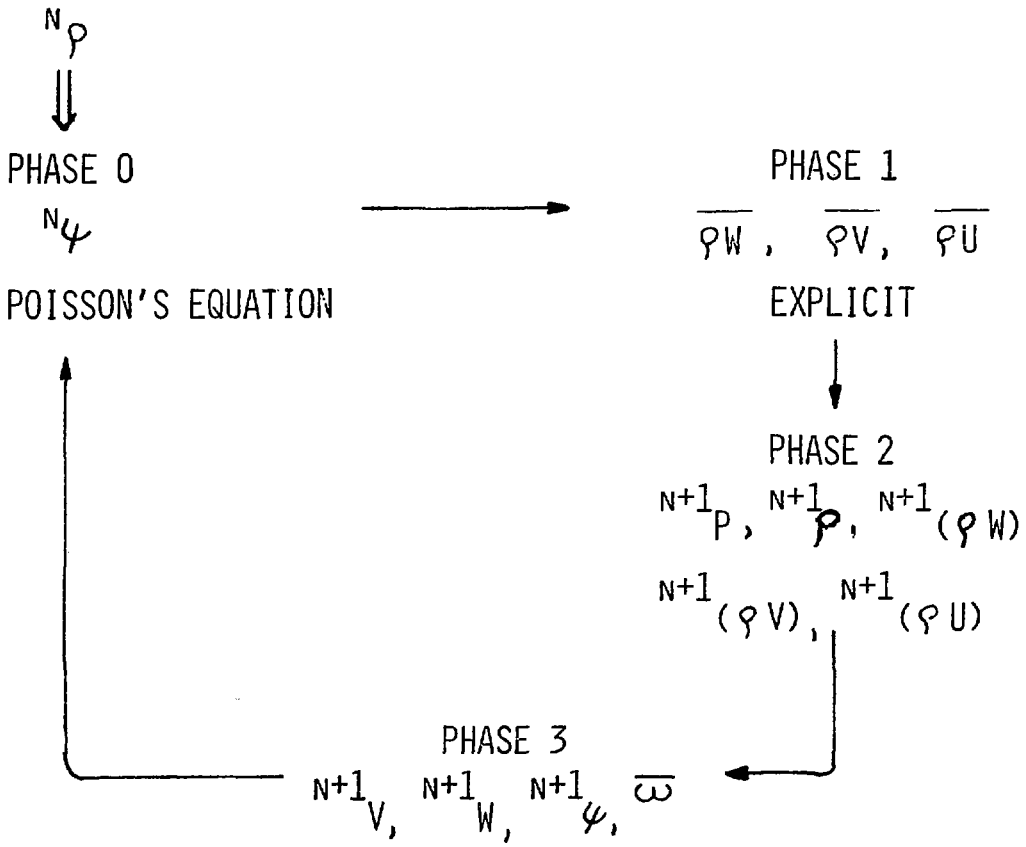

FIGURE 3

D. DIFFERENCE TECHNIQUE

1. Donor-Cell Fluxes

Donor-cell fluxing of the mass and momentum convective fluxes can help ensure numerical stability for problems in which violent discontinuities are present either initially or at various stages of the calculation.[56] In the present methodology the convection terms are written so that one may weight the donor-cell averages by varying the parameter α. Equation (III-1) defines the basic donor-cell nomenclature.

$$< u Q >_{i+\frac{1}{2}jk} \equiv u_{i+\frac{1}{2}jk} \left[(1/2 + \xi)\, Q_{ijk} + (1/2 - \xi)\, Q_{i+1jk} \right] \qquad \text{(III-1)}$$

where

$$\xi = \alpha \text{ sign } \left(u_{i+\frac{1}{2}jk} \right)$$

and

$$0 \leqslant \alpha \leqslant 1/2 \quad .$$

In the above expression Q is the physical quantity being convected by the velocity u. In the rotating coordinate system where the convection is controlled by the quantity v-rω, it is this net quantity that determines the sign of ξ and that appears as the coefficient in Eq. (III-1). It is the use of this net quantity in the donor-cell terms that minimizes the artificial diffusion. For full donor-cell differencing one would choose $\alpha = 1/2$.

Donor-cell fluxing provides a means by which a weighted average that depends on the direction and magnitude of the fluid flow can be performed

on the physical variables. If a physical quantity to be fluxed appears in a product with a coordinate, the coordinate should be taken out of the brackets along with the convecting velocity. That is, there is no logical reason for performing a flow-weighted average on a variable that is not moving with the fluid. If, however, the physical quantity being convected contains a coordinate within its definition (such as angular momentum), the quantity should not be decomposed, and the donor-cell average is applied to the product. These rules are exhibited for some selected donor-cell terms, which are specifically expanded in Appendix B.

From an examination of Eq. (III-1), one sees that the donor-cell flux is not space-centered unless ξ=0. As a result low order truncation errors in δr, $\delta\theta$, and δz are introduced.[57, 58] These terms provide a positive diffusion that tends to automatically stabilize the numerical calculations. The advantage of the donor-cell technique can also be its disadvantage because the magnitude of the positive diffusion can in certain circumstances be significant enough to obscure real diffusive effects.

2. Averaging Schemes

In numerical calculations one must often perform simple averages to obtain values of the physical variables at the mesh locations demanded by the difference equations. This requirement is independent of the actual differencing scheme (i.e., donor-cell, space-centered, ZIP,[59] etc.) used. For example, if two quantities occur in a product such that neither quantity appears as it is naturally centered, one can either average the products or take the product of the respective averages. Except where specifically indicated, the latter technique is employed throughout this methodology.

E. PHASE 0: GRAVITATIONAL POTENTIAL

1. Tilde Notation

Given ${}^{n}\rho_{ijk}$, ${}^{n}\psi_{ijk}$, and the new values for ψ on the outer and upper boundaries and in the central core region, one relaxes Poisson's equation iteratively. To simplify the representations, one can develop a tilde notation to indicate iterated values. One can write

$$\tilde{Q}_{ijk} = \tilde{Q}_{ijk} + \delta Q_{ijk} \tag{III-2}$$

with the convention that this statement is not an equation but rather an expression for the way in which the new value on the left is calculated from the old value on the right.

2. Relaxation of Poisson's Equation

One can represent the finite difference version of Eq. (II-15) by means of the statement $\tilde{L}_{ijk} = 0$, in which

$$\begin{aligned}\tilde{L}_{ijk} \equiv \frac{1}{r_i\,\delta r^2}\left[r_{i+\frac{1}{2}}\left(\tilde{\psi}_{i+1jk} - \tilde{\psi}_{ijk}\right) - r_{i-\frac{1}{2}}\left(\tilde{\psi}_{ijk} - \tilde{\psi}_{i-1jk}\right)\right] \\ + \frac{1}{r_i^{\,2}\,\delta\theta^2}\left(\tilde{\psi}_{ij+1k} + \tilde{\psi}_{ij-1k} - 2\tilde{\psi}_{ijk}\right) \\ + \frac{1}{\delta z^2}\left(\tilde{\psi}_{ijk+1} + \tilde{\psi}_{ijk-1} - 2\tilde{\psi}_{ijk}\right) - 4\pi G\,{}^{n}\rho_{ijk} \quad .\end{aligned} \tag{III-3}$$

Given a first approximation to a root of the equation $\hat{L}_{ijk} = 0$, one can obtain an improved value by employing Newton's Iterative Method.[60]

$$\delta\tilde{\psi}_{ijk} = -\frac{\tilde{L}_{ijk}}{\dfrac{\partial\tilde{L}_{ijk}}{\partial\tilde{\psi}_{ijk}}} \tag{III-4}$$

where

$$\frac{\partial \tilde{L}_{ijk}}{\partial \tilde{\psi}_{ijk}} = -2\left(\frac{1}{\delta r^2} + \frac{1}{r_i^2\,\delta\theta^2} + \frac{1}{\delta z^2}\right) \quad .$$

The updated potential follows

$$\tilde{\psi}_{ijk} = \tilde{\psi}_{ijk} + \delta\tilde{\psi}_{ijk} \quad . \tag{III-5}$$

With the improved scalar potential, one now recalculates $\tilde{L}_{ijk}$ and tests for convergence according to the following prescription.

$$|\tilde{L}_{ijk}| \leq \Delta\left(4\pi\epsilon\,{}^{n}\rho_{max} + \frac{|\tilde{\psi}_{ijk}|}{\delta r^2 + r_i^2\,\delta\theta^2 + \delta z^2}\right) \tag{III-6}$$

where Δ is a constant that controls the tightness of the convergence and hence the accuracy of the root.

F. PHASE 1: THE BAR QUANTITIES

1. Axial Equation

In this section and the subsequent one, the equations developed in the previous chapter are presented in difference form. In Phase 1 the "bar" quantities are calculated. Beginning with the axial momentum equation one first calculates the z-component of the viscous stress tensor, Eq. (II-13).

$${}^{n}\left(V_z\right)_{ijk+\frac{1}{2}} = \nu\left\{\frac{1}{r_i\,\delta r^2}\left[{}^{n}\left(\rho r\right)_{i+\frac{1}{2}jk+\frac{1}{2}}\left({}^{n}W_{i+1jk+\frac{1}{2}} - {}^{n}W_{ijk+\frac{1}{2}}\right)\right.\right.$$

$$\left.\left. - {}^{n}\left(\rho r\right)_{i-\frac{1}{2}jk+\frac{1}{2}}\left({}^{n}W_{ijk+\frac{1}{2}} - {}^{n}W_{i-1jk+\frac{1}{2}}\right)\right]\right.$$

$$+ \frac{1}{r_i^2 \delta\theta^2} \left[{}^{n}\rho_{ij+\frac{1}{2}k+\frac{1}{2}} \left({}^{n}w_{ij+1k+\frac{1}{2}} - {}^{n}w_{ijk+\frac{1}{2}} \right) \right.$$

$$\left. - {}^{n}\rho_{ij-\frac{1}{2}k+\frac{1}{2}} \left({}^{n}w_{ijk+\frac{1}{2}} - {}^{n}w_{ij-1k+\frac{1}{2}} \right) \right]$$

$$+ \frac{1}{\delta z^2} \left[{}^{n}\rho_{ijk+1} \left({}^{n}w_{ijk+3/2} - {}^{n}w_{ijk+\frac{1}{2}} \right) \right.$$

$$\left. \left. - {}^{n}\rho_{ijk} \left({}^{n}w_{ijk+\frac{1}{2}} - {}^{n}w_{ijk-\frac{1}{2}} \right) \right] \right\} \quad . \tag{III-7}$$

The initial guess for the new axial momentum of each cell follows directly from the V_z's and from the ψ's. Deleting the pressure term in Eq. (II-22), one defines

$$(\overline{\rho v'})_{ijk+\frac{1}{2}} \equiv {}^{n}(\rho w)_{ijk+\frac{1}{2}} + \delta t \left\{ \frac{1}{r_i \delta r} \left({}^{n}\langle \rho uwr \rangle_{i-\frac{1}{2}jk+\frac{1}{2}} \right.\right.$$

$$\left. - {}^{n}\langle \rho uwr \rangle_{i+\frac{1}{2}jk+\frac{1}{2}} \right) + \frac{1}{r_i \delta\theta} \left({}^{n}\langle \rho w(v - r\omega) \rangle_{ij-\frac{1}{2}k+\frac{1}{2}} \right.$$

$$\left. - {}^{n}\langle \rho w(v - r\omega) \rangle_{ij+\frac{1}{2}k+\frac{1}{2}} \right) + \frac{1}{\delta z} \left({}^{n}\langle \rho w^2 \rangle_{ijk} - \langle \rho w^2 \rangle_{ijk+1} \right)$$

$$\left. + \frac{{}^{n}\rho_{ijk+\frac{1}{2}}}{\delta z} \left({}^{n}\psi_{ijk} - {}^{n}\psi_{ijk+1} \right) + {}^{n}(V_z)_{ijk+\frac{1}{2}} \right\} \tag{III-8}$$

2. Azimuthal Equation

The θ-component of the viscous stress from Eq. (II-12) is

$${}^{n}(V_\theta)_{ij+\frac{1}{2}k} = \nu \left\{ \frac{1}{r_i^2 \delta r} \left[\frac{{}^{n}(\rho r^2)_{i+\frac{1}{2}j+\frac{1}{2}k}}{\delta r} \left({}^{n}v_{i+1j+\frac{1}{2}k} - {}^{n}v_{ij+\frac{1}{2}k} \right) \right. \right.$$

$$- {}^{n}(\rho r)_{i+\frac{1}{2}j+\frac{1}{2}k} \, {}^{n}v_{i+\frac{1}{2}j+\frac{1}{2}k} - \frac{{}^{n}(\rho r^2)_{i-\frac{1}{2}j+\frac{1}{2}k}}{\delta r}$$

$$\left({}^{n}v_{ij+\frac{1}{2}k} - {}^{n}v_{i-1j+\frac{1}{2}k}\right) + {}^{n}(\rho r)_{i-\frac{1}{2}j+\frac{1}{2}k} \, {}^{n}v_{i-\frac{1}{2}j+\frac{1}{2}k}\Bigg]$$

$$+ \frac{1}{r_i^2 \, \delta\theta^2}\left[{}^{n}\rho_{ij+1k}\left({}^{n}v_{ij+3/2k} - {}^{n}v_{ij+\frac{1}{2}k}\right) - {}^{n}\rho_{ijk}\left({}^{n}v_{ij+\frac{1}{2}k}\right.\right.$$

$$\left.\left. - {}^{n}v_{ij-\frac{1}{2}k}\right)\right] + \frac{2}{r_i^2 \, \delta\theta}\left[{}^{n}(\rho u)_{ij+1k} - {}^{n}(\rho u)_{ijk}\right]$$

$$+ \frac{1}{\delta z^2}\left[{}^{n}\rho_{ij+\frac{1}{2}k+\frac{1}{2}}\left({}^{n}v_{ij+\frac{1}{2}k+1} - {}^{n}v_{ij+\frac{1}{2}k}\right)\right.$$

$$\left.\left. - {}^{n}\rho_{ij+\frac{1}{2}k-\frac{1}{2}}\left({}^{n}v_{ij+\frac{1}{2}k} - {}^{n}v_{ij+\frac{1}{2}k-1}\right)\right]\right\} \qquad \text{(III-9)}$$

Omitting the pressure terms from Eq. (II-21) and using Eq. (III-9), one defines the explicit part of the azimuthal momentum equation in difference form.

$${}^{n}(\overline{\rho v})_{ij+\frac{1}{2}k} \equiv {}^{n}(\rho v)_{ij+\frac{1}{2}k} + \delta t\left\{\frac{1}{r_i^2 \, \delta r}\left({}^{n}<\rho uvr^2>_{i-\frac{1}{2}j+\frac{1}{2}k}\right.\right.$$

$$\left. - {}^{n}<\rho uvr^2>_{i+\frac{1}{2}j+\frac{1}{2}k}\right) + \frac{1}{r_i \, \delta\theta}\left({}^{n}<\rho v(v - r\omega)>_{ijk}\right.$$

$$\left. - {}^{n}<\rho v(v - r\omega)>_{ij+1k}\right) + \frac{1}{\delta z}\left({}^{n}<\rho vw>_{ij+\frac{1}{2}k-\frac{1}{2}}\right.$$

$$\left. - {}^{n}<\rho vw>_{ij+\frac{1}{2}k+\frac{1}{2}}\right) + \frac{\rho_{ij+\frac{1}{2}k}}{r_i \, \delta\theta}\left({}^{n}\psi_{ijk} - {}^{n}\psi_{ij+1k}\right)$$

$$+ {}^{n}(V_\theta)_{ij+\frac{1}{2}k} \Bigg\} \quad . \tag{III-10}$$

3. Radial Equation

For the r-component of the viscous stress one has from Eq. (II-11),

$$\begin{aligned}
{}^{n}(V_r)_{i+\frac{1}{2}jk} = \nu \Bigg\{ & \frac{1}{\delta r^2}\left[\frac{{}^{n}\rho_{i+1jk}}{r_{i+1}}\left(r_{i+3/2}\,{}^{n}u_{i+3/2jk} - r_{i+\frac{1}{2}}\,{}^{n}u_{i+\frac{1}{2}jk}\right)\right. \\
& - \frac{{}^{n}\rho_{ijk}}{r_i}\left(r_{i+\frac{1}{2}}\,{}^{n}u_{i+\frac{1}{2}jk} - r_{i-\frac{1}{2}}\,{}^{n}u_{i-\frac{1}{2}jk}\right) + \frac{1}{r^2_{i+\frac{1}{2}}\,\delta\theta^2} \\
& \cdot\left[{}^{n}\rho_{i+\frac{1}{2}j+\frac{1}{2}k}\left({}^{n}u_{i+\frac{1}{2}j+1k} - {}^{n}u_{i+\frac{1}{2}jk}\right) - {}^{n}\rho_{i+\frac{1}{2}j-\frac{1}{2}k}\left({}^{n}u_{i+\frac{1}{2}jk}\right.\right. \\
& \left.\left. - {}^{n}u_{i+\frac{1}{2}j-1k}\right)\right] - 2\,\frac{{}^{n}\rho_{i+\frac{1}{2}jk}}{r^2_{i+\frac{1}{2}}\,\delta\theta}\left({}^{n}v_{i+\frac{1}{2}j+\frac{1}{2}k} - {}^{n}v_{i+\frac{1}{2}j-\frac{1}{2}k}\right) \\
& + \frac{1}{\delta z^2}\left[{}^{n}\rho_{i+\frac{1}{2}jk+\frac{1}{2}}\left({}^{n}u_{i+\frac{1}{2}jk+1} - {}^{n}u_{i+\frac{1}{2}jk}\right) - {}^{n}\rho_{i+\frac{1}{2}jk-\frac{1}{2}}\right. \\
& \left.\left.\cdot\left({}^{n}u_{i+\frac{1}{2}jk} - {}^{n}u_{i+\frac{1}{2}jk-1}\right)\right]\right\} \quad .
\end{aligned} \tag{III-11}$$

From Eqs. (II-20) and (III-11) one has for the explicit portion of the radial momentum equation again with the pressure terms absent

$$\begin{aligned}
(\overline{\rho u})_{i+\frac{1}{2}jk} \equiv {}^{n}(\rho u)_{i+\frac{1}{2}jk} + \delta t \Bigg\{ & \frac{1}{r_{i+\frac{1}{2}}\,\delta r}\left({}^{n}\langle \rho u^2 r\rangle_{ijk}\right. \\
& \left. - {}^{n}\langle \rho u^2 r\rangle_{i+1jk}\right) + \frac{1}{r_{i+\frac{1}{2}}\,\delta\theta}\left({}^{n}\langle \rho u(v - r\omega)\rangle_{i+\frac{1}{2}j-\frac{1}{2}k}\right.
\end{aligned}$$

$$- {}^{n}\langle \rho u(v - r\omega)\rangle_{i+\frac{1}{2}j+\frac{1}{2}k}\Big) + \frac{1}{\delta z}\left({}^{n}\langle \rho uw\rangle_{i+\frac{1}{2}jk-\frac{1}{2}}\right.$$

$$\left. - {}^{n}\langle \rho uw\rangle_{i+\frac{1}{2}jk+\frac{1}{2}}\right) + \frac{\rho_{i+\frac{1}{2}jk}}{\delta r}\left({}^{n}\psi_{ijk} - {}^{n}\psi_{i+1jk}\right)$$

$$+ \frac{{}^{n}\rho_{i+\frac{1}{2}jk}\ {}^{n}v^{2}_{i+\frac{1}{2}jk}}{r_{i+\frac{1}{2}}} + {}^{n}(V_r)_{i+\frac{1}{2}jk}\Bigg\} \quad . \qquad \text{(III-12)}$$

4. The Difference Equations

From all of the segments introduced and defined in this section we are now in a position to exhibit the full finite difference version of the equations used for the calculations.

$$\frac{{}^{n+1}\rho_{ijk} - {}^{n}\rho_{ijk}}{\delta t} + \frac{1}{r_i\,\delta r}\left({}^{n+1}\langle \rho ur\rangle_{i+\frac{1}{2}jk} - {}^{n+1}\langle \rho ur\rangle_{i-\frac{1}{2}jk}\right)$$

$$+ \frac{1}{r_i\,\delta\theta}\left({}^{n+1}\langle \rho(v-r\omega)\rangle_{ij+\frac{1}{2}k} - {}^{n+1}\langle \rho(v-r\omega)\rangle_{ij-\frac{1}{2}k}\right)$$

$$+ \frac{1}{\delta z}\left({}^{n+1}\langle \rho w\rangle_{ijk+\frac{1}{2}} - {}^{n+1}\langle \rho w\rangle_{ijk-\frac{1}{2}}\right) = 0$$

$$\text{(III-13)}$$

$${}^{n+1}(\rho w)_{ijk+\frac{1}{2}} = (\overline{\rho w})_{ijk+\frac{1}{2}} + \frac{\delta t}{\delta z}\left({}^{n+1}p_{ijk} - {}^{n+1}p_{ijk+1}\right) \qquad \text{(III-14)}$$

$${}^{n+1}(\rho v)_{ij+\frac{1}{2}k} = (\overline{\rho v})_{ij+\frac{1}{2}k} + \frac{\delta t}{r_i\,\delta\theta}\left({}^{n+1}p_{ijk} - {}^{n+1}p_{ij+1k}\right) \qquad \text{(III-15)}$$

$${}^{n+1}(\rho u)_{i+\frac{1}{2}jk} = (\overline{\rho u})_{i+\frac{1}{2}jk} + \frac{\delta t}{\delta r}\left({}^{n+1}p_{ijk} - {}^{n+1}p_{i+1jk}\right) \qquad \text{(III-16)}$$

G. PHASE 2: ITERATIVE RELAXATION OF THE MASS AND MOMENTUM EQUATIONS

1. Initialization

During this phase of a computational cycle, the continuity equation and the momentum equations are solved simultaneously using an iterative relaxation scheme. At the beginning of phase 2 the components of axial, azimuthal and radial momentum are initialized using the newly obtained "bar" quantities and the pressure field at time n. Using the tilde notation developed in the gravitational potential section,

$$(\widetilde{\rho w})_{ijk+\frac{1}{2}} = (\overline{\rho w})_{ijk+\frac{1}{2}} + \frac{\delta t}{\delta z}\left({}^{n}p_{ijk} - {}^{n}p_{ijk+1}\right) \tag{III-17}$$

$$(\widetilde{\rho v})_{ij+\frac{1}{2}k} = (\overline{\rho v})_{ij+\frac{1}{2}k} + \frac{\delta t}{r_i\,\delta\theta}\left({}^{n}p_{ijk} - {}^{n}p_{ij+1k}\right) \tag{III-18}$$

$$(\widetilde{\rho u})_{i+\frac{1}{2}jk} = (\overline{\rho u})_{i+\frac{1}{2}jk} + \frac{\delta t}{\delta r}\left({}^{n}p_{ijk} - {}^{n}p_{i+1jk}\right) \quad . \tag{III-19}$$

2. Calculating New Pressures and Densities

One now commences the implicit portion of the phase by defining a function $\widetilde{D}_{ijk}$ that goes to zero when the equation of continuity is satisfied. From Eq. (III-13)

$$\widetilde{D}_{ijk} \equiv \frac{\widetilde{\rho}_{ijk} - {}^{n}\rho_{ijk}}{\delta t} + \frac{1}{r_i\,\delta r}\left(<\widetilde{\rho u}\, r>_{i+\frac{1}{2}jk} - <\widetilde{\rho u}\, r>_{i-\frac{1}{2}jk}\right)$$

$$+ \frac{1}{r_i\,\delta\theta}\left(<\widetilde{\rho}(\widetilde{v} - r\omega)>_{ij+\frac{1}{2}k} - <\widetilde{\rho}(\widetilde{v} - r\omega)>_{ij-\frac{1}{2}k}\right)$$

$$+ \frac{1}{\delta z}\left(<\widetilde{\rho w}>_{ijk+\frac{1}{2}} - <\widetilde{\rho w}>_{ijk-\frac{1}{2}}\right) . \tag{III-20}$$

The procedure used to obtain the roots of $\tilde{D}$ is again that of Newton, although the process is somewhat more involved here than in the solution of Poisson's equation described earlier. One must form the partial derivative of $\tilde{D}_{ijk}$ with respect to $\tilde{p}_{ijk}$. To avoid a fairly complicated derivative, one can define a function $\tilde{\mathcal{D}}_{ijk}$ that is identical to the function $\tilde{D}_{ijk}$ except for the replacement of the donor-cell fluxes with simple cell-centered fluxes.

$$\tilde{\mathcal{D}}_{ijk} \equiv \frac{\tilde{\rho}_{ijk} - {}^{n}\rho_{ijk}}{\delta t} + \frac{1}{r_i \delta r}\left[(\tilde{\rho u}\, r)_{i+\frac{1}{2}jk} - (\tilde{\rho u}\, r)_{i-\frac{1}{2}jk}\right]$$

$$+ \frac{1}{r_i \delta\theta}\left[\tilde{\rho}(\tilde{v} - r\omega)_{\,ij+\frac{1}{2}k} - \tilde{\rho}(\tilde{v} - r\omega)_{\,ij-\frac{1}{2}k}\right]$$

$$+ \frac{1}{\delta z}\left[(\tilde{\rho w})_{ijk+\frac{1}{2}} - (\tilde{\rho w})_{ijk-\frac{1}{2}}\right] \qquad \text{(III-21)}$$

Forming the partial derivative of $\tilde{\mathcal{D}}_{ijk}$

$$\frac{\partial\tilde{\mathcal{D}}_{ijk}}{\partial\tilde{p}_{ijk}} = \frac{1}{\delta t}\frac{\partial\tilde{\rho}_{ijk}}{\partial\tilde{p}_{ijk}} + \frac{1}{r_i \delta r}\left[r_{i+\frac{1}{2}}\frac{\partial(\tilde{\rho u})_{i+\frac{1}{2}jk}}{\partial\tilde{p}_{ijk}} - r_{i-\frac{1}{2}}\frac{\partial(\tilde{\rho u})_{i-\frac{1}{2}jk}}{\partial\tilde{p}_{ijk}}\right]$$

$$+ \frac{1}{r_i \delta\theta}\left[\frac{\partial(\tilde{\rho v})_{ij+\frac{1}{2}k}}{\partial\tilde{p}_{ijk}} - \frac{\partial(\tilde{\rho v})_{ij-\frac{1}{2}k}}{\partial\tilde{p}_{ijk}}\right]$$

$$+ \frac{1}{\delta z}\left[\frac{\partial(\tilde{\rho w})_{ijk+\frac{1}{2}}}{\partial\tilde{p}_{ijk}} - \frac{\partial(\tilde{\rho w})_{ijk-\frac{1}{2}}}{\partial\tilde{p}_{ijk}}\right] \qquad \text{(III-22)}$$

in which the derivative of the ω terms has been neglected. From the equation of state, Eq. (II-14)

$$\frac{\partial \tilde{p}_{ijk}}{\partial \tilde{p}_{ijk}} = 1 = A \frac{\partial (\tilde{\rho}_{ijk})^{\gamma}}{\partial \tilde{p}_{ijk}} = \gamma A (\tilde{\rho}_{ijk})^{\gamma-1} \frac{\partial \tilde{\rho}_{ijk}}{\partial \tilde{p}_{ijk}}$$

or

$$\frac{\partial \tilde{\rho}_{ijk}}{\partial \tilde{p}_{ijk}} = \frac{1}{\gamma A (\tilde{\rho}_{ijk})^{\gamma-1}} \tag{III-23}$$

From Eqs. (III-14), (III-15), and (III-16) with the pressures at time $n+1$ replaced by the "tilde" pressures Eq. (III-22) becomes

$$\frac{\partial \tilde{\mathcal{D}}_{ijk}}{\partial \tilde{p}_{ijk}} = \frac{1}{\delta t \gamma A (\tilde{\rho}_{ijk})^{\gamma-1}} + \frac{1}{r_i \delta r}\left[r_{i+\frac{1}{2}} \frac{\delta t}{\delta r} + r_{i-\frac{1}{2}} \frac{\delta t}{\delta r}\right]$$

$$+ \frac{1}{r_i \delta\theta}\left[\frac{\delta t}{r_i \delta\theta} + \frac{\delta t}{r_i \delta\theta}\right] + \frac{1}{\delta z}\left[\frac{\delta t}{\delta z} + \frac{\delta t}{\delta z}\right]$$

or

$$\frac{\partial \tilde{\mathcal{D}}_{ijk}}{\partial \tilde{p}_{ijk}} = \frac{1}{\delta t A \gamma (\tilde{\rho}_{ijk})^{\gamma-1}} + \frac{2\delta t}{\delta r^2} + \frac{2\delta t}{r_i^2 \delta\theta^2} + \frac{2\delta t}{\delta z^2} \tag{III-24}$$

The new $\delta \tilde{p}_{ijk}$'s follow from Eqs. (III-20) and (III-24)

$$\delta \tilde{p}_{ijk} = - \frac{\tilde{D}_{ijk}}{\frac{\partial \tilde{\mathcal{D}}_{ijk}}{\partial \tilde{p}_{ijk}}} \quad . \tag{III-25}$$

Once the solution has converged it will not matter that the equations have been relaxed substituting the approximate expression, Eq. (III-24), for the exact $\frac{\partial \tilde{D}_{ijk}}{\partial \tilde{p}_{ijk}}$. In addition to being less complicated, Eq. (III-24) tends to relax the system in fewer iterations than the corresponding expression for $\frac{\partial \tilde{D}_{ijk}}{\partial \tilde{p}_{ijk}}$. From Eq. (III-25) one sees that this latter conclusion is reasonable because, as shown in a subsequent section, the approximate derivative is always smaller than the exact one. If, however, the equations do not converge, the correct derivative or a closer approximation reflecting more of the nature of the fluid flow can serve as a remedy. For certain situations it is necessary to use this more nearly correct expression. A detailed discussion of $\frac{\partial \tilde{D}_{ijk}}{\partial \tilde{p}_{ijk}}$ is reserved for the section of this chapter entitled Special Methodological Developments.

From Eq. (III-25) the new p_{ijk}'s follow directly.

$$\tilde{p}_{ijk} = \tilde{p}_{ijk} + \delta\tilde{p}_{ijk} \qquad \text{(III-26)}$$

With these new pressures and the equation of state, the new densities are

$$\tilde{\rho}_{ijk} = \left(\frac{\tilde{p}_{ijk}}{A}\right)^{1/\gamma} \qquad \text{(III-27)}$$

3. Momentum Equations

The "bar" quantities and the new pressures allow one to solve for the momentum components.

$$(\tilde{\rho w})_{ijk+\frac{1}{2}} = (\overline{\rho w})_{ijk+\frac{1}{2}} + \frac{\delta t}{\delta z}\left(\tilde{p}_{ijk} - \tilde{p}_{ijk+1}\right) \qquad \text{(III-28)}$$

$$(\widetilde{\rho v})_{ij+\frac{1}{2}k} = (\overline{\rho v})_{ij+\frac{1}{2}k} + \frac{\delta t}{r_i \delta\theta}\left(\widetilde{p}_{ijk} - \widetilde{p}_{ij+1k}\right) \tag{III-29}$$

$$(\widetilde{\rho u})_{i+\frac{1}{2}jk} = (\overline{\rho u})_{i+\frac{1}{2}jk} + \frac{\delta t}{\delta r}\left(\widetilde{p}_{ijk} - \widetilde{p}_{i+1jk}\right) \tag{III-30}$$

One now tests for convergence according to the simple prescription

$$\widetilde{D}_{ijk} \leq \frac{\varepsilon\, \rho_{max}}{\delta t} \tag{III-31}$$

The quantity ρ_{max} is a maximum density obtained at each iteration level, and ε is a factor controlling the tightness of the convergence. If any $\widetilde{D}_{ijk}$ fails to satisfy the criterion defined by Eq. (III-31), the calculation returns to Eq. (III-20) and the whole process begins again. When the convergence test has been satisfied the tilde quantities become the n+1 quantities.

H. PHASE 3: VELOCITY COMPONENTS AND THE NEW FRAME

One can now separate the velocity components from their respective momenta. The following equations are used.

$$^{n+1}u_{i+\frac{1}{2}jk} = \frac{^{n+1}(\rho u)_{i+\frac{1}{2}jk}}{^{n+1}\rho_{i+\frac{1}{2}jk}} \tag{III-32}$$

$$^{n+1}v_{ij+\frac{1}{2}k} = \frac{^{n+1}(\rho v)_{ij+\frac{1}{2}k}}{^{n+1}\rho_{ij+\frac{1}{2}k}} \tag{III-33}$$

$$^{n+1}w_{ijk+\frac{1}{2}} = \frac{^{n+1}(\rho w)_{ijk+\frac{1}{2}}}{^{n+1}\rho_{ijk+\frac{1}{2}}} \tag{III-34}$$

The angular velocity of the rotating frame to which the variables are referred is selected by requiring the net angular momentum relative to it be zero.

$$\sum_{ijk} r_i \, \delta r \, \delta\theta \, \delta z \; {}^{n+1}(\rho r)_{ij+\frac{1}{2}k} \left({}^{n+1}v_{ij+\frac{1}{2}k} - r_i \, \omega \right) = 0 \qquad \text{(III-35)}$$

Solving for ω

$$\omega = \frac{\sum_{ijk} r_i^{\,2} \; {}^{n+1}(\rho v)_{ij+\frac{1}{2}k}}{\sum_{ijk} r_i^{\,3} \; {}^{n+1}\rho_{ij+\frac{1}{2}k}} \qquad \text{(III-36)}$$

I. REPRESENTATION OF THE VARIABLES

In order to follow the general evolution of the physical system and to isolate significant characteristics, one must have a way to represent the field variables in a useful and convenient fashion. The difficulties attendent to the successful analysis of three-dimensional results are non-trivial. The approach taken in this work utilizes two types of printout and three types of graphical representation to exhibit system properties.

A short print summarizing certain aspects of the problem at each cycle is used to provide a frequent monitoring of the evolution. Quantities presented in the short print include the cycle number, the problem time, the current time step, the number of iterations in the gravitational potential and in the phase 2 calculation respectively, the central pressures, densities, and velocities, the angular velocity of the rotating frame and its variation with time, the total gravitational, kinetic, rotational and internal energies, the total angular momentum relative to

both fixed and rotating frames, and the total mass. At selected edit times a long print yields the value of all dependent variables at every mesh point.

The graphical display of such a complicated system is also desirable in analyzing the results. At selected edit times contour plots of density, pressure, gravitational potential, and angular velocity relative to the fixed frame are plotted in mutually perpendicular planes. The r-θ plots are in the $z = 0$ plane. The r-z contours are along a ray through the most massive regions of the fluid. Velocity vector plots are also provided in these planes. One of the most useful forms of graphical representation is the computer movie. A movie allows the researcher to observe the total system in continuous stages of evolution, making it less easy to overlook significant developments and perturbations. Movies are therefore made to follow the progress of selected problems.

J. SPECIAL METHODOLOGICAL DEVELOPMENTS

1. Symmetry

In order to gain confidence in the physical significance of the results produced by the methodology for general three-dimensional problems for which it is either difficult or impossible to make direct ties to analytic theory or to observation, one can make a series of calculations that have simple symmetries and can check the conservation of symmetries as the systems evolve. If, for example, one initiates a collapse problem with an initial spherical configuration and no rotation, the system should retain this symmetry throughout its evolution and the azimuthal velocities should remain zero. Several such studies have been made, and the results indicate that the convergence of the gravitational potential must be rather tight (about 10 significant digits are required) if the

symmetric characteristics of the problem are to be maintained at late time. If the convergence criterion is relaxed, a substantial azimuthal velocity field develops with velocities comparable in magnitude to radial and axial collapse velocities. By requiring the same degree of accuracy during the evolution of asymmetric self-gravitating systems, one ensures that the observed dynamical phenomena are more likely to be real in the sense that they result from natural physical processes rather than from numerical inaccuracies.

2. Numerical Stability

a. Classical considerations

The next facet of special methodology concerns a difficulty with numerical stability. To describe this difficulty one must first consider the classical aspects of numerical instability as follows. Three-dimensional problems are very time consuming and expensive. One reason that these are slow arises from the fact that one is trying to resolve a volume of space in some detail with a discrete calculational mesh. Many cells are utilized even for coarsely resolved problems. The three-dimensional methodologies are more complicated because one is dealing with more coupled nonlinear partial differential equations, and the added complexities result in slower problem evolution. To speed the calculation one must force the system to evolve using the largest possible time steps subject to numerical stability requirements. The time step is controlled by the condition

$$\frac{v_{max}\,\delta t}{\delta x} < 1 \qquad \text{(III-37)}$$

v_{max} is the maximum velocity component in the system at time n and δx is the corresponding coordinate zone size. For the azimuthal velocity, one uses $(v - r\omega)$ and $r\delta\theta$ for v_{max} and δx, respectively. The above expression is a statement that the fluid cannot traverse more than one zone in a given time step. To be cautious during the rather violent dynamical stages of evolution of the fluid systems studied in this work, the left-hand side of Eq. (III-37) is restricted to being 1/5 or less.

There are other constraints that must be considered in this discussion of numerical instability. These constraints limit the magnitude of the artificial viscosity. From stability analysis,[61] one must satisfy the following condition

$$\nu\,\delta t < \frac{1}{2\left(\frac{1}{\delta r^2} + \frac{1}{r_i^2\,\delta\theta} + \frac{1}{\delta z^2}\right)} \qquad \text{(III-38)}$$

whereas the lower limit of the viscosity is constrained by the requirement

$$\nu > \frac{1}{2} v_{max}^2\,\delta t + \frac{1}{2}\frac{v_{max}\,\delta x}{n} \qquad \text{(III-39)}$$

where n is the number of cells necessary to define the width of the gradients. Typically, one selects an n of 2. The above three conditions are not independent; and if δx is selected appropriately, Eq. (III-39) is automatically satisfied when Eq. (III-37) is used to determine the time step and when Eq. (III-38) is used to obtain the kinematic viscosity. Note that Eq. (III-38) illustrates the motivation for a central core in the calculation, which excludes some zones which would otherwise be very narrow in the vicinity of the axis. The corresponding small value of $r_i\,\delta\theta$ would introduce severe restrictions on the time step. Since

calculations in three space dimensions are very time consuming with even the fastest modern computers, the added time step restriction should be avoided.

b. Local viscosity instabilities

Despite adherence to the restrictions described in the preceding paragraphs, difficulties can arise from a somewhat different type of local viscosity instability. Density discontinuities in adjacent cells can be many orders of magnitude in the regions of the mesh far removed from a center of gravitational attraction. If in four adjacent cells one cell has a relatively high density compared to that of the other three, the average density required at the common nodal point by the viscous stress components would be that of the high density cell if a straight linear average of all four were used. The resulting momentum flux would then be too great for the low density zones. Experience with this four-cell-average approach shows indeed that the velocity at such interfaces can grow catastrophically in magnitude, changing sign every time step.

A fairly simple solution to this difficulty can be implemented. One forms a linear two-cell average of the densities on either side of the viscous flux direction and then selects the lower value for use in the viscous stress components. This procedure is conservative of momentum because the value of density assigned to a node is the same when viewed from either side of the flux. The fact that this technique is applied throughout all regions of the mesh is of no consequence to this research because the viscous stress components and the kinematic viscosity are not used as physical properties of the fluid, but are instead numerical artifacts employed for stability.

3. Partial Derivative of $\tilde{D}_{ijk}$

For certain dynamical systems the equations may not converge using the $\frac{\partial \tilde{p}_{ijk}}{\partial \tilde{p}_{ijk}}$ approximation given in Eq. (III-24). In these instances the convergence can be regained by using the correct expression, formed by the partial derivative of Eq. (III-20) rather than of Eq. (III-21). From Eq. (III-20) one has

$$\frac{\partial \tilde{D}_{ijk}}{\partial \tilde{p}_{ijk}} = \frac{1}{\delta t}\frac{\partial \tilde{\rho}_{ijk}}{\partial \tilde{p}_{ijk}} + \frac{1}{r_i\,\delta r}\frac{\partial}{\partial \tilde{p}_{ijk}}\left(<\tilde{\rho u}\, r>_{i+\frac{1}{2}jk} - <\tilde{\rho u}\, r>_{i-\frac{1}{2}jk}\right)$$

$$+ \frac{1}{r_i\,\delta\theta}\frac{\partial}{\partial \tilde{p}_{ijk}}\left(<\tilde{\rho}(\tilde{v} - r\omega)>_{ij+\frac{1}{2}k} - <\tilde{\rho}(\tilde{v} - r\omega)>_{ij-\frac{1}{2}k}\right)$$

$$+ \frac{1}{\delta z}\frac{\partial}{\partial \tilde{p}_{ijk}}\left(<\tilde{\rho w}>_{ijk+\frac{1}{2}} - <\tilde{\rho w}>_{ijk-\frac{1}{2}}\right) \qquad \text{(III-40)}$$

The first term in Eq. (III-40) is simply Eq. (III-23). To obtain the partial derivatives of the donor-cell terms, these must first be expanded. Consider for example the $<\tilde{\rho u}\, r>_{i+\frac{1}{2}jk}$ term.

$$<\tilde{\rho u}\, r>_{i+\frac{1}{2}jk} = (\tilde{ur})_{i+\frac{1}{2}jk}\left[\left(\frac{1}{2} + \xi_1\right)\tilde{\rho}_{ijk} + \left(\frac{1}{2} - \xi_1\right)\tilde{\rho}_{i+1jk}\right]$$

$$= (\tilde{ur})_{i+\frac{1}{2}jk}\left[\frac{1}{2}\left(\tilde{\rho}_{ijk} + \tilde{\rho}_{i+1jk}\right) + \xi_1\left(\tilde{\rho}_{ijk} - \tilde{\rho}_{i+1jk}\right)\right]$$

$$= (\tilde{\rho u}\, r)_{i+\frac{1}{2}jk} + \xi_1\,(\tilde{ur})_{i+\frac{1}{2}jk}\left(\tilde{\rho}_{ijk} - \tilde{\rho}_{i+1jk}\right) \qquad \text{(III-41)}$$

where $\xi_1 = \alpha\,\text{sign}\,(\tilde{u}_{i+\frac{1}{2}jk}) \quad 0 \leq \alpha \leq 1/2$. Therefore

$$\frac{\partial <\tilde{\rho u}\, r>_{i+\frac{1}{2}jk}}{\partial \tilde{p}_{ijk}} = r_{i+\frac{1}{2}}\frac{\partial(\tilde{\rho u})_{i+\frac{1}{2}jk}}{\partial \tilde{p}_{ijk}} + \xi_1\, r_{i+\frac{1}{2}}\,\tilde{u}_{i+\frac{1}{2}jk}\frac{\partial \tilde{\rho}_{ijk}}{\partial \tilde{p}_{ijk}}$$

$$+ \xi_1 \left(\tilde{\rho}_{ijk} - \tilde{\rho}_{i+1jk}\right) r_{i+\frac{1}{2}} \frac{\partial \tilde{u}_{i+\frac{1}{2}jk}}{\partial \tilde{p}_{ijk}} \qquad \text{(III-42)}$$

From Eqs. (III-30) and (III-23), Eq. (III-42) becomes

$$\frac{\partial < \tilde{\rho u}\, r >_{i+\frac{1}{2}jk}}{\partial \tilde{p}_{ijk}} = r_{i+\frac{1}{2}} \frac{\delta t}{\delta r} + \frac{\xi_1 r_{i+\frac{1}{2}} \tilde{u}_{i+\frac{1}{2}jk}}{\gamma A (\tilde{\rho}_{ijk})^{\gamma-1}}$$

$$+ \xi_1 \left(\tilde{\rho}_{ijk} - \tilde{\rho}_{i+1jk}\right) \frac{\partial \tilde{u}_{i+\frac{1}{2}jk}}{\partial \tilde{p}_{ijk}} \qquad \text{(III-43)}$$

To evaluate the one remaining partial derivative, one uses Eqs. (III-23) and (III-30) and the chain rule.

$$\frac{\partial (\rho u)_{i+\frac{1}{2}jk}}{\partial \tilde{p}_{ijk}} = \tilde{u}_{i+\frac{1}{2}jk} \frac{\partial \tilde{\rho}_{i+\frac{1}{2}jk}}{\partial \tilde{p}_{ijk}} + \tilde{\rho}_{i+\frac{1}{2}jk} \frac{\partial \tilde{u}_{i+\frac{1}{2}jk}}{\partial \tilde{p}_{ijk}}$$

$$\frac{\delta t}{\delta r} = \tilde{u}_{i+\frac{1}{2}jk} \frac{\partial\, 1/2 (\tilde{\rho}_{ijk} + \tilde{\rho}_{i+1jk})}{\partial \tilde{p}_{ijk}} + \tilde{\rho}_{i+\frac{1}{2}jk} \frac{\partial \tilde{u}_{i+\frac{1}{2}jk}}{\partial \tilde{p}_{ijk}}$$

or

$$\frac{\partial \tilde{u}_{i+\frac{1}{2}jk}}{\partial \tilde{p}_{ijk}} = \frac{1}{\tilde{\rho}_{i+\frac{1}{2}jk}} \left(\frac{\delta t}{\delta r} - \frac{1}{2} \frac{\tilde{u}_{i+\frac{1}{2}jk}}{\gamma A (\tilde{\rho}_{ijk})^{\gamma-1}}\right) \qquad \text{(III-44)}$$

Combining Eqs. (III-43) and (III-44) one has

$$\frac{\partial < \tilde{\rho u}\, r >_{i+\frac{1}{2}jk}}{\partial \tilde{p}_{ijk}} = r_{i+\frac{1}{2}} \frac{\delta t}{\delta r} + \frac{\xi_1 r_{i+\frac{1}{2}} \tilde{u}_{i+\frac{1}{2}jk}}{\gamma A (\tilde{\rho}_{ijk})^{\gamma-1}}$$

$$+ \frac{2\xi_1 (\tilde{\rho}_{ijk} - \tilde{\rho}_{i+1jk}) r_{i+\frac{1}{2}}}{(\tilde{\rho}_{ijk} + \tilde{\rho}_{i+1jk})} \left(\frac{\delta t}{\delta r} - \frac{1}{2} \frac{\tilde{u}_{i+\frac{1}{2}jk}}{\gamma A (\tilde{\rho}_{ijk})^{\gamma-1}} \right) \tag{III-45}$$

By analogy the other partial derivatives follow.

$$\frac{\partial < \rho u r >_{i-\frac{1}{2}jk}}{\partial \tilde{p}_{ijk}} = - r_{i-\frac{1}{2}} \frac{\delta t}{\delta r} - \frac{\xi_2 r_{i-\frac{1}{2}} \tilde{u}_{i-\frac{1}{2}jk}}{\gamma A (\tilde{\rho}_{ijk})^{\gamma-1}}$$

$$- \frac{2\xi_2 (\tilde{\rho}_{i-1jk} - \tilde{\rho}_{ijk}) r_{i-\frac{1}{2}}}{(\tilde{\rho}_{i-1jk} + \tilde{\rho}_{ijk})} \left(\frac{\delta t}{\delta r} + \frac{1}{2} \frac{\tilde{u}_{i-\frac{1}{2}jk}}{\gamma A (\tilde{\rho}_{ijk})^{\gamma-1}} \right) \tag{III-46}$$

where

$$\xi_2 = \alpha \operatorname{sign} (\tilde{u}_{i-\frac{1}{2}jk}) \quad 0 \leq \alpha \leq 1/2$$

$$\frac{\partial < \tilde{\rho}(\tilde{v} - r\omega) >_{ij+\frac{1}{2}k}}{\partial \tilde{p}_{ijk}} = \frac{\delta t}{r_i \delta \theta} + \frac{\xi_3 \tilde{v}_{ij+\frac{1}{2}k}}{\gamma A (\tilde{\rho}_{ijk})^{\gamma-1}} + \frac{2\xi_3 (\tilde{\rho}_{ijk} - \tilde{\rho}_{ij+1k})}{(\tilde{\rho}_{ijk} + \tilde{\rho}_{ij+1k})}$$

$$\cdot \left(\frac{\delta t}{r_i \delta \theta} - \frac{1}{2} \frac{\tilde{v}_{ij+\frac{1}{2}k}}{\gamma A (\tilde{\rho}_{ijk})^{\gamma-1}} \right) - \frac{(1/2 + \xi_3) r_i \omega}{\gamma A (\tilde{\rho}_{ijk})^{\gamma-1}} \tag{III-47}$$

where

$$\xi_3 = \alpha \operatorname{sign} (\tilde{v}_{ij+\frac{1}{2}} - r_i \omega) \quad 0 \leq \alpha \leq 1/2$$

$$\frac{\partial < \tilde{\rho}(\tilde{v} - r\omega) >_{ij-\frac{1}{2}k}}{\partial \tilde{p}_{ijk}} = -\frac{\delta t}{r_i \delta\theta} - \frac{\xi_4 \tilde{v}_{ij-\frac{1}{2}k}}{\gamma A (\tilde{\rho}_{ijk})^{\gamma-1}} - \frac{2\xi_4 (\tilde{\rho}_{ij-1k} - \tilde{\rho}_{ijk})}{(\tilde{\rho}_{ij-1k} + \tilde{\rho}_{ijk})}$$

$$\cdot \left(\frac{\delta t}{r_i \delta\theta} + \frac{1}{2} \frac{v_{ij-\frac{1}{2}k}}{\gamma A (\tilde{\rho}_{ijk})^{\gamma-1}} \right) - \frac{(1/2 - \xi_4) r_i \omega}{\gamma A (\tilde{\rho}_{ijk})^{\gamma-1}} \qquad \text{(III-48)}$$

where

$$\xi_4 = \alpha \operatorname{sign} (v_{ij-\frac{1}{2}k} - r_i\omega) \quad 0 \leq \alpha \leq 1/2$$

$$\frac{\partial < \tilde{\rho w} >_{ijk+\frac{1}{2}}}{\partial \tilde{p}_{ijk}} = \frac{\delta t}{\delta z} + \frac{\xi_5 \tilde{w}_{ijk+\frac{1}{2}}}{\gamma A (\tilde{\rho}_{ijk})^{\gamma-1}} + \frac{2\xi_5 (\tilde{\rho}_{ijk} - \tilde{\rho}_{ijk+1})}{(\tilde{\rho}_{ijk} + \tilde{\rho}_{ijk+1})} \left(\frac{\delta t}{\delta z} \right.$$

$$\left. - \frac{1}{2} \frac{\tilde{w}_{ijk+\frac{1}{2}}}{\gamma A (\tilde{\rho}_{ijk})^{\gamma-1}} \right) \qquad \text{(III-49)}$$

where

$$\xi_5 = \alpha \operatorname{sign} (w_{ijk+\frac{1}{2}}) \quad 0 \leq \alpha \leq 1/2$$

$$\frac{\partial < \tilde{\rho w} >_{ijk-\frac{1}{2}}}{\partial \tilde{p}_{ijk}} = -\frac{\delta t}{\delta z} - \frac{\xi_6 \tilde{w}_{ijk-\frac{1}{2}}}{\gamma A (\tilde{\rho}_{ijk})^{\gamma-1}} - \frac{2\xi_6 (\tilde{\rho}_{ijk-1} - \tilde{\rho}_{ijk})}{(\tilde{\rho}_{ijk-1} + \tilde{\rho}_{ijk})} \left(\frac{\delta t}{\delta z} \right.$$

$$\left. + \frac{1}{2} \frac{\tilde{w}_{ijk-\frac{1}{2}}}{\gamma A (\tilde{\rho}_{ijk})^{\gamma-1}} \right) \qquad \text{(III-50)}$$

where

$$\xi_6 = \alpha \operatorname{sign} (w_{ijk-\frac{1}{2}}) \quad 0 \leq \alpha \leq 1/2$$

As a first approximation to this improved form one may neglect the terms involving density differences in Eqs. (III-45), (III-46), (III-47), (III-48), (III-49), and (III-50) and substitute the resulting expressions into Eq. (III-40), arriving at a much closer approximation to $\frac{\partial \tilde{D}_{ijk}}{\partial \tilde{p}_{ijk}}$ without much additional complexity.

$$\frac{\partial \tilde{D}_{ijk}}{\partial \tilde{p}_{ijk}} \approx \frac{1}{\delta t\, \gamma A (\rho_{ijk})^{\gamma-1}} + \frac{2\delta t}{\delta r^2} + \frac{2\delta t}{r_i^2\, \delta\theta^2} + \frac{2\delta t}{\delta z^2}$$

$$+ \frac{1}{\gamma A (\tilde{\rho}_{ijk})^{\gamma-1}} \left[\frac{(\xi_1 r_{i+\frac{1}{2}} \tilde{u}_{i+\frac{1}{2}jk} + \xi_2 r_{i-\frac{1}{2}} \tilde{u}_{i-\frac{1}{2}jk})}{r_i\, \delta r} \right.$$

$$\left. + \frac{(\xi_3 v_{ij+\frac{1}{2}k} + \xi_4 v_{ij-\frac{1}{2}k})}{r_i\, \delta\theta} - \frac{(\xi_3 + \xi_4)\,\omega}{\delta\theta} + \frac{(\xi_5 w_{ijk+\frac{1}{2}} + \xi_6 w_{ijk-\frac{1}{2}})}{\delta z} \right]$$

(III-51)

Equation (III-51) is identical to Eq. (III-24) except for the terms in brackets. These terms are all positive definite with the exception of the ω term, which can be positive, zero, or negative. In general the net contribution of the additional terms is positive, serving to slow down the relaxation of the equations and thereby improving the propensity for convergence.

4. Velocity Zeroing

One may want to set the high velocities in the relatively rarefied regions to zero. This procedure does little to effect the physics because of the low fluxes associated with the lower densities of the region; and it does allow the problem to evolve using a greater time step, as well as giving more detail in the velocity vector plots for the more dense fluid areas where the velocities are smaller.

5. Pressure Halving

From Eq. (III-27) one can anticipate a difficulty arising because of possible negative pressure excursions during the phase 2 iterations before convergence has been achieved. It turns out that negative pressures only occur in conjunction with the velocity zeroing scheme described in the preceding section. To avoid the difficulties arising from the resulting negative densities, one simply tests the new pressures calculated each iteration from Eq. (III-31) to determine if any are negative. If a negative pressure occurs, the associated change in pressure is set equal to half the former positive value.

IV. NUMERICAL ACCURACY

A. INTRODUCTION

Finite difference solutions of the partial differential equations are never exact because of the presence of truncation and coarse convergence errors. The truncation terms are generally the greatest source of inaccuracy for calculations in which one is forced to use a coarsely zoned mesh. To aid in determining the numerical accuracy of the three-dimensional code, KORYO, a two-dimensional computer program, TAEBEK, has been developed. Because KORYO and TAEBEK are based on the same fundamental equations, comparison calculations can be easily performed.

KORYO and TAEBEK are both capable of treating initial value problems. Each can be run to a unique final steady state equilibrium configuration. One can compare the final multi-dimensional steady state solutions to a finely resolved one-dimensional hydrostatic equilibrium calculation. If all three calculations agree, our confidence that the numerical solution is in close agreement with the actual solution of the partial differential equations is greatly increased.

B. PROOF TESTING OF TAEBEK

1. Two-Dimensional Time Relaxation to Steady State

Starting from an initial arbitrary non-equilibrium configuration, the two-dimensional TAEBEK code has been used to follow the evolution of a non-rotating, non-conducting, self-gravitating, polytropic fluid to its steady state. From basic physical principles one expects the steady state configuration to be spherical. For this reason the symmetry of the final state provides a qualitative check on the accuracy of the solution.

For this calculation a coarse 10 x 10 mesh is used. An individual cell is a toroid with a square cross section that measures 10^7 cm on each

side. The mass is initially distributed in two regions of space. A uniform density of 1.34 g/cm^3 is put into a cylindrical region that has a radius and a half-height, respectively, of 7×10^7 cm. Everywhere else in the mesh, the density is set to half this value. The resulting total mass of the system is 5.65×10^{24} g. The adiabatic-parameter, A, in the polytropic equation of state is held at a constant value of 10^9 $cm^{7/2}/g^{\frac{1}{2}} s^2$, γ is 3/2, and the kinematic viscosity is 10^{12} cm^2/s.

Figures 4 and 5 are contour plots of the density and gravitational potential at four selected times during the collapse. The r axis is horizontal; the z axis, vertical. The origin of the coordinate system and the center of the fluid body is at the lower left of the plots at the intersection of the axes. That is, one is looking at only the upper quadrant of the body. $Z = 0$ is a plane of symmetry; $r = 0$, an axis of symmetry.

In Fig. 4a at $t = 0$ s, the initial configuration is shown by the single contour line. The circular segment that has been drawn over some of the contours is present to allow one to better assess departures from spherical symmetry. Based on the decrease in total kinetic energy, the system is assumed to be in equilibrium at $t = 26{,}000$ s. The excellent agreement with spherical symmetry at this time occurs despite the coarseness of the zoning. The innermost contour at later times is a straight line because of the coarseness of the zoning. The evolution of the gravitational potential in Fig. 5 is similar, although visibly less dramatic.

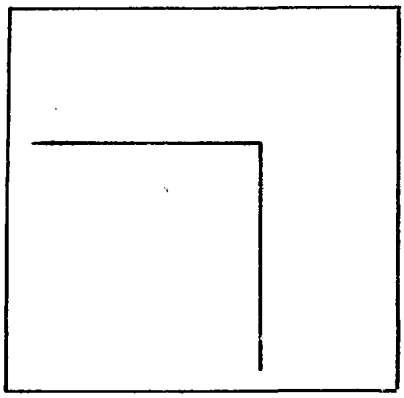

T = 0 sec

A.

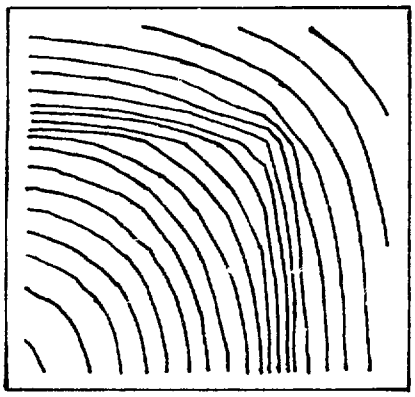

T = 1000 sec

B.

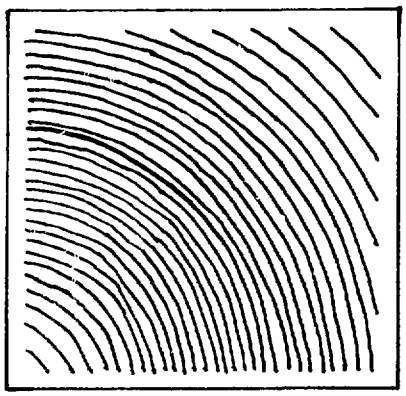

T = 10,000 sec

C.

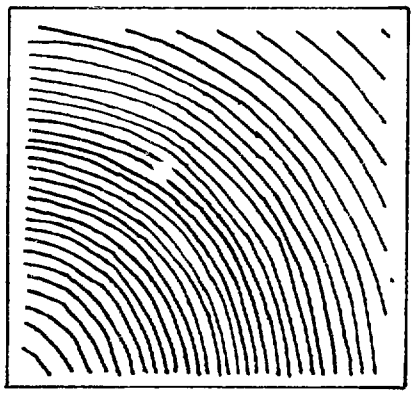

T = 26,000 sec

D.

DENSITY (g/cm^3)

FIGURE 4

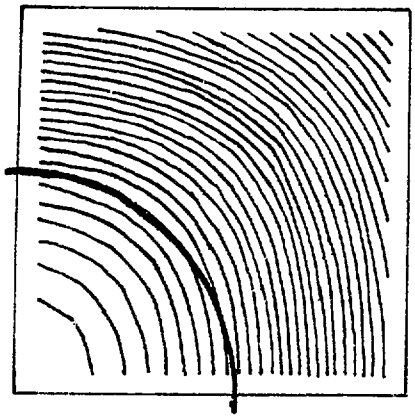

T = 100 sec
A.

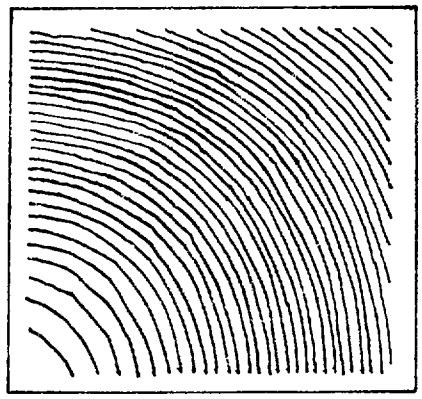

T = 1000 sec
B.

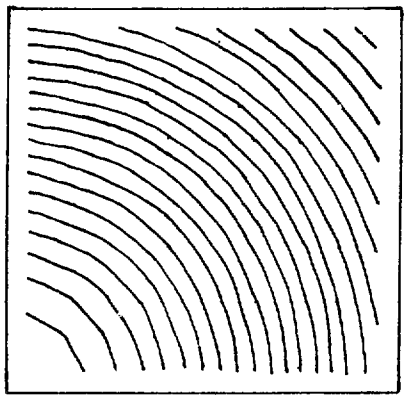

T = 10,000 sec
C.

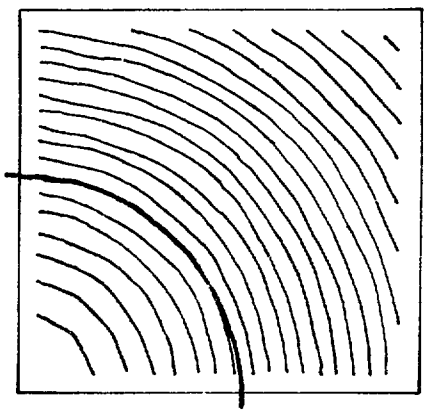

T = 26,000 sec
D.

GRAVITATIONAL POTENTIAL (ergs/g)

FIGURE 5

2. One-Dimensional Hydrostatic Equilibrium

In steady state the self-gravitating fluid body of the preceding section is spherically symmetric. Under such conditions one can solve for spatial density and gravitational potential profiles in a straightforward manner. In steady state the radial momentum equation reduces to the following simple form.

$$\frac{\partial p}{\partial r} = - \rho \frac{\partial \psi}{\partial r} \quad . \tag{IV-1}$$

Since the adiabatic-parameter is assumed to be constant, the equation of of state can be used to eliminate p from the above equation. After rearranging, the result is

$$\frac{\partial \psi}{\partial r} = - \frac{A \gamma}{\gamma - 1} \frac{\partial \rho^{\gamma-1}}{\partial r} \tag{IV-2}$$

Equation (IV-2) can be used in conjunction with the one-dimensional Poisson's equation for the gravitational potential to solve for ρ and ψ. In spherical coordinates one has

$$\frac{1}{r^2} \frac{\partial}{\partial r} \left(r^2 \frac{\partial \psi}{\partial r} \right) = 4\pi G \rho \tag{IV-3}$$

Substituting Eq. (IV-2) into Eq. (IV-3) and rearranging

$$- \frac{1}{r^2} \frac{\partial}{\partial r} \left(r^2 \frac{\partial \rho^{\gamma-1}}{\partial r} \right) = c_1 \rho \tag{IV-4}$$

where

$$c_1 \equiv \frac{4\pi G(\gamma-1)}{\gamma A} \quad .$$

Equation (IV-4) is a nonlinear second order partial differential equation that can be easily solved numerically. If one centers the variables as in the two-dimensional code; and if one defines an analogous indexing scheme, as depicted graphically in Fig. 6, the finite difference form of Eq. (IV-4) is

$$\frac{1}{\delta r^2}\left\{ r^2_{i+\frac{1}{2}} \left[(\rho_{i+1})^{\gamma-1} - (\rho_i)^{\gamma-1}\right] - r^2_{i-\frac{1}{2}} \left[(\rho_i)^{\gamma-1} - (\rho_{i-1})^{\gamma-1}\right] \right\}$$

$$= - r_i^2 \, c_1 \, \rho_i \qquad \text{(IV-5)}$$

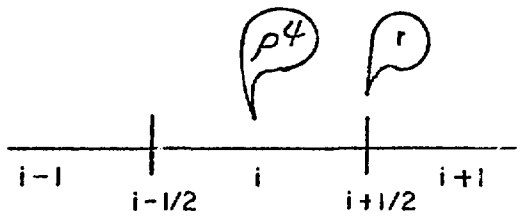

FIGURE 6

Equation (IV-5) can be solved algebraically for ρ_{i+1}. The result is

$$\rho_{i+1} = \left\{ \frac{r_{i-\frac{1}{2}}^2 \left[(\rho_i)^{\gamma-1} - (\rho_{i-1})^{\gamma-1}\right] - \delta r^2 \, r_i^2 \, c_1 \, \rho_i}{r_{i+\frac{1}{2}}^2} + (\rho_i)^{\gamma-1} \right\}^{1/\gamma-1} \tag{IV-6}$$

One now obtains $\psi(r)$ from the finite-difference form of Eq. (IV-2)

$$\psi_{i+1} = \psi_i + \frac{A\,\gamma}{\gamma - 1}\left[(\rho_i)^{\gamma-1} - (\rho_{i+1})^{\gamma-1}\right] \tag{IV-7}$$

To generate the solution from Eqs. (IV-6) and (IV-7) one needs the central density (ρ_c), the central scalar potential (ψ_c), the constant adiabatic-parameter, and boundary conditions that result from the assumption of axial symmetry. That is,

$$\rho_2 = \rho_c \; ; \quad \psi_2 = \psi_c \; ; \quad \rho_1 = \rho_2 \tag{IV-8}$$

3. Comparison of the One- and Two-Dimensional Results

The one- and two-dimensional calculations are compared graphically in Fig. 7. The solution along the axis agrees very well with the one-dimensional result. The solution along the radius agrees nearly as well. The apparent asymmetry in the two-dimensional result is due to the coarseness of the calculational mesh. In Fig. 7b one sees that for this series of calculations the gravitational potential has been normalized to zero at the center of the body.

Subsequent to the completion of this development for methodological check purposes, a publication[62] has appeared that also addresses

one-dimensional hydrostatic equilibrium with a finite difference scheme. Although the detailed numerical techniques differ slightly, the solutions produced by the respective schemes are virtually identical.

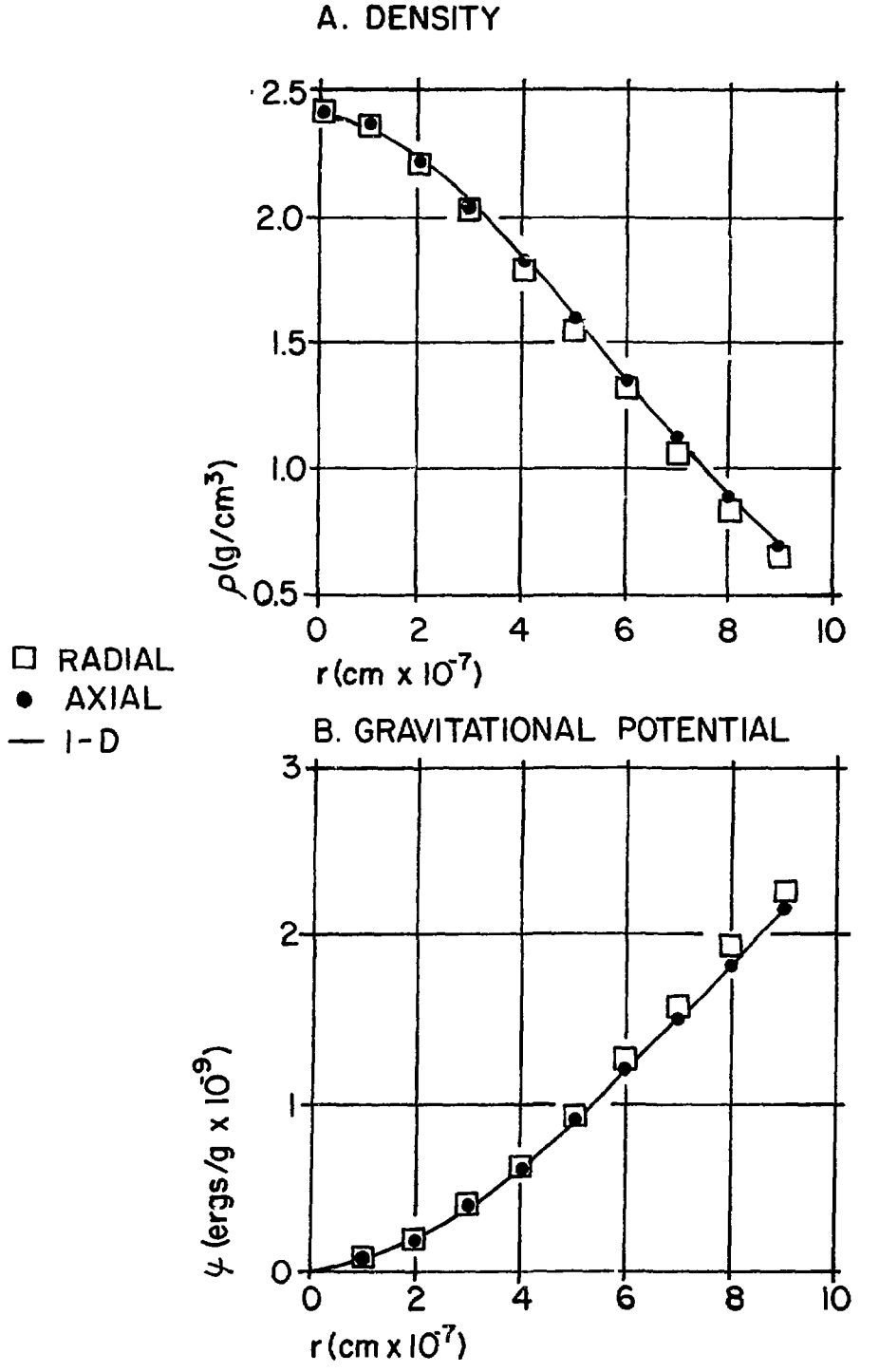

HYDROSATIC EQUILIBRIUM

FIGURE 7

4. Numerical Viscosity Parameter Study

In Chapter III, Sec. I the numerical stability constraints on the kinematic viscosity have been described. There are also physical considerations that can influence the selection of an appropriate viscosity. In many applications one wishes to begin with a self-gravitating body in equilibrium and to study phenomena resulting from various perturbations to steady state. In such cases the transient dynamic phases in the approach to equilibrium are not of interest, and one is free to select non-physical viscosities merely to expedite the development of the desired steady state.

Fluids can behave in ways analogous to harmonic oscillators. If the kinematic viscosity exceeds a certain critical value, the system is overdamped; and equilibrium is approached very slowly because of the large frictional resistance to fluid flow. If on the other hand, the system is severely underdamped, it will oscillate about the equilibrium configuration essentially forever. The goal then is to select a viscosity that does not prove overly restrictive on the time step and that is not too far removed from the critical value of the physical system.

For these reasons a study has been made to consider the effect of viscosity on the self-gravitating fluid sphere described in Sec. IVB. Each calculation is made using a numerical viscosity that is constant over the entire mesh. The viscous stress components assumed in this study are those taken from the stress tensor appropriate for an incompressible fluid (Eqs. (II-11), (II-12), and (II-13)).

One begins by perturbing the hydrostatic equilibrium configuration with an angular momentum step function. The fluid is given a sudden solid body distribution of angular momentum and is allowed to expand under the

action of centrifugal force for 1300 seconds. The angular velocities are then re-zeroed, and the now slightly oblated body is allowed to collapse back to its original equilibrium configuration. To monitor the approach to equilibrium, the total kinetic energy is studied as a function of time. The process is repeated for four different viscosities.

The results of the study are summarized graphically in Fig. 8. The plots begin at the time when the rotation is turned off. In 1300 sec the body has not reached rotational equilibrium. The initial decrease in kinetic energies reflects the removal of the centrifugal force driving the expansion and the subsequent deceleration of the fluid. Gravity turns the velocities around and the now unstable mass distribution accelerates toward the former equilibrium configuration. If the system is not overdamped, the fluid overshoots the equilibrium point because of the newly acquired linear momentum and oscillates about it with an e-folding time dependent on the magnitude of the viscosity.

Figures 8a ($\nu = 5 \times 10^{10}$ cm^2/s) and 8b ($\nu = 10^{11}$ cm^2/s) have the same period of oscillation and have similar amplitude decay rates. The dash-dot line in Fig. 8b is a fit to the trace using the analytic form for a damped linear harmonic oscillator.* The free parameters in the fit are the decay rate and the frequency. The agreement is comforting, although

---

* The equation of motion of a damped linear harmonic oscillator is

$$\ddot{x} = - k^2 x - \lambda \dot{x}$$

where k^2 is the spring constant; λ, the frictional term; and x, the displacement. Solving, one has for the real part

$$x = x_0 \, e^{-\lambda/2(t - t_0)} \cos \omega (t - t_0)$$

where $\omega = \pi/(4k^2 - \lambda^2)^{\frac{1}{2}}$

only qualitative agreement is to be expected. In Fig. 8c the viscosity of 4×10^{11} cm^2/s is approaching the critical value. Figure 8d shows the system to be overdamped at a viscosity of 10^{12} cm^2/s.

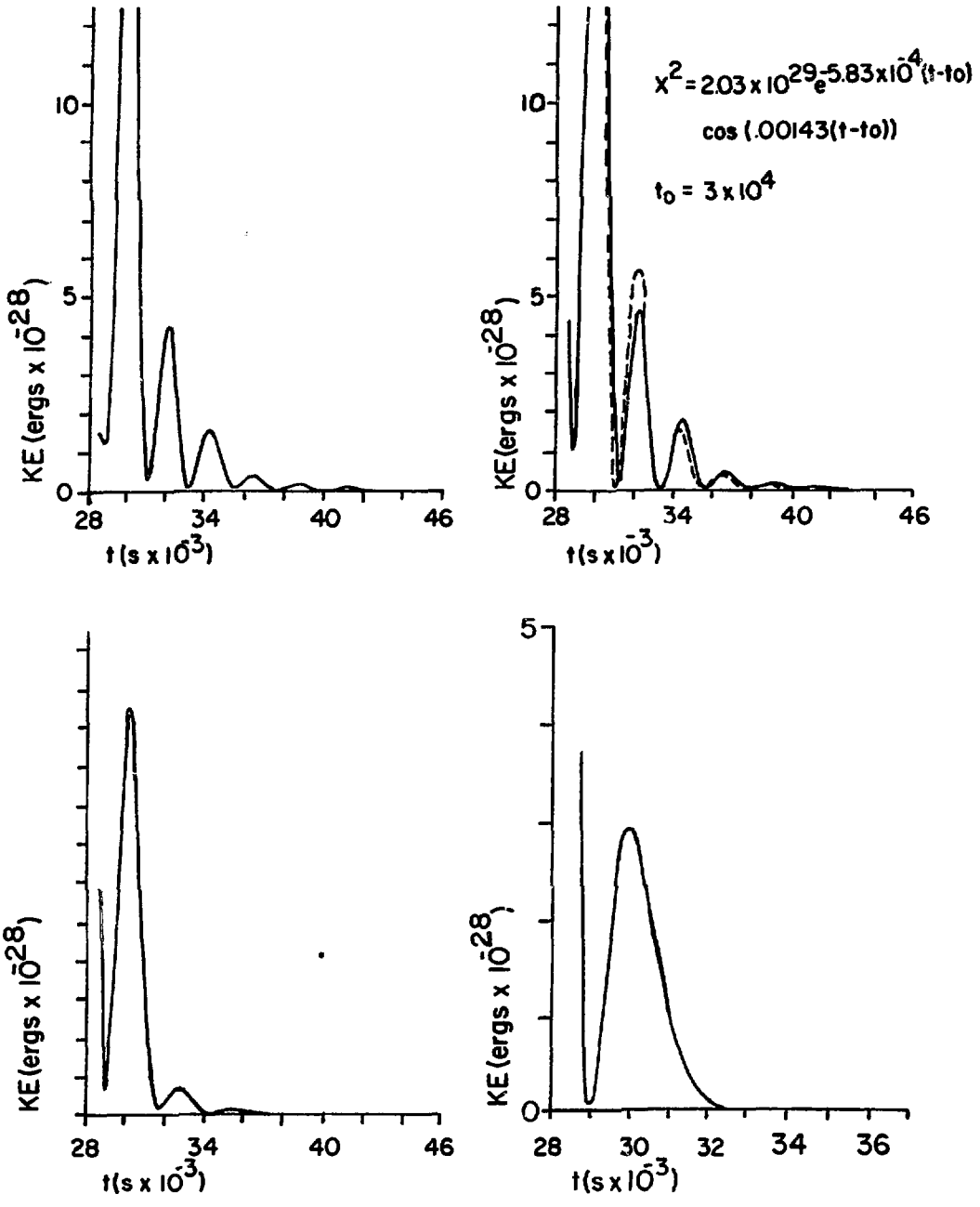
KE (ergs x 10^-28)
t (s x 10^-3)
0
5
10
28
34
40
46
x^2 = 2.03 x 10^29 e^-5.83x10^-4 (t-to)
cos (.00143(t-to))
t_o = 3 x 10^4
30
32
36

FIGURE 8

C. PROOF TESTING OF KORYO

1. Symmetry Considerations

The two-dimensional code, TAEBEK, and the three-dimensional code, KORYO, are based on very similar methodologies; and, when symmetry allows, they can be used to address identical problems. The methodological checkout of TAEBEK has already been described in the preceding sections of this chapter. To test KORYO, one compares it to its predecessor by solving a problem with axial symmetry.

An obvious question regarding the methodology of KORYO relates to its ability to maintain axial symmetry if the nature of the problem demands that it do so. This question has been addressed by two separate parameter studies involving the tightness of convergence imposed, respectively, on the iterative solution of Poisson's equation for the gravitational potential and on the iterative solution of the equations of motion. From these studies one concludes that the convergence criteria for the former must be rather strict, and that for the latter it need not be so severe.

The above result is fortunate because the iterative relaxation process used to determine the gravitational potential is very fast, and the increased fraction of time spent in this phase of the calculation due to the required close convergence is minimal. One reason why this convergence restraint on the potential does not require a large number of additional iterations has already been discussed in Chapter II, Sec. D; i.e., the initial guess to the gravitational potential is very good in a rotating frame. For the iterative relaxation of the equations of motion, the number of iterations required is, of course, a strong function of the dynamics of the system. Since this phase of each calculational cycle is

one of the most time consuming parts, it would have been costly in total problem running time had the axial symmetry been overly sensitive to the convergence of the phase 2 solutions.

2. Three-Dimensional Time Relaxation to Steady State

A natural choice for a comparison calculation is the problem already described. The outer dimensions of the problems are the same; however, because of the central boundary core in the three-dimensional mesh, the specific zoning in KORYO must be somewhat different. A $5 \times 12 \times 5$ mesh with $\delta r = 5/3 \times 10^7$ cm, $\delta\theta = 2\pi/12$, and $\delta z = 2 \times 10^7$ cm has been selected. The calculations are started with different initial conditions from those used in the TAEBEK calculation. No artificial axial symmetry constraints have been imposed on KORYO, i.e., the calculation is fully three-dimensional.

In Fig. 9 KORYO density contours in both the r-θ and the r-z planes are presented at very early times. The initially uniform mass distribution has begun to collapse under self-gravity. The concentration of contours near the outer boundaries indicates that the mass in these regions is being drawn rapidly inward. At the late time represented in Fig. 10 the contours are evenly distributed throughout the mesh, and the body has reached a symmetric steady state.

Figures 11 and 12 summarize the evolution of the gravitational potential. When the mass becomes more centrally concentrated, the potential well deepens as one would expect. The influence of the core on the gravitational potential is very clearly demonstrated by the contour plots in the r-z plane. The effect of the core is more pronounced at the origin of the coordinate system than it is farther up the z-axis. The implication is that the influence of the core is configuration dependent

and that the greatest effect results when the body is concentrated near the origin. This point is discussed in a subsequent part of this section.

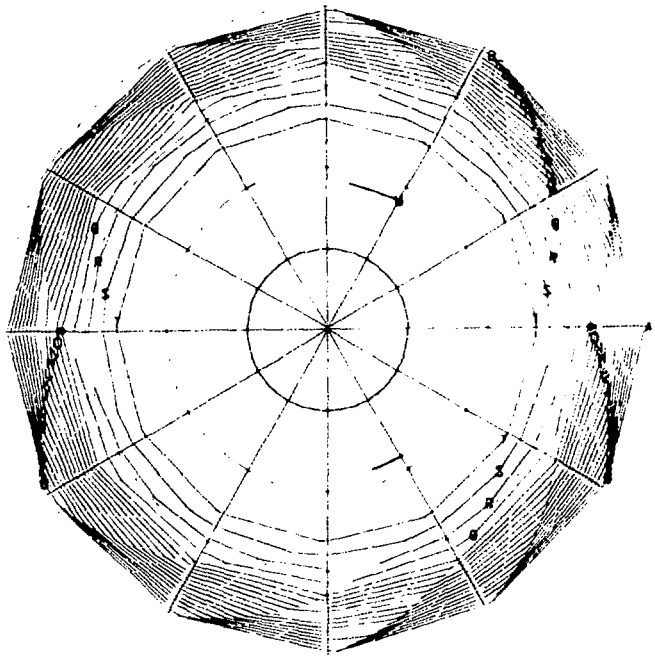

Λ	0.647
U	1.004
Δρ	0.008

r-θ Plane
a

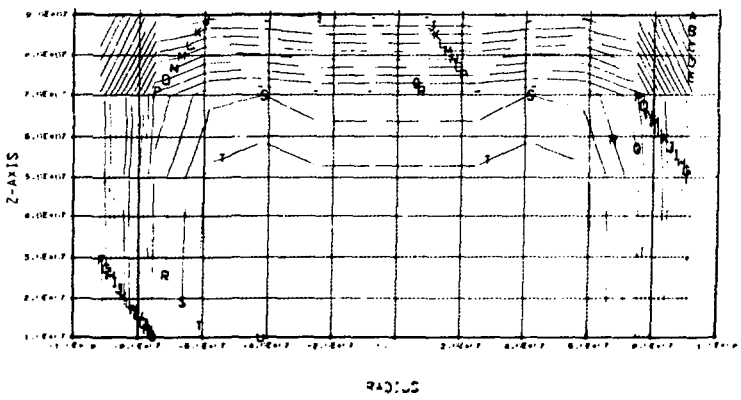

Λ	0.804
U	1.004
Δρ	0.010

r-z Plane
b

$t = 4.06 \times 10^2$ s
Density(g/cm^3)
FIGURE 9

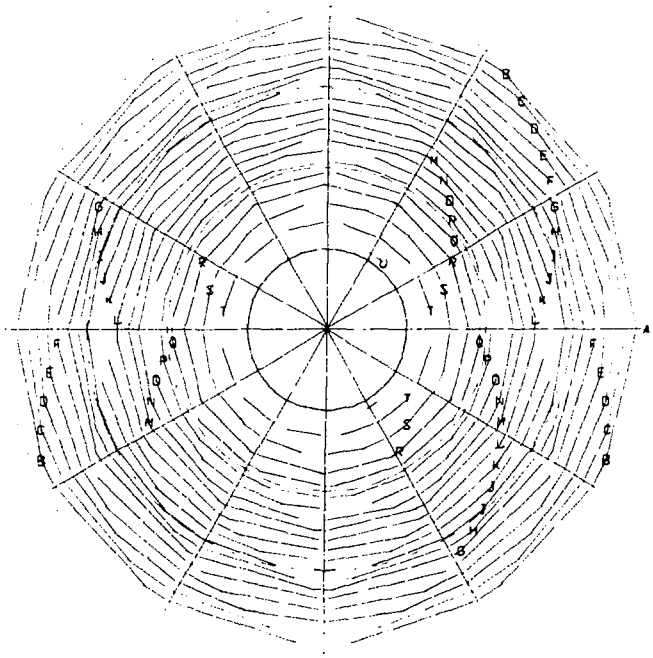

A	0.779
U	2.045
Δρ	0.063

r-θ Plane
a

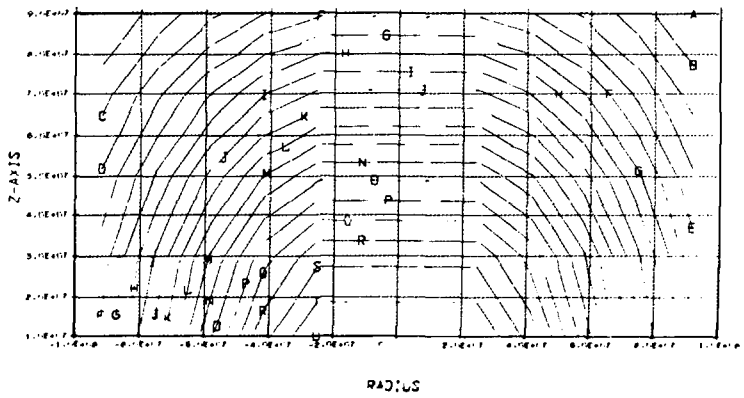

A	0.335
U	2.045
Δρ	0.085

r-z Plane
b

$t = 4.58 \times 10^4$ s
Density(g/cm^3)
FIGURE 10

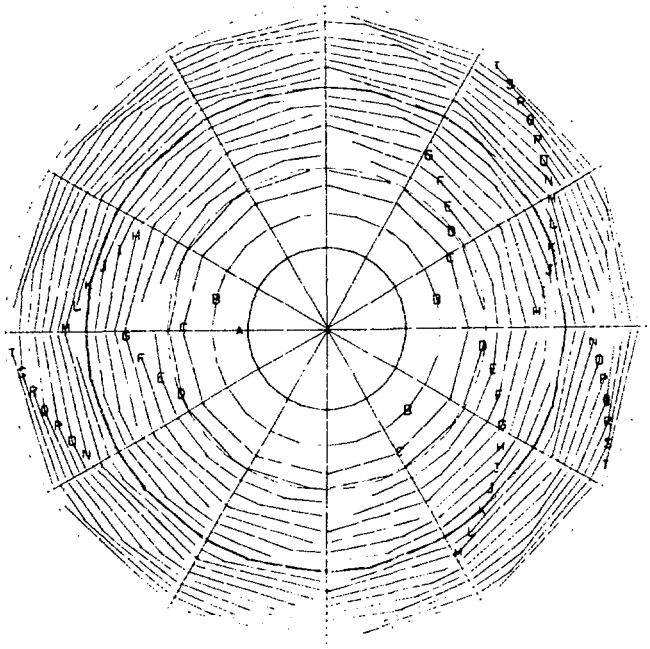

A	-4.71×10^9
T	-3.28×10^9
$\Delta\psi$	-0.07×10^9

r-θ Plane
a

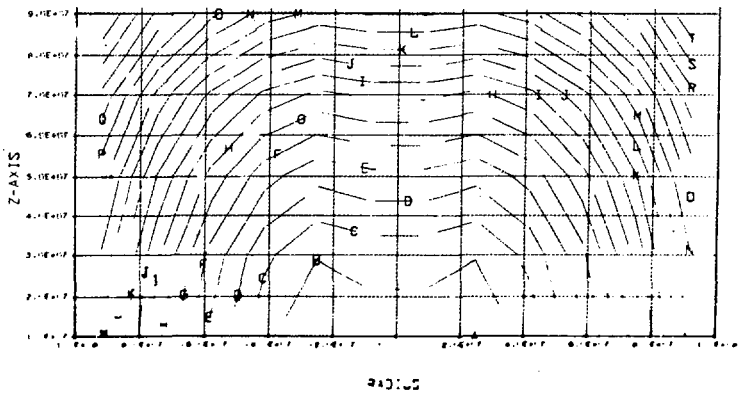

A	-4.79×10^9
U	-3.10×10^9
$\Delta\psi$	-0.08×10^9

r-z Plane
b

$t = 4.00 \times 10^2$ s
Gravitational Potential(ergs/g)
FIGURE 11

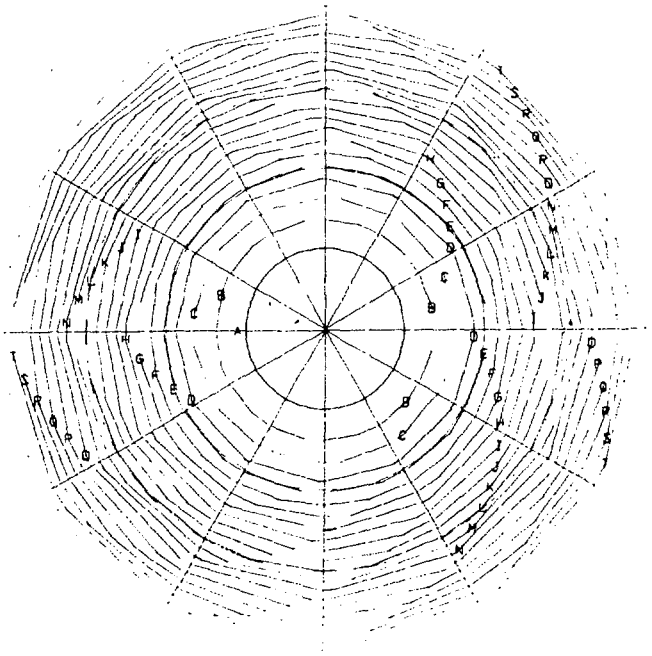

A -5.50×10^9
T -3.38×10^9
$\Delta\psi$ -0.11×10^9

r-θ Plane
a

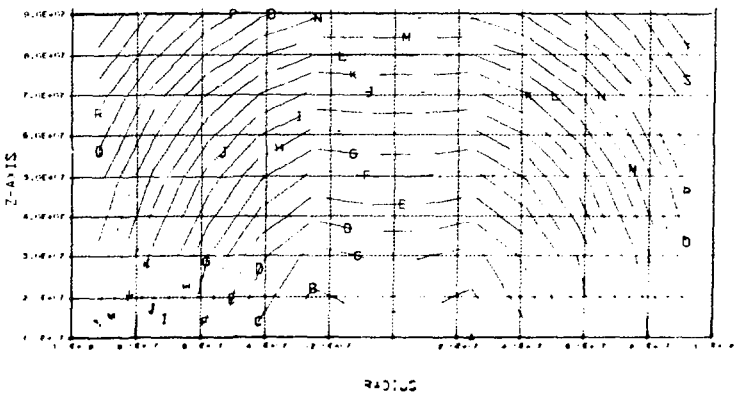

A -5.57×10^9
U -3.01×10^9
$\Delta\psi$ -0.13×10^9

r-z Plane
b

$t = 4.58 \times 10^4$ s
Gravitational Potential(ergs/g)
FIGURE 12

3. Comparison of the Two- and Three-Dimensional Results

A more quantitative comparison of the two- and three-dimensional calculations is provided by the profiles of density and gravitational potential presented in Figs. 13, 14, and 15. The comparison of TAEBEK with the one-dimensional hydrostatic equilibrium calculation presented earlier in this chapter is for a 10 x 10 mesh. The KORYO calculation discussed in this section uses much coarser zoning. For these reasons Figs. 13 and 14 include a comparison between a TAEBEK calculation that employs a 5 x 5 mesh and one that uses a 10 x 10 mesh. The resulting profiles are in excellent agreement; therefore, the zoning differences do not enter significantly into the interpretation given below.

The density and gravitational potential profiles calculated with KORYO are in fairly good agreement with those produced with TAEBEK. The lower central density predicted by KORYO is a result of the massless core and the resulting higher gravitational potential in proximity to it. Naturally, the worst agreement results when one looks up along the z-axis in zones immediately adjacent to the core. In Fig. 15 the gravitational potentials are compared for a rotating self-gravitating body to demonstrate that as the system becomes less centrally condensed, the effect of the core is reduced. For the class of physical systems, that this methodology is specifically designed to address, the effect of a central massless core seems to be of relatively minor consequence.

The effect of the central core is related to the fraction of the total mass excluded from the system by its presence. The magnitude of the effect is therefore inversely proportional to the number of radial zones. That is, the influence of the massless core in a calculation using 10 radial zones instead of the 5 described in these check cases is reduced

by about a factor of two. All of the protostar models reported in Chapter V and VI do in fact use the finer radial zoning. The effect of truncation errors and the convergence of the numerical solutions are discussed in more detail in Appendix C.

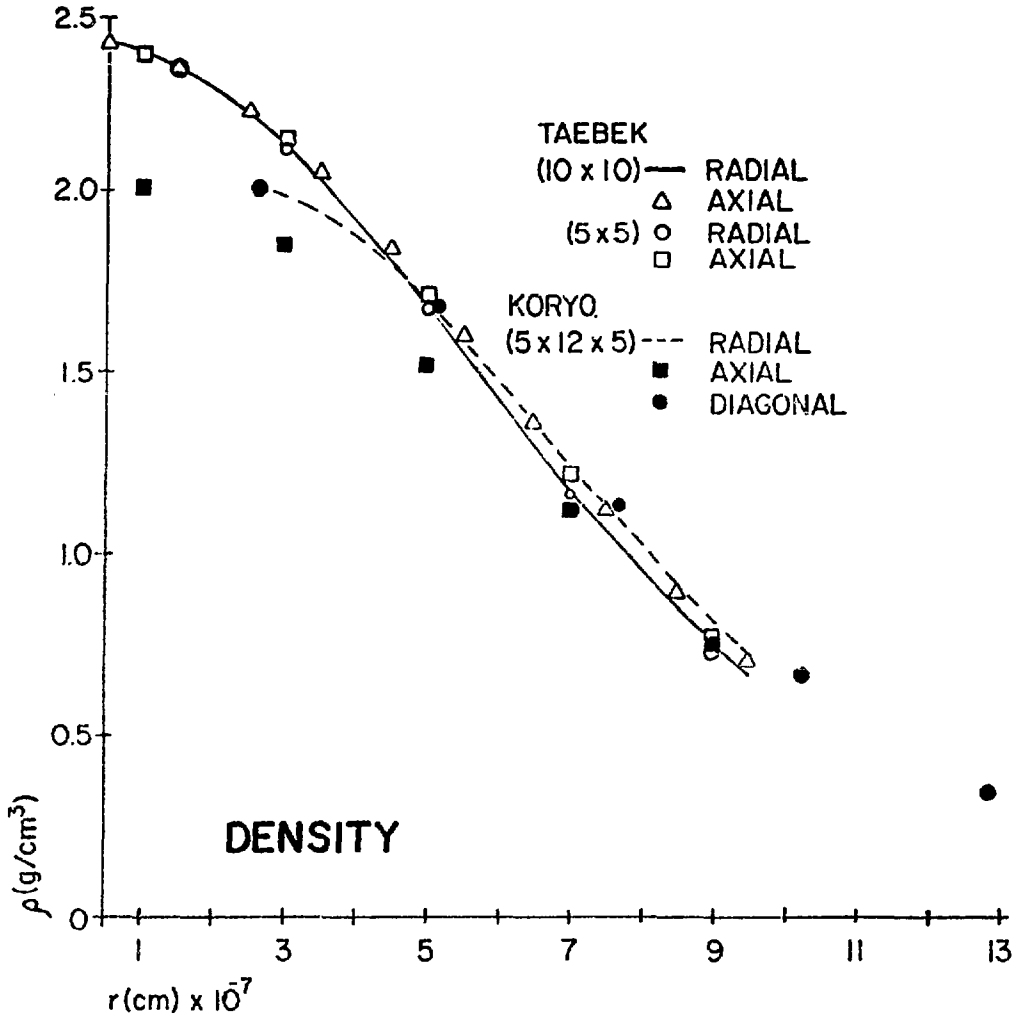
2.5
2.0
1.5
1.0
0.5
0
TAEBEK
(10 x 10) RADIAL
AXIAL
(5x5) RADIAL
AXIAL
KORYO
(5 x 12 x 5) RADIAL
AXIAL
DIAGONAL
DENSITY
ρ(g/cm³)
1
3
5
7
9
11
13
r(cm) x 10⁻⁷

FIGURE 13

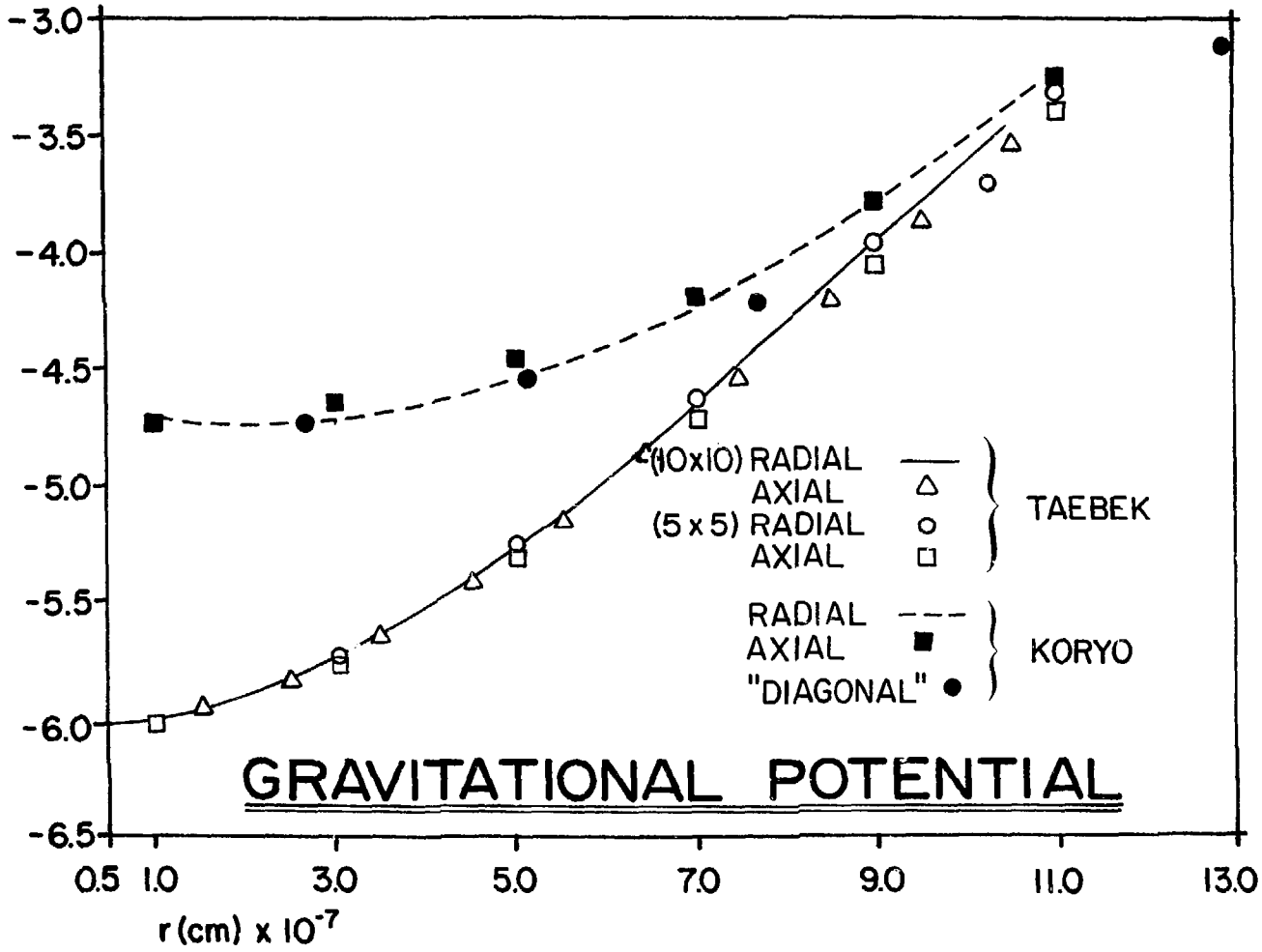
-3.0
-3.5
-4.0
-4.5
-5.0
-5.5
-6.0
-6.5
0.5
1.0
3.0
5.0
7.0
9.0
11.0
13.0
r (cm) x 10^-7
(10x10) RADIAL
AXIAL
(5 x 5) RADIAL
AXIAL
TAEBEK
RADIAL
AXIAL
"DIAGONAL"
KORYO
GRAVITATIONAL POTENTIAL

FIGURE 14

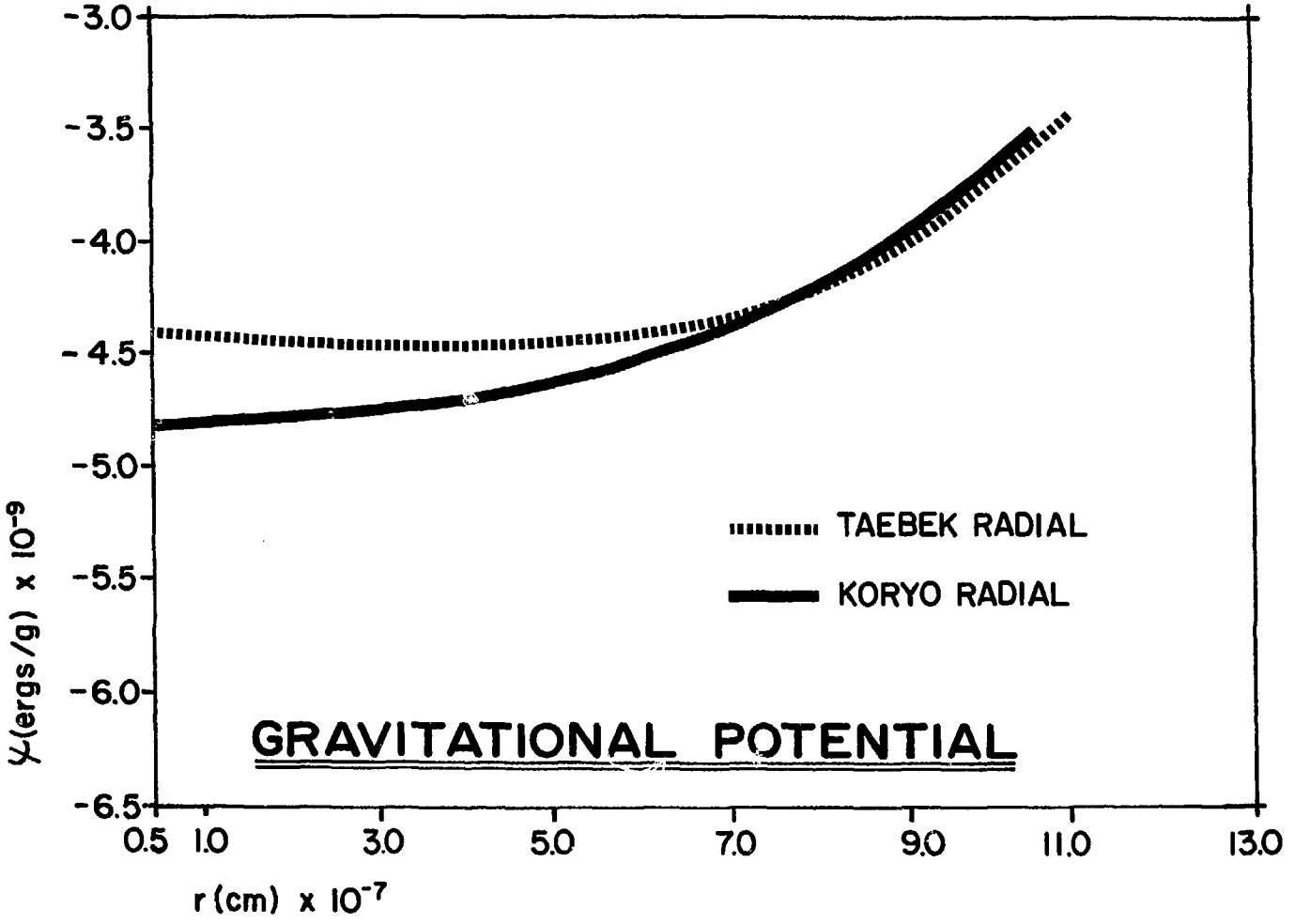
-3.0
-3.5
-4.0
-4.5
-5.0
-5.5
-6.0
-6.5
ψ(ergs/g) x 10⁻⁹
0.5
1.0
3.0
5.0
7.0
9.0
11.0
13.0
r (cm) x 10⁻⁷
TAEBEK RADIAL
KORYO RADIAL
GRAVITATIONAL POTENTIAL

FIGURE 15

V. COLLAPSE OF A ROTATING INTERSTELLAR CLOUD

A. INTRODUCTION

As a first step in the study of the dynamics of protostellar evolution, we have examined the formation of toroids from uniform and from nonuniform distributions of interstellar gas. As discussed in Chapter I, several other workers have studied the same problem and have come to contradictory conclusions. In every case the calculations, upon which the conclusions are based, have been two-dimensional, with forced axial symmetry. Our goals with the fully three-dimensional calculations have been

1) to investigate whether or not stable toroidal rings can be formed from the collapse of a three-dimensional configuration
2) to see if the formation of such rings can be inhibited or prevented by the existence of perturbations in the initial gaseous distribution

In selecting initial conditions one uses the limited observational guidance available. The assumption is made that the early protostar can be modelled by a cylindrical region of space, characterized by an average uniform density. The dimensions of the cylinder are chosen to be consistent with the size of observed dark globules and other dense interstellar clouds.[63] The primordial cloud is assumed to be initially in solid body rotation with a counterclockwise sense. In choosing a rate of rotation one is guided by the observation that neither the stellar rotation axes nor the axes of binary systems show any preferred orientation relative to the galactic plane. This random orientation implies that the rotational motions originated in random turbulent motions in the interstellar medium and that the rotational velocities

of protostellar clouds are comparable to the measured translational velocities.[64] One therefore chooses angular velocities greater than or approximately equal to galactic rotation rates.

The collapse calculations have been performed in a grid that has 10 radial, 12 azimuthal and 5 axial cells resolving the space above an equatorial plane across which symmetry has been assumed. The 12 azimuthal zones divide the region into 30° segments. In an r-z plane the cell surfaces are rectangles. The axial dimension of a zone is 1.4×10^{16} cm; the radial dimension is exactly one-half the axial value. The upper boundary is 7.0×10^{16} cm above the reflecting plane. The inner radial boundary required by the central core and the outer radial boundary are 7.0×10^{15} cm and 7.7×10^{16} cm, respectively, from the axis of rotation.

The results are summarized using contour plots of density, gravitational potential, and angular velocity in both the r-θ and the r-z planes. The r-θ plane contours represent conditions in the equatorial plane. Plots in the r-z plane are selected to pass through the most massive azimuthal ray of the system. Velocity and momentum-density vector fields in the r-θ and r-z planes, as referred to both the laboratory and the rotating frames, are used to summarize fluid motions. All vectors originate at cell centers; so the tails can be easily identified either by visual inspection or by using a straight edge to line them up. The r-θ plane vector plots contain linearly interpolated additional azimuthal rays of two different lengths to fill in the diverging areas, facilitating pattern identification.

A density, called the maximum interpolated density, and a radius, called the position of maximum interpolated density, are used to

summarize the time evolution of a system. These variables are given the symbols ρ'_{max} and $R_{\rho'_{max}}$, respectively. They are obtained from a three-point parabolic fit to the maximum cell density and the two adjacent densities. Except where specifically indicated, all quantities are reported in the cgs system of units.

B. RING CHARACTERIZATION

1. Assumptions and Constraints

The literature on equilibrium rings, as well as the generally restrictive assumptions upon which these works are based, is summarized in Chapter I. We continue to assume that a polytropic gas equation of state is valid. One is constrained by the calculational mesh to studying rings that have dimensions comparable to or greater than the dimensions of an individual cell. The viscosity chosen for the calculations is limited to that amount necessary for numerical stability; therefore, the systems are not significantly constrained from rotating differentially. Examples of the patterns of differential rotation that develop in the various calculations are presented in the form of angular velocity contours referred to the laboratory frame.

The only symmetry constraint imposed on the system is the reflecting plane at $z = 0$. This assumption limits the problems one can address to a specific, but rather large, class. The reflecting plane can be easily removed at the expense of increased computing times or of reduced spatial resolution.

We reemphasize the three-dimensionality of the calculations. With the finite difference techniques used throughout, the potential surfaces and the mass configurations of highly distorted objects can be

more accurately determined than with any analytical solutions that are currently available. The distortion scales of interest must, however, be comparable to or greater than the computational zone size if they are to be resolved.

2. Geometric Properties

To describe the structural appearance of a ring, one needs to consider two separate geometric features. The radius of the toroid, defined as the distance from the axis of rotation to the maximum density contour, is the first of these features. Figure 16 graphically illustrates this concept. The second feature depends on the cross-sectional characteristics of the region of high mass concentration in the ring. If the configuration is that of a circular toroid, one can characterize the cross section by a single linear dimension, the radius of the circular cross section. In general, rotating rings are flattened into the equatorial plane; so the cross sections can not even be accurately represented as ellipses with well-defined major and minor axes. One therefore defines an average dimension, which in all subsequent sections is called the characteristic cross-sectional radius, a, of the ring. To determine $\underline{a}$ for distorted toroidal systems one measures the diameter of the ring in the equatorial plane, divides by two, and averages this result with the measured axial radius. The cross-sectional radius of a ring section is graphically illustrated in Figure 16.

The radius, R, of a toroid is a uniquely and well-defined concept if one uses the definition given above. The characteristic cross-sectional radius, on the other hand, requires that one know the location of the ring surface. As a matter of convention we define the

surface of the ring to lie on the contour that represents one order of magnitude decrease from the maximum density in the ring.

Both of the geometric features described above depend in a complicated way on the partitioning of energy in the system. The radius of the toroid is most sensitive to the gravitational potential energy and to the kinetic energy of rotation. The characteristic cross-sectional radius of the ring is likewise influenced by these energies; but in addition, the area and shape of the ring depend very strongly on the thermal pressure.

The geometric characteristics of rotating toroids result from a very complicated interaction of centrifugal and gravitational forces with forces arising from the internal thermal pressures of the ring. As a means for estimating the characteristic cross-sectional radius, one assumes that a section of the toroid can be represented by an infinite cylinder; and one non-dimensionalizes the cylindrical equation of hydrostatic equilibrium. Combining Eqs. (II-14), (IV-1), and the one-dimensional form of Eq. (II-15) and expanding the inner radial derivative, one has

$$-\frac{\gamma A}{r}\frac{\partial}{\partial r}\left(r\,\rho^{\gamma-2}\frac{\partial \rho}{\partial r}\right) = 4\pi G\rho \qquad \text{(V-1)}$$

Defining the following change of variables

$$r = ax \qquad \text{(V-2)}$$

$$\rho = \left(\frac{M}{a^3}\right) f$$

Substituting Eq. (V-2) into Eq. (V-1) and rearranging, one obtains

$$\frac{1}{x}\,\frac{\partial}{\partial x}\left(x\, f^{\gamma-2}\,\frac{\partial f}{\partial x}\right) = -\,\frac{4\pi G}{\gamma A}\,\frac{a^{3\gamma-4}}{M^{\gamma-2}}\, f \qquad \text{(V-3)}$$

The dimensionless quantity above can be scaled by writing

$$\frac{4\pi G}{\gamma A}\,\frac{a^{3\gamma-4}}{M^{\gamma-2}} = \frac{4\pi}{\gamma}\,\lambda \qquad \text{(V-4)}$$

where λ is a free scaling factor. Setting $\gamma = 5/3$ and solving for $\underline{a}$, one has

$$a = \lambda\,\frac{A}{GM^{1/3}} \qquad \text{(V-5)}$$

Once the free scaling parameter is chosen, Eq. (V-5) provides a very convenient and surprisingly consistent means for predicting the characteristic cross-sectional radius of a self-gravitating system. The selection of the free-scaling parameter, λ, is discussed in Section G of Chapter VI.

In the following discussions, systems are classified as dispersed, intermediate, or compact purely as a matter of convenience. A dispersed gas is characterized by thermal pressures that significantly resist local self-gravity. For a fixed ratio of specific heats the designation can be qualitatively defined in terms of the entropy variable, A. Systems with higher values of A are more dispersed than those having lower values. Dispersed toroids are those for which the characteristic cross-sectional radius, a, of the ring is comparable to the radius, R, of the toroid. Compact toroids are those for which $\underline{a}$ is much less than R. Intermediate toroids lie in between.

CHARACTERIZATION OF ROTATING TOROIDS

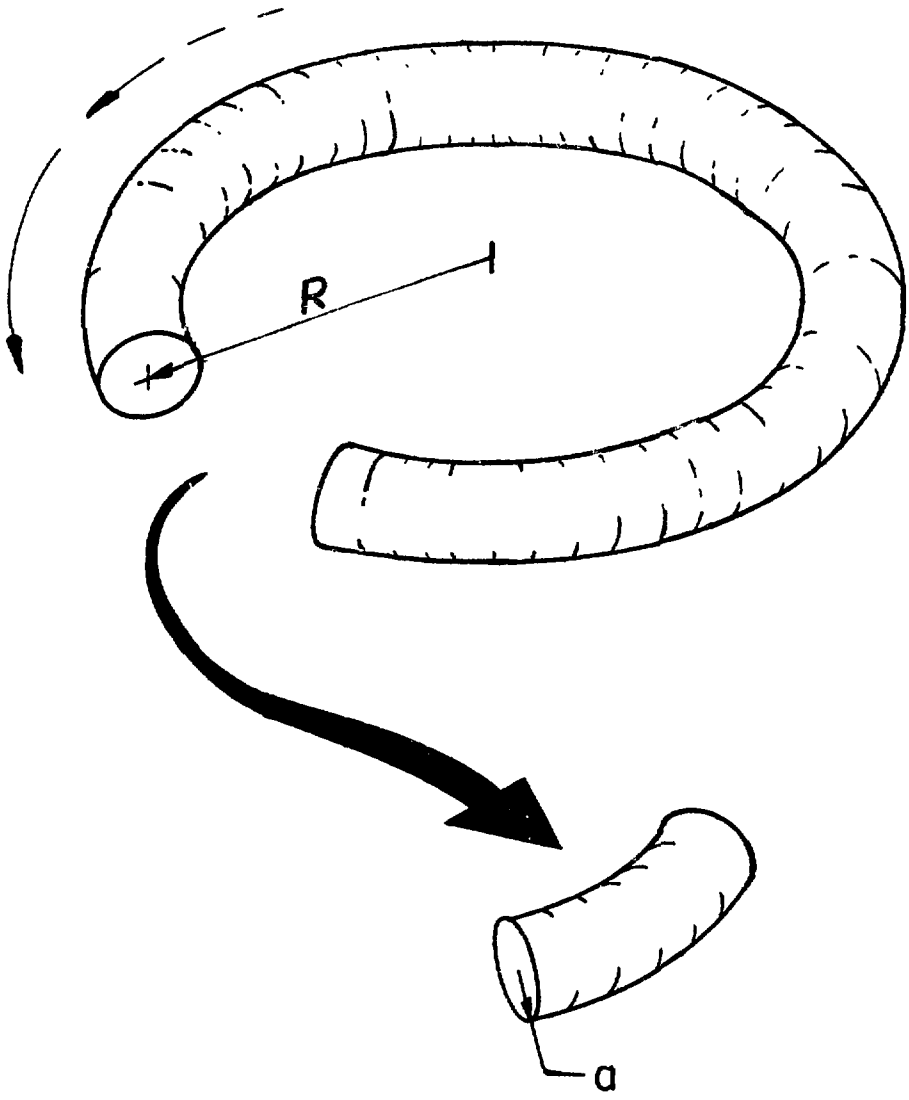

FIGURE 16

C. RING FORMATION

1. The Collapse of a Uniform Cloud

An initial density of 1.38×10^{-18} is distributed uniformly over the calculational grid. The total mass in the system is 1.81 solar masses. The entropy variable, A, is assigned the value of 1.5×10^{20}. The azimuthal velocity is initially that of a solid body rotating with an angular velocity of 6.0×10^{-13}. The radial and axial velocities are initialized to zero. For these assumed initial conditions the cloud satisfies the Jeans criterion and begins to collapse under its own self-gravity.

Figures 17 - 22 summarize the early-time configuration and flow of the fluid. Although the variation is only about 20%, the r-θ plane density contours of Fig. 17a show that a toroidal buildup of mass has already begun. The lowest-density contour in that plane is greater than the initial density of the system. The net increase results from the gas in the upper regions of the cloud collapsing down toward the equatorial plane unimpeded by the action of centrifugal forces, as shown in the r-z plane contours of Fig. 17b. The toroidal structure is also evident in both the r-θ and r-z plane angular velocity contours of Fig. 19a, b. One notices that patterns of differential rotation have begun to develop. The ring itself shows the highest angular velocities, while the fluid elements near the axis of rotation and those near the lateral boundary lag behind. The gravitational potential contours in Fig. 18a, b do not visually indicate the ring configuration. In the r-θ plane the potential well is centered on the axis of rotation rather than on the ring circumference.

The velocity and momentum-density vector fields summarize the fluid motion. The accretion onto the ring is best illustrated in the rotating-frame plots shown in Fig. 21a, b. The largest radial velocities occur in the fluid outside of the region of ring formation. This velocity pattern is consistent with the axis-centered gravitational potential contours of Fig. 18a. The picture one has of the accretion process is that of gas in the upper and outer regions of the cloud falling toward a toroidal core that has begun to form at a radius where centrifugal and gravitational forces are in balance.

The r-z velocity and momentum-density vector fields of Fig. 22a, b illustrate the collapse toward the equatorial plane. The vectors higher up the z-axis have a slight positive radial component. Two independent mechanisms contribute to produce this outward motion. First, since there is less mass near the axis in the upper regions of the cloud, the radial gravitational potential gradient is small; and the centrifugal forces resulting from the assumed initial conditions can dominate. This effect increases with time as the upper regions become more and more rarefied near the axis. Second, the downward falling gas encounters a pressure gradient that accelerates the material outwards as it impacts the spherical surface of the high pressure toroidal core. As a result of these processes, the system loses mass out the lateral boundary during the early and intermediate phases of the collapse.

Figure 23a, b illustrates the configuration of the system in terms of its density contours at a time near the point of maximum compression. The toroidal structure is still evident in both the r-θ and r-z planes; but in addition, the latter shows a disc-like structure. The linear momentum developed during the collapse has caused the system to be

compressed beyond the point of equilibrium, and the elevated thermal pressures subsequently re-expand the ring. Figure 30 summarizes the oscillation of the toroid about equilibrium.

The cloud configuration is illustrated at late time in Figs. 24 - 29. In the density contours of Fig. 24a, b, a well-defined toroidal structure is present. The minimum density contour in the r-θ plane is now about 24% of the maximum value in the ring. The density gradient is greater on the outer edge of the ring than it is on the inner edge. In fact, it is difficult to define an inner edge. Near the axis the density is 85% of the maximum. This system is a disc with a toroidal bulge. The maximum density at this time is reduced from the value at maximum compression; and the ring is less flattened into the equatorial plane, as shown in Fig. 24b. In Fig. 25a, b, one observes that even at late time the gravitational potential well of a toroidally bulging disc is centered on the axis of rotation, rather than on the ring itself.

The differential rotation is shown in the angular velocity contours of Fig. 26a, b. The ring structure is no longer visible in this variable. The average angular velocity of the late-time system is greater than that assumed for the initial cloud. As the protostar has become more concentrated the conservation of angular momentum has worked to spin it faster. The angular velocity decreases away from the axis of rotation. The sharp gradient in the axial direction shown in the r-z plane of Fig. 26b is due to the numerical technique of zeroing the velocities in very low density regions.

The vector fields are summarized in Figs. 27 - 29. In the r-θ plane, the laboratory velocity and momentum-density vector fields are

shown in Fig. 27a, b. The positive radial component indicates that the system is still losing mass. The momentum density representation reflects the concentration of mass in the toroidal system. In the rotating frame of Fig. 28a, b, the vector fields emphasize the mass loss in the outer regions. In Fig. 29a the r-z plane velocity vector field shows the high residual collapse velocities in the less dense regions of the protosta· The accompanying momentum density representation indicates a small positive radial flow in the equatorial plane.

Figure 30 is a plot of the maximum interpolated density and of the radius of that density as functions of time. The maximum ring density is oscillating about an average value of 6×10^{-18}. One would estimate the average toroidal radius to be about 2.9×10^{16}. The characteristic cross-sectional radius of this ring as measured from the graphs is 4.11×10^{16}. At this time the system has lost 31% of the mass in the original cloud.

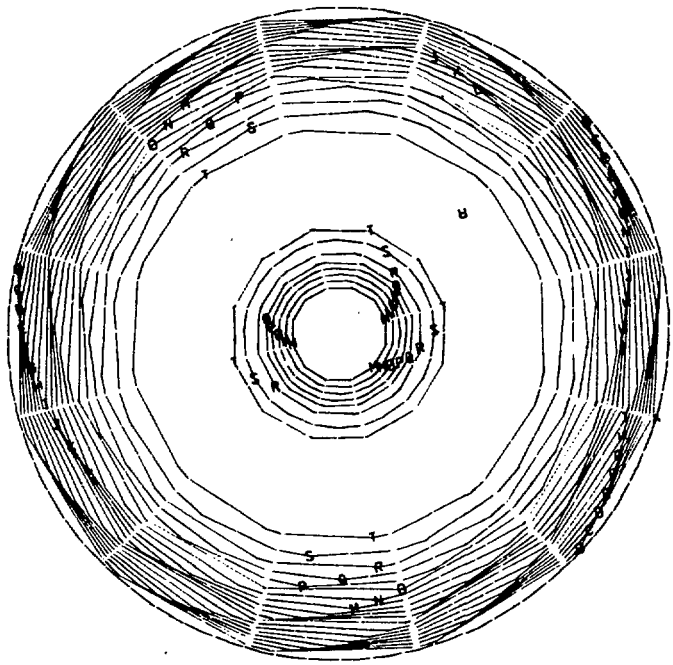

IDENTIFICATION	CONTOUR VALUE
A A A A	1.428E-18
B B B B	1.446E-18
C C C C	1.463E-18
D D D D	1.481E-18
E E E E	1.499E-18
F F F F	1.517E-18
G G G G	1.534E-18
H H H H	1.552E-18
I I I I	1.570E-18
J J J J	1.588E-18
K K K K	1.606E-18
L L L L	1.623E-18
M M M M	1.641E-18
N N N N	1.659E-18
O O O O	1.677E-18
P P P P	1.695E-18
Q Q Q Q	1.712E-18
R R R R	1.730E-18
S S S S	1.748E-18
T T T T	1.766E-18
U U U U	1.783E-18

r-θ Plane
a

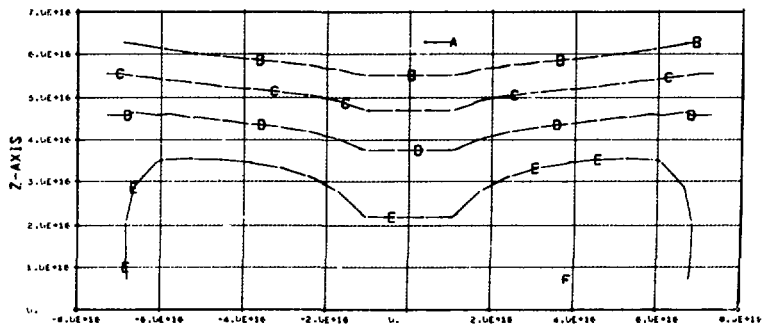

IDENTIFICATION	CONTOUR VALUE
A A A A	6.194E-19
B B B B	8.522E-19
C C C C	1.085E-18
D D D D	1.318E-18
E E E E	1.551E-18
F F F F	1.783E-18

r-z Plane
b

$t = 0.32 \times 10^5$ yrs
Density(g/cm^3)
FIGURE 17

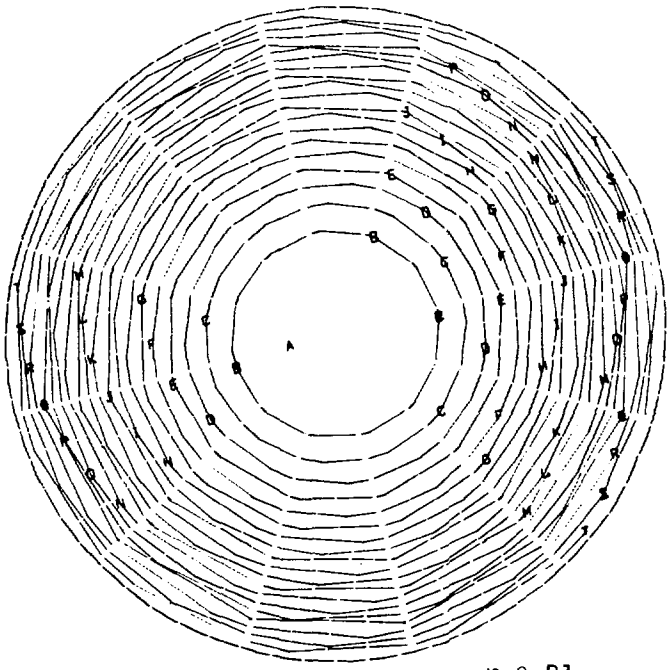

IDENTIFICATION	CONTOUR VALUE
A A A A	-4.250E+09
B B B B	-4.195E+09
C C C C	-4.139E+09
D D D D	-4.084E+09
E E E E	-4.029E+09
F F F F	-3.973E+09
G G G G	-3.918E+09
H H H H	-3.863E+09
I I I I	-3.807E+09
J J J J	-3.752E+09
K K K K	-3.697E+09
L L L L	-3.641E+09
M M M M	-3.586E+09
N N N N	-3.531E+09
O O O O	-3.476E+09
P P P P	-3.420E+09
Q Q Q Q	-3.364E+09
R R R R	-3.309E+09
S S S S	-3.254E+09
T T T T	-3.198E+09
U U U U	-3.143E+09

r-θ Plane
a

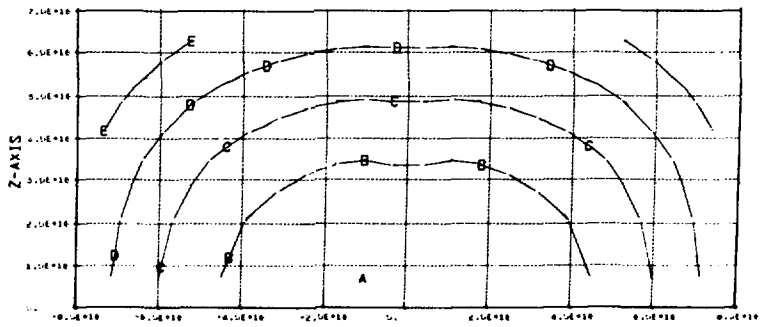

IDENTIFICATION	CONTOUR VALUE
A A A A	-4.250E+09
B B B B	-3.902E+09
C C C C	-3.554E+09
D D D D	-3.206E+09
E E E E	-2.858E+09
F F F F	-2.510E+09

r-z Plane
b

$t = 0.32 \times 10^5$ yrs
Gravitational Potential(ergs/g)
FIGURE 18

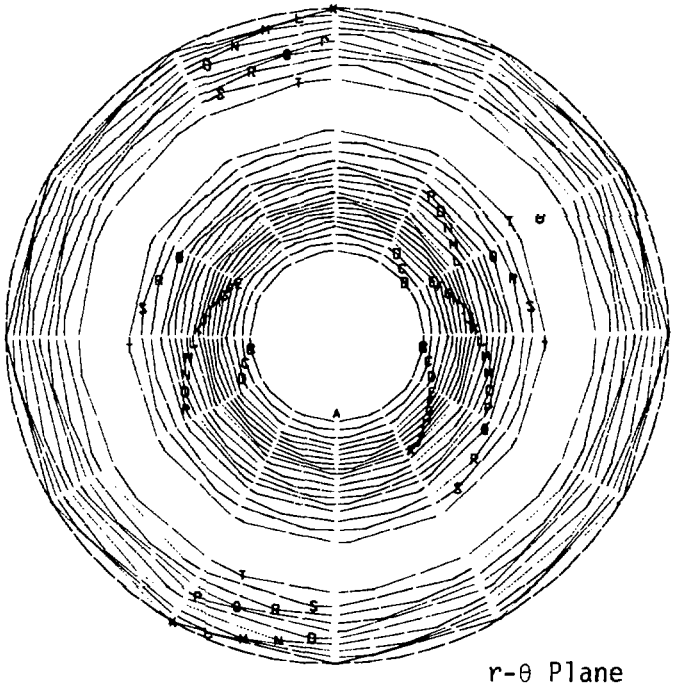

IDENTIFICATION	CONTOUR VALUE
A—A—A—A	5.865E-13
B—B—B—B	5.880E-13
C—C—C—C	5.895E-13
D—D—D—D	5.910E-13
E—E—E—E	5.925E-13
F—F—F—F	5.939E-13
G—G—G—G	5.954E-13
H—H—H—H	5.969E-13
I—I—I—I	5.984E-13
J—J—J—J	5.998E-13
K—K—K—K	6.013E-13
L—L—L—L	6.028E-13
M—M—M—M	6.043E-13
N—N—N—N	6.057E-13
O—O—O—O	6.072E-13
P—P—P—P	6.087E-13
Q—Q—Q—Q	6.102E-13
R—R—R—R	6.117E-13
S—S—S—S	6.131E-13
T—T—T—T	6.146E-13
U—U—U—U	6.161E-13

r-θ Plane
a

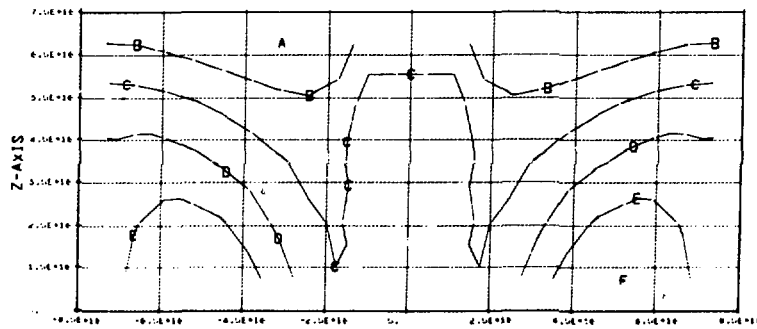

IDENTIFICATION	CONTOUR VALUE
A—A—A—A	5.664E-13
B—B—B—B	5.764E-13
C—C—C—C	5.863E-13
D—D—D—D	5.962E-13
E—E—E—E	6.062E-13
F—F—F—F	6.161E-13

r-z Plane
b

$t = 0.32 \times 10^5$ yrs
Angular Velocity(s^{-1})
FIGURE 19

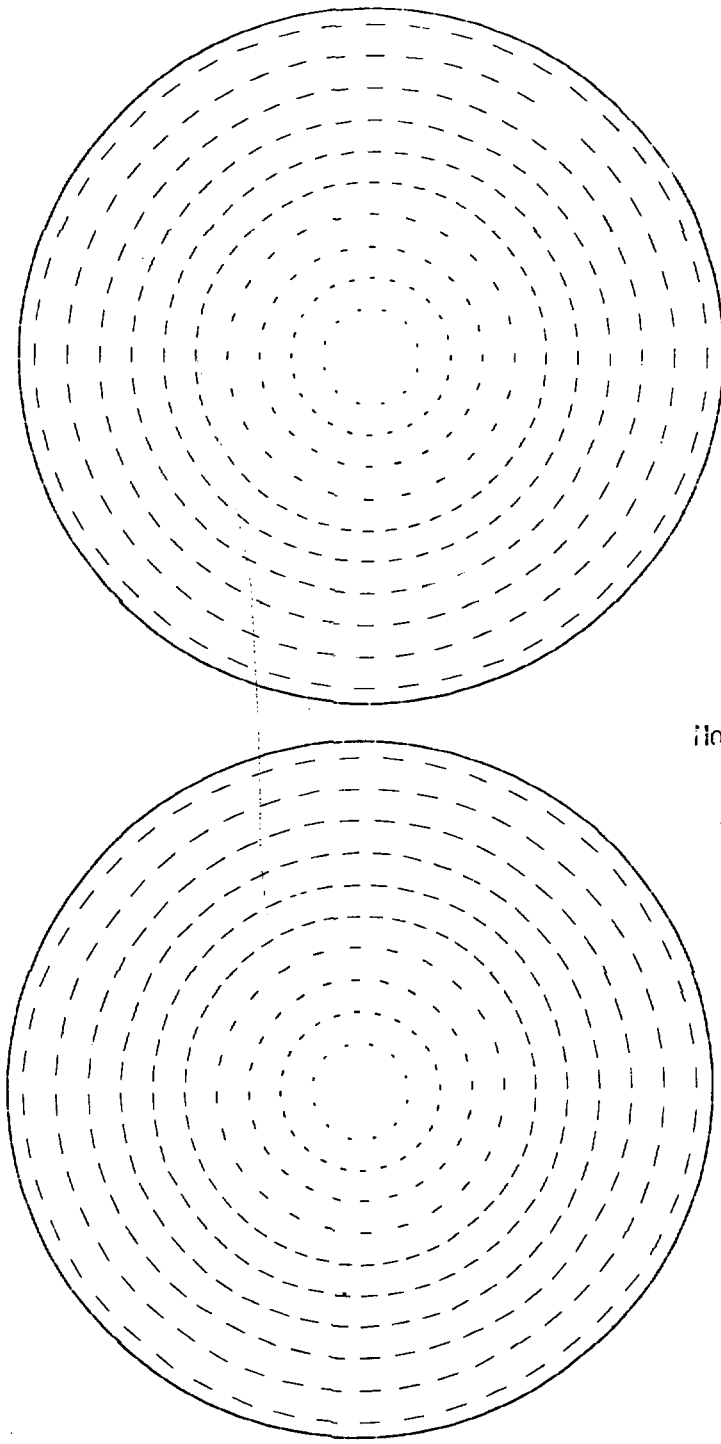

a
Velocity(cm/s)

$u_{min} = -1.83 \times 10^{3}$

$v_{max} = 4.42 \times 10^{4}$

b
Momentum Density($g/cm^2 s$)

$(\rho u)_{min} = -3.06 \times 10^{-15}$

$(\rho v)_{max} = 6.38 \times 10^{-14}$

$t = 0.32 \times 10^{5}$ yrs
Laboratory Frame
FIGURE 20

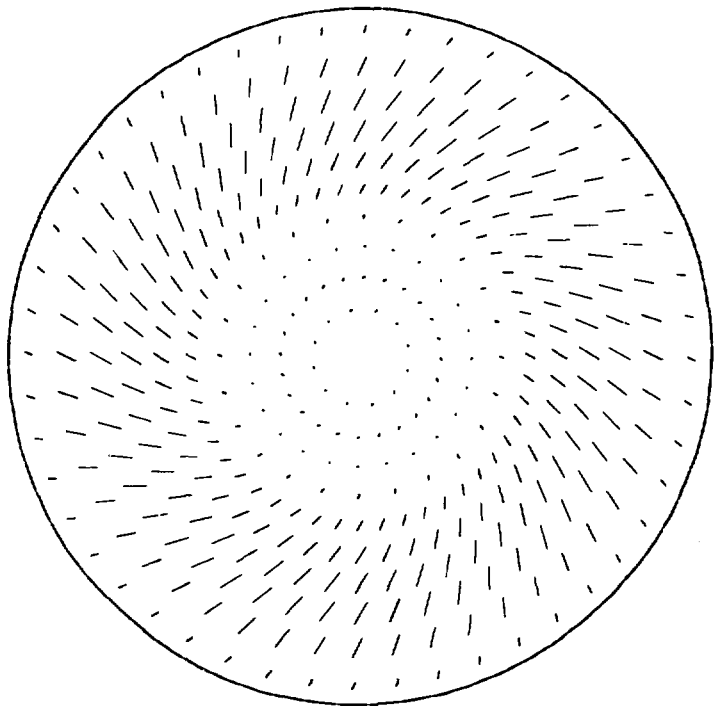

a
Velocity(cm/s)

$u_{min} = -1.83 \times 10^{3}$

$v_{max} = 9.76 \times 10^{2}$

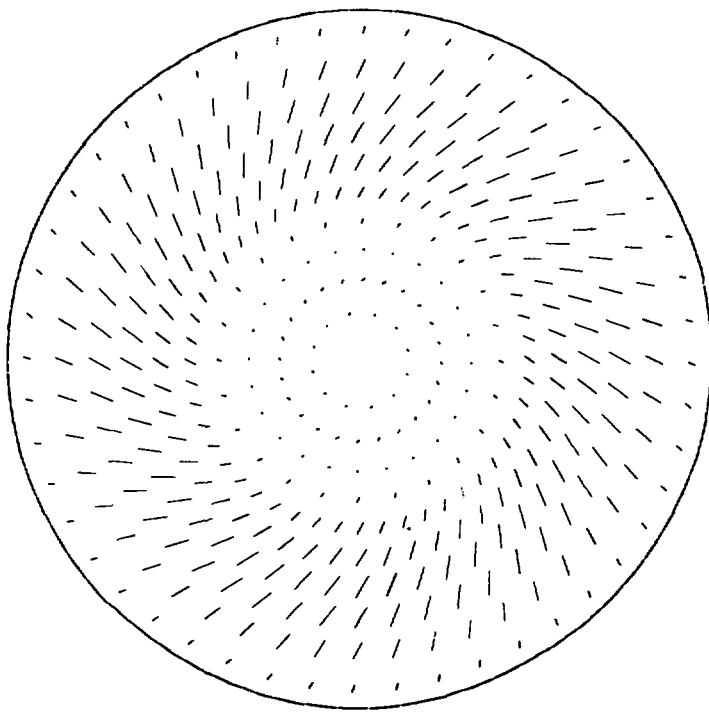

b
Momentum Density($g/cm^2 s$)

$(\rho u)_{min} = -3.06 \times 10^{-15}$

$(\rho v)_{max} = 1.69 \times 10^{-15}$

$t = 0.32 \times 10^{5}$ yrs
Rotating Frame
FIGURE 21

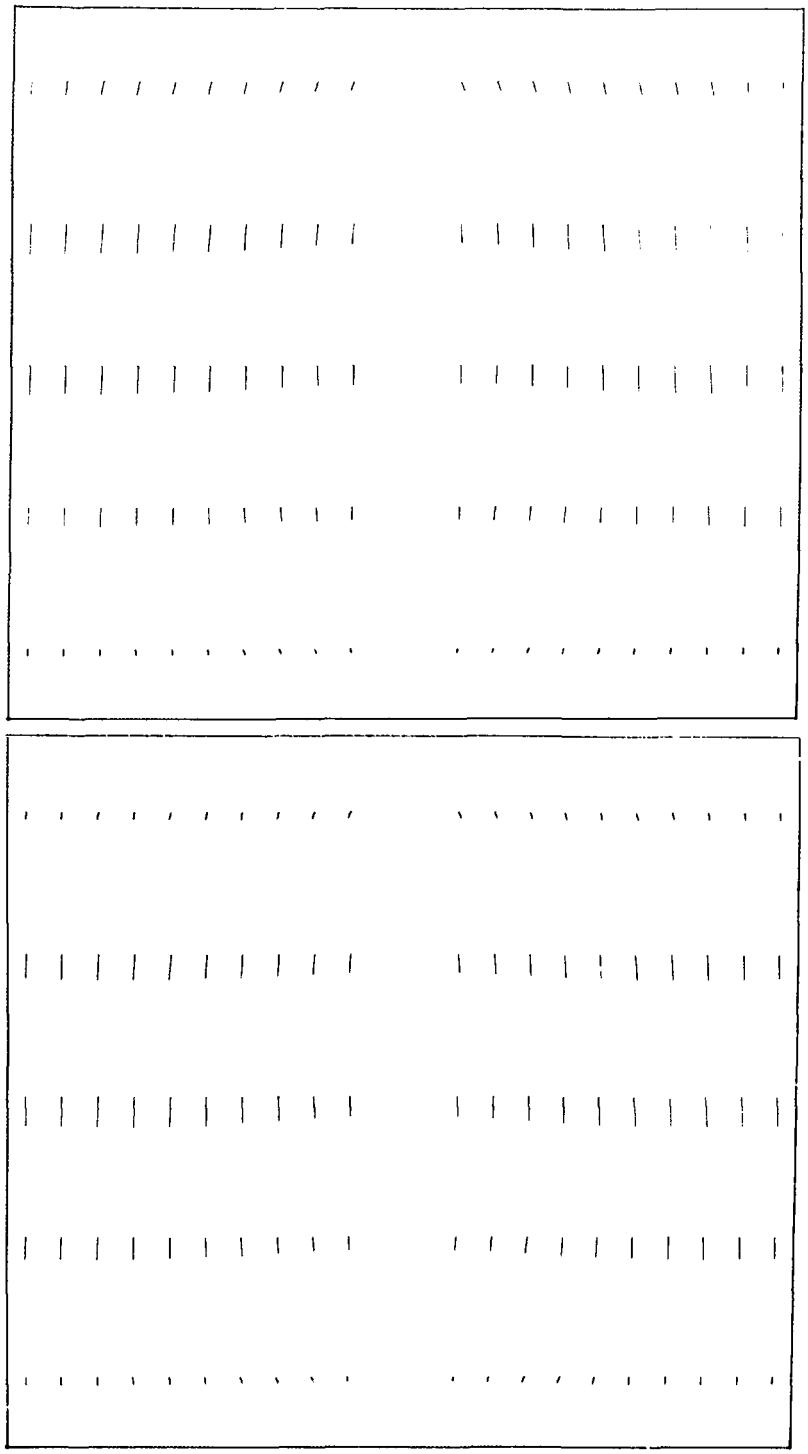

a
Velocity(cm/s)

$u_{max} = 3.60 \times 10^{3}$

$w_{min} = -1.62 \times 10^{4}$

b
Momentum Density
(g/cm^2s)

$(\rho u)_{max} = 3.15 \times 10^{-15}$

$(\rho w)_{min} = -2.19 \times 10^{-14}$

$t = 0.32 \times 10^{5}$ yrs

FIGURE. 22

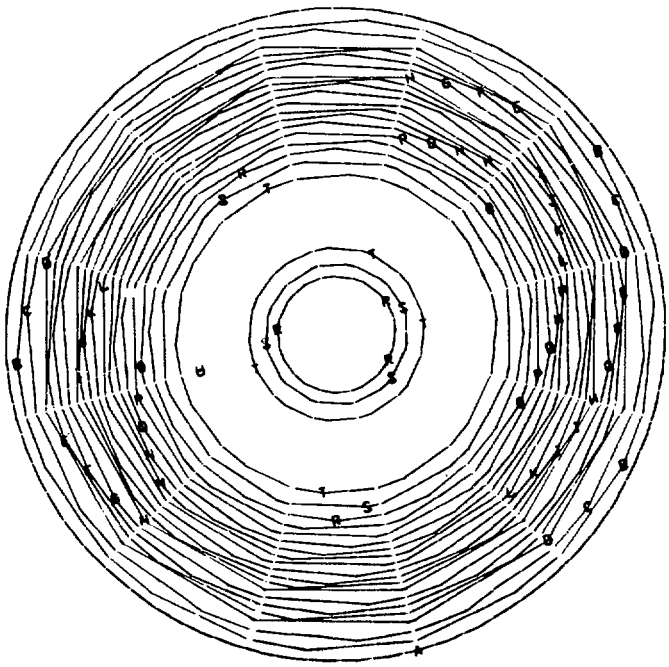

IDENTIFICATION	CONTOUR VALUE
A—A—A—A	2.024E-18
B—B—B—B	2.418E-18
C—C—C—C	2.813E-18
D—D—D—D	3.208E-18
E—E—E—E	3.602E-18
F—F—F—F	3.997E-18
G—G—G—G	4.392E-18
H—H—H—H	4.786E-18
I—I—I—I	5.181E-18
J—J—J—J	5.576E-18
K—K—K—K	5.971E-18
L—L—L—L	6.365E-18
M—M—M—M	6.760E-18
N—N—N—N	7.155E-18
O—O—O—O	7.549E-18
P—P—P—P	7.944E-18
Q—Q—Q—Q	8.339E-18
R—R—R—R	8.733E-18
S—S—S—S	9.128E-18
T—T—T—T	9.523E-18
U—U—U—U	9.918E-18

r-θ Plane
a

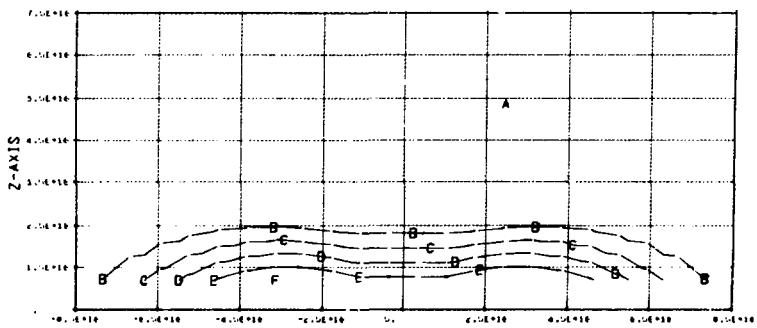

IDENTIFICATION	CONTOUR VALUE
A—A—A—A	3 650E-22
B—B—B—B	1.984E-18
C—C—C—C	3.967E-18
D—D—D—D	5.951E-18
E—E—E—E	7.934E-18
F—F—F—F	9.918E-18

r-z Plane
b

$t = 1.57 \times 10^5$ yrs
Density(g/cm^3)
FIGURE 23

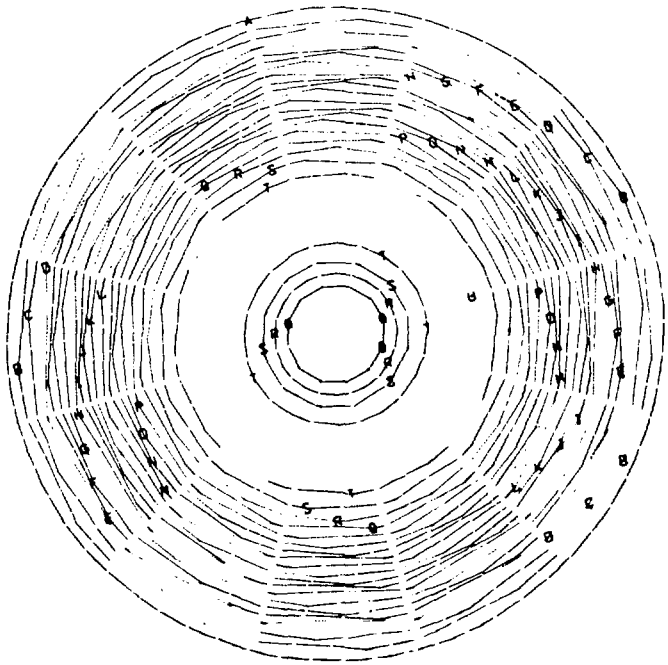

IDENTIFICATION	CONTOUR VALUE
A A A A	1.365E-18
B B B B	1.579E-18
C C C C	1.793E-18
D D D D	2.007E-18
E E E E	2.221E-18
F F F F	2.435E-18
G G G G	2.649E-18
H H H H	2.863E-18
I I I I	3.077E-18
J J J J	3.291E-18
K K K K	3.504E-18
L L L L	3.718E-18
M M M M	3.932E-18
N N N N	4.146E-18
O O O O	4.360E-18
P P P P	4.574E-18
Q Q Q Q	4.788E-18
R R R R	5.002E-18
S S S S	5.216E-18
T T T T	5.430E-18
U U U U	5.644E-18

r-θ Plane
a

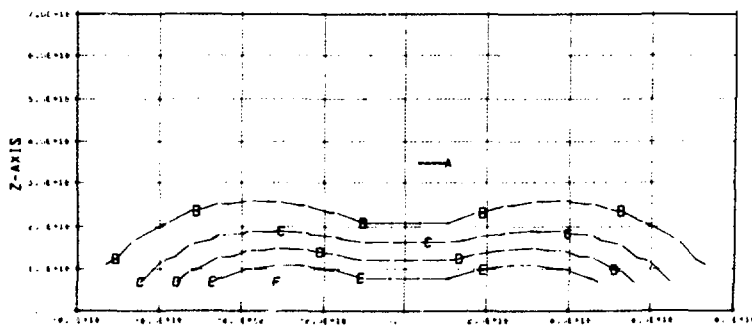

IDENTIFICATION	CONTOUR VALUE
A A A A	8.556E-28
B B B B	1.129E-18
C C C C	2.257E-18
D D D D	3.386E-18
E E E E	4.515E-18
F F F F	5.644E-18

r-z Plane
b

$t = 4.63 \times 10^5$ yrs
Density(g/cm^3)
FIGURE 24

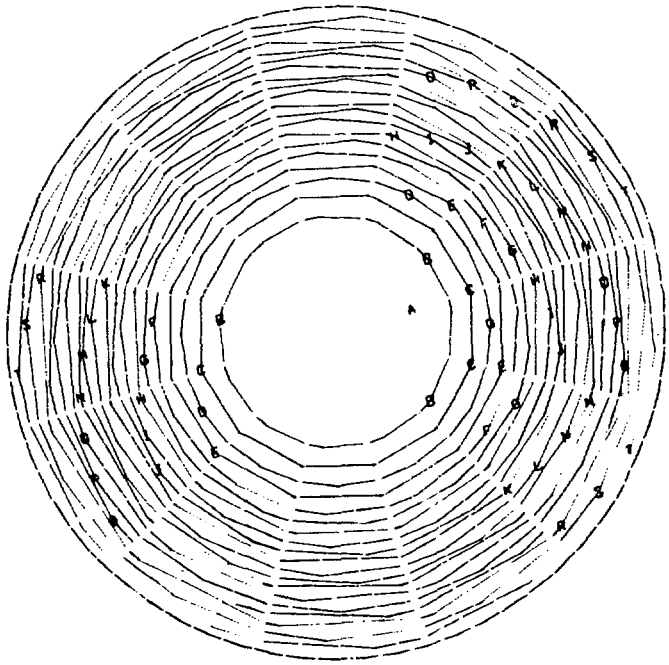

IDENTIFICATION	CONTOUR VALUE
A A A A	-4.192E+09
B B B B	-4.108E+09
C C C C	-4.024E+09
D D D D	-3.940E+09
E E E E	-3.856E+09
F F F F	-3.772E+09
G G G G	-3.687E+09
H H H H	-3.603E+09
I I I I	-3.519E+09
J J J J	-3.435E+09
K K K K	-3.351E+09
L L L L	-3.267E+09
M M M M	-3.183E+09
N N N N	-3.099E+09
O O O O	-3.015E+09
P P P P	-2.931E+09
Q Q Q Q	-2.846E+09
R R R R	-2.762E+09
S S S S	-2.678E+09
T T T T	-2.594E+09
U U U U	-2.510E+09

r-θ Plane
a

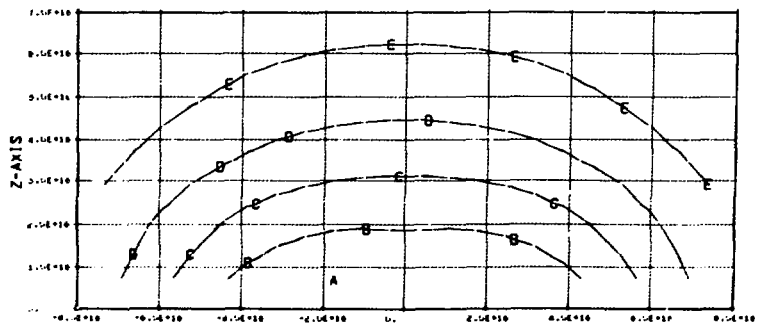

IDENTIFICATION	CONTOUR VALUE
A A A A	-4.192E+09
B B B B	-3.685E+09
C C C C	-3.178E+09
D D D D	-2.672E+09
E E E E	-2.165E+09
F F F F	-1.658E+09

r-z Plane
b

$t = 4.63 \times 10^5$ yrs
Gravitational Potential(ergs/g)
FIGURE 25

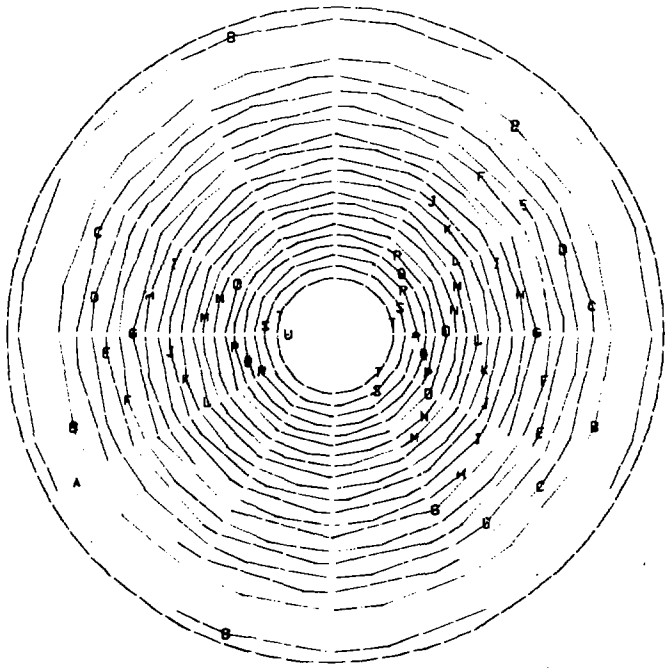

IDENTIFICATION	CONTOUR VALUE
A A A A	5.202E-13
B B B B	5.395E-13
C C C C	5.589E-13
D D D D	5.783E-13
E E E E	5.976E-13
F F F F	6.170E-13
G G G G	6.364E-13
H H H H	6.557E-13
I I I I	6.751E-13
J J J J	6.945E-13
K K K K	7.139E-13
L L L L	7.332E-13
M M M M	7.526E-13
N N N N	7.720E-13
O O O O	7.913E-13
P P P P	8.107E-13
Q Q Q Q	8.301E-13
R R R R	8.494E-13
S S S S	8.688E-13
T T T T	8.882E-13
U U U U	9.075E-13

r-θ Plane
a

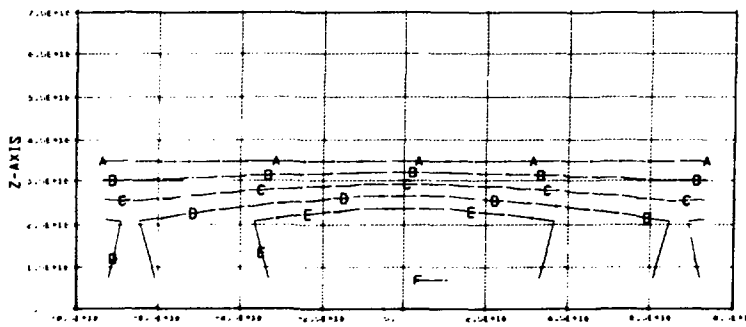

IDENTIFICATION	CONTOUR VALUE
A A A A	0.
B B B B	1.815E-13
C C C C	3.630E-13
D D D D	5.445E-13
E E E E	7.260E-13
F F F F	9.075E-13

r-z Plane
b

$t = 4.63 \times 10^5$ yrs
Angular Velocity(s^{-1})
FIGURE 26.

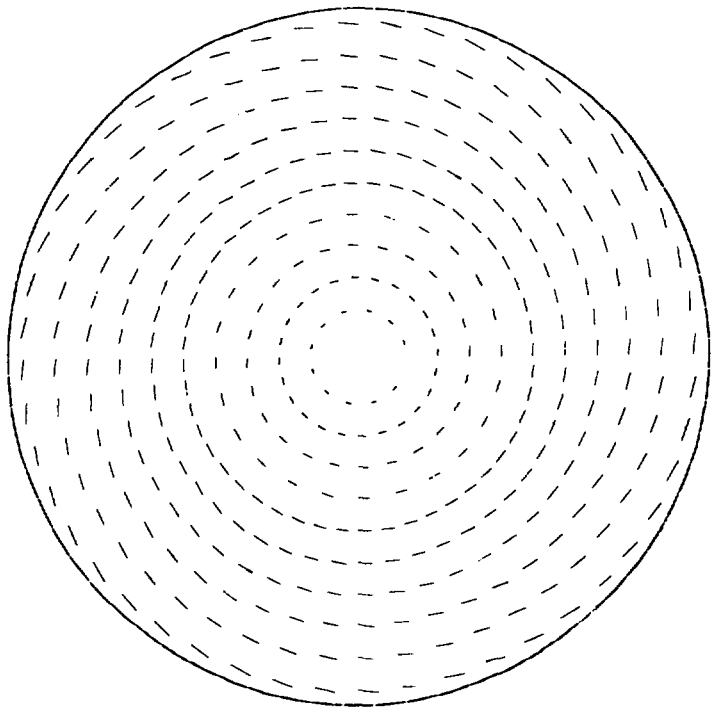

a
Velocity(cm/s)

$u_{max} = 4.79 \times 10^{3}$

$v_{max} = 4.04 \times 10^{4}$

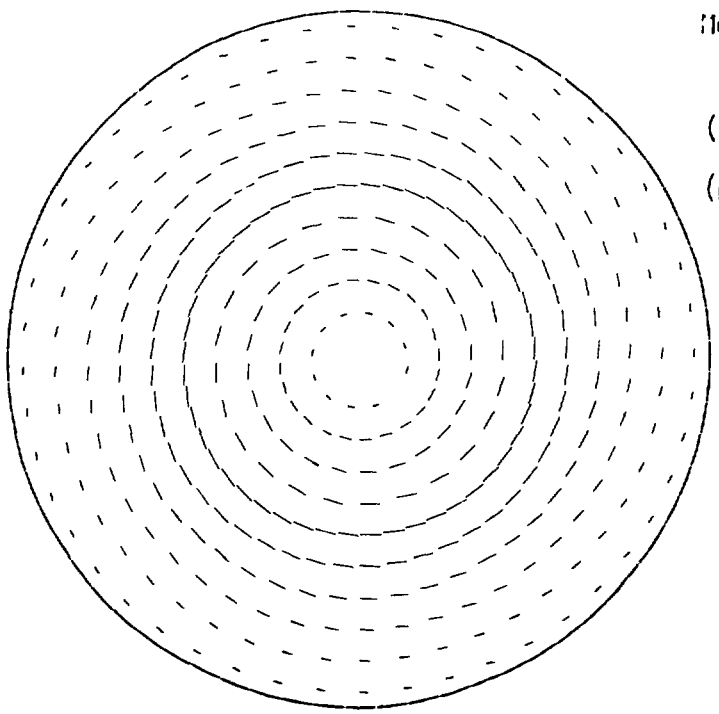

b
Momentum Density(g/cm^2s)

$(\rho u)_{max} = 8.79 \times 10^{-15}$

$(\rho v)_{max} = 1.40 \times 10^{-13}$

$t = 4.63 \times 10^{5}$ yrs
Laboratory Frame
FIGURE 27

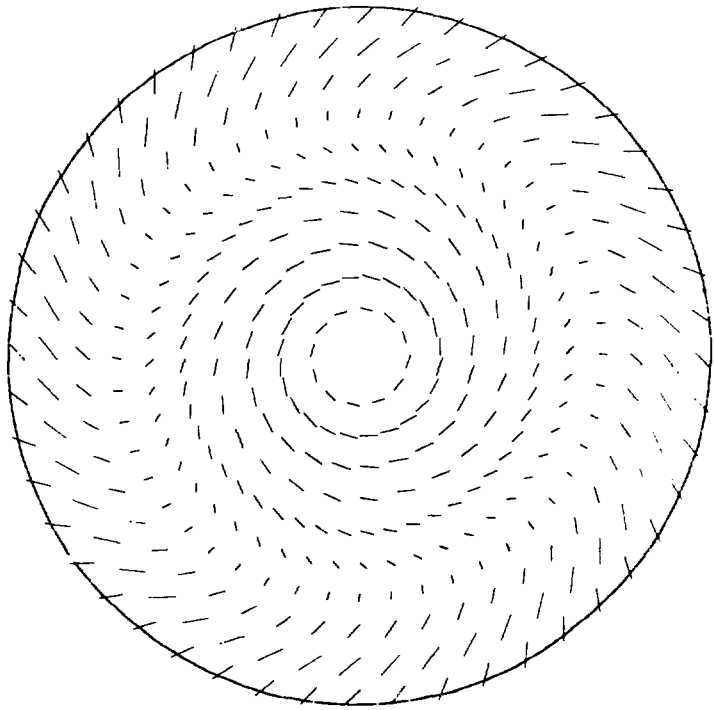

a
Velocity(cm/s)

$u_{max} = 4.79 \times 10^{3}$

$v_{min} = -5.15 \times 10^{3}$

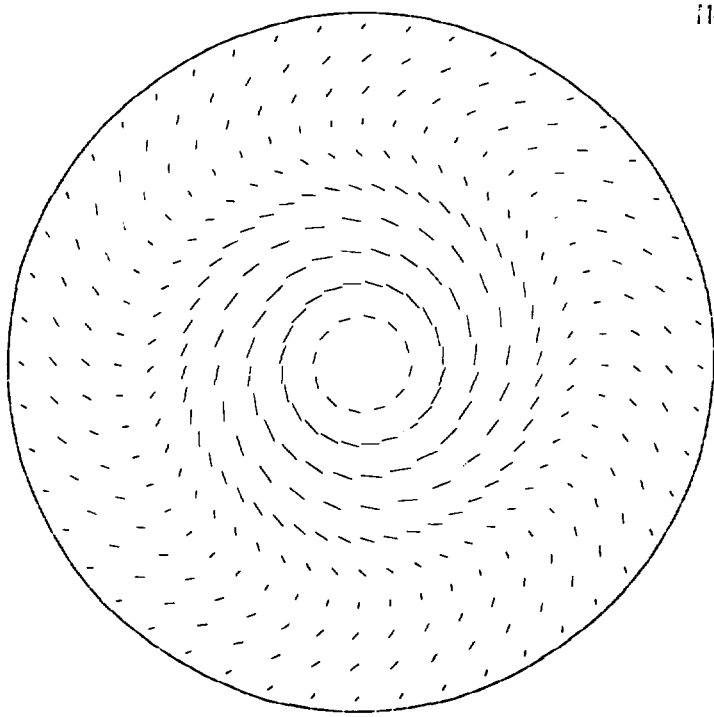

b
Momentum Density($g/cm^2 s$)

$(\rho u)_{max} = 8.79 \times 10^{-15}$

$(\rho v)_{max} = 2.71 \times 10^{-14}$

$t = 4.63 \times 10^{5}$ yrs
Rotating Frame
FIGURE 28

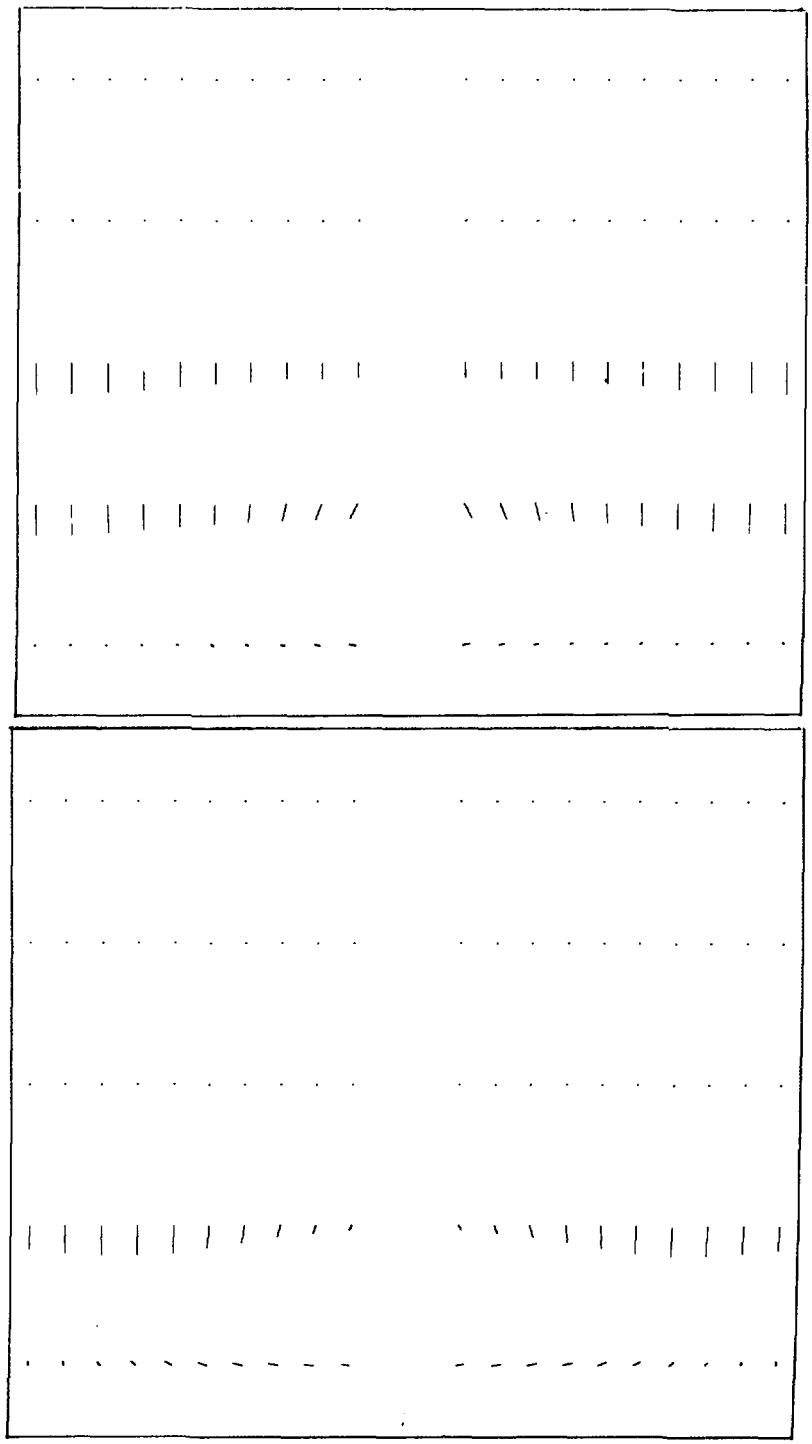

a
Velocity(cm/s)

$u_{max} = 4.79 \times 10^{3}$

$w_{min} = -9.90 \times 10^{3}$

b
Momentum Density
(g/cm^2s)

$(\rho u)_{max} = 8.79 \times 10^{-15}$

$(\rho w)_{min} = -1.39 \times 10^{-14}$

$t = 4.63 \times 10^{5}$ yrs

FIGURE 29

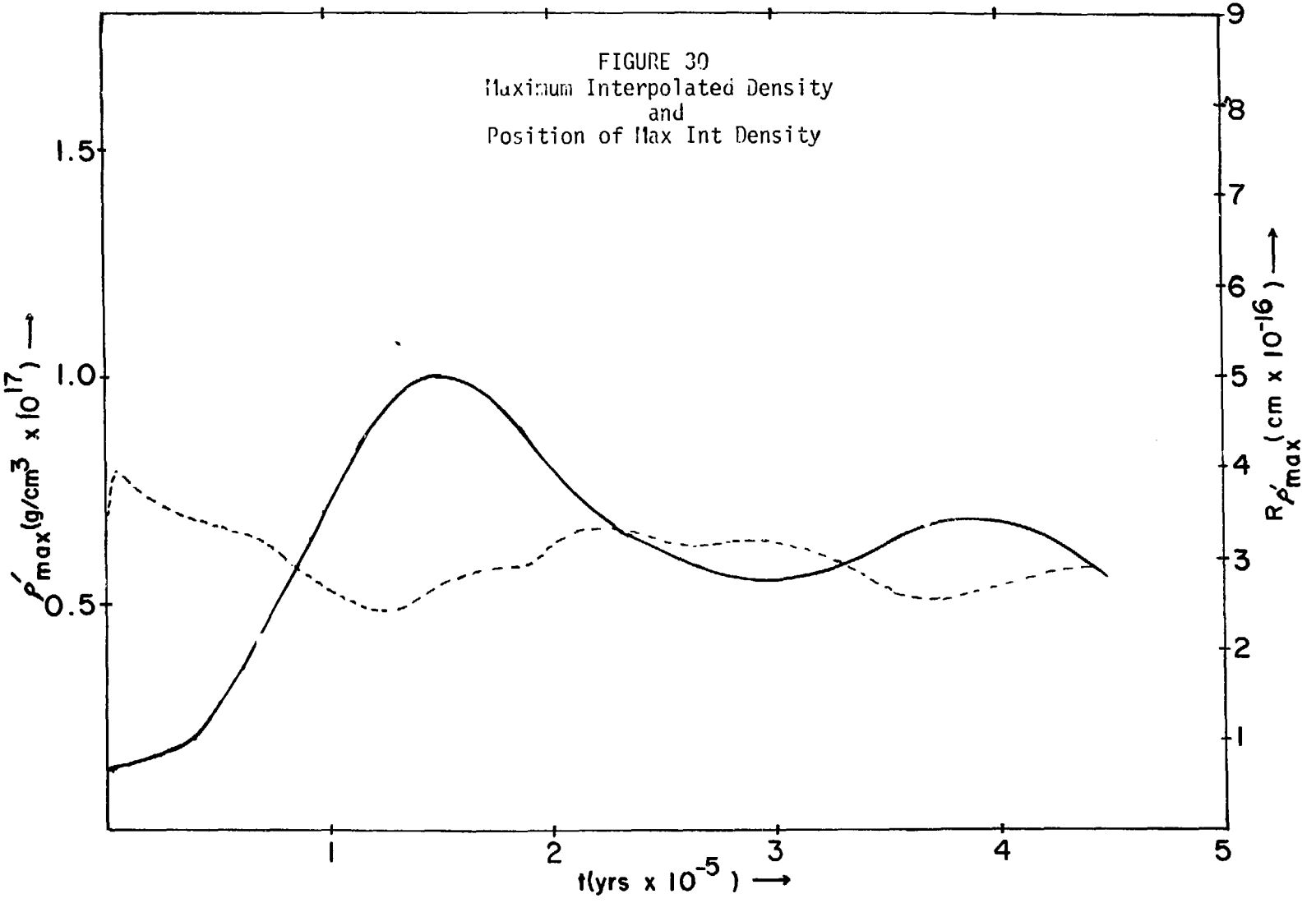

FIGURE 30
Maximum Interpolated Density
and
Position of Max Int Density

2. The Collapse of Nonuniform Clouds

a. Initial conditions

Two collapses have been followed that start from a nonuniform cloud. One system is identical to the dispersed uniform cloud discussed in the preceeding section, except for the perturbation applied initially to its azimuthal velocity field. The following prescription defines the mode 2 perturbation applied.

$$v \rightarrow v_0 \left[1 + B \sin (2\theta) \right] \qquad \text{(V-6)}$$

B is the amplitude of the perturbation; and for all cases described in this work, it has a value of 1/100. The perturbation is applied only at t = 0. The second system is an intermediate cloud having an A of 9.0×10^{19}, but is otherwise identical.

b. Dispersed cloud

The collapse for the dispersed cloud is summarized in the r-θ plane density and angular velocity contours of Figs. 31 and 32, respectively. The perturbation, evident in both density and angular velocity contours at early times, decays as the system evolves. No significant visible expression of the original asymmetry remains in the late time density contours of Fig. 31b. The angular velocity contours in Fig. 32 are slightly elliptical, indicating the presence of the still decaying initial perturbation.

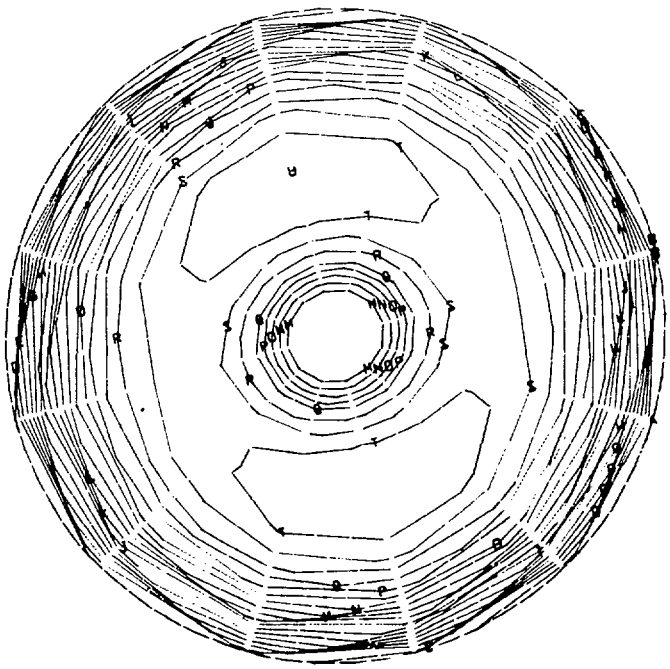

IDENTIFICATION	CONTOUR VALUE
A—A—A—A	1.404E-18
B—B—B—B	1.424E-18
C—C—C—C	1.444E-18
D—D—D—D	1.464E-18
E—E—E—E	1.484E-18
F—F—F—F	1.503E-18
G—G—G—G	1.523E-18
H—H—H—H	1.543E-18
I—I—I—I	1.563E-18
J—J—J—J	1.582E-18
K—K—K—K	1.602E-18
L—L—L—L	1.622E-18
M—M—M—M	1.642E-18
N—N—N—N	1.662E-18
O—O—O—O	1.681E-18
P—P—P—P	1.701E-18
Q—Q—Q—Q	1.721E-18
R—R—R—R	1.741E-18
S—S—S—S	1.760E-18
T—T—T—T	1.780E-18
U—U—U—U	1.800E-18

$t = 0.32 \times 10^5$ yrs

a

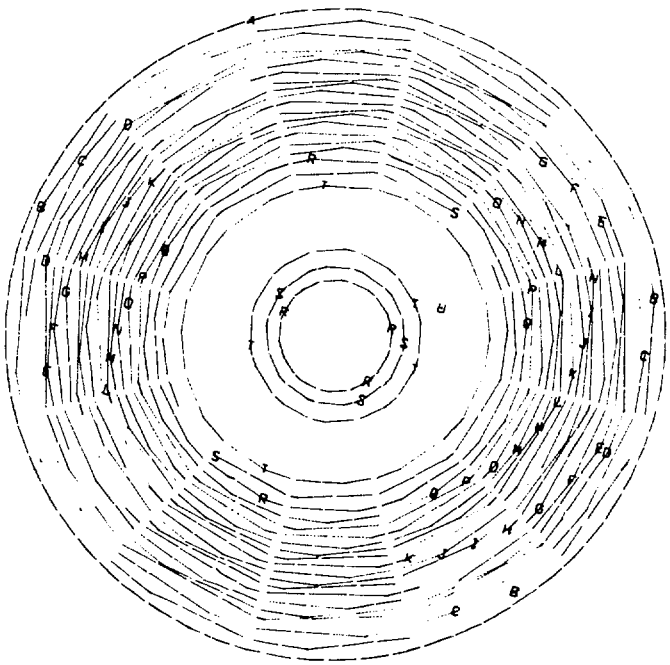

IDENTIFICATION	CONTOUR VALUE
A—A—A—A	1.264E-18
B—B—B—B	1.540E-18
C—C—C—C	1.817E-18
D—D—D—D	2.094E-18
E—E—E—E	2.371E-18
F—F—F—F	2.648E-18
G—G—G—G	2.925E-18
H—H—H—H	3.201E-18
I—I—I—I	3.478E-18
J—J—J—J	3.755E-18
K—K—K—K	4.032E-18
L—L—L—L	4.309E-18
M—M—M—M	4.586E-18
N—N—N—N	4.863E-18
O—O—O—O	5.139E-18
P—P—P—P	5.416E-18
Q—Q—Q—Q	5.693E-18
R—R—R—R	5.970E-18
S—S—S—S	6.247E-18
T—T—T—T	6.524E-18
U—U—U—U	6.800E-18

$t = 4.01 \times 10^5$ yrs

b

Density(g/cm^3)

FIGURE 31

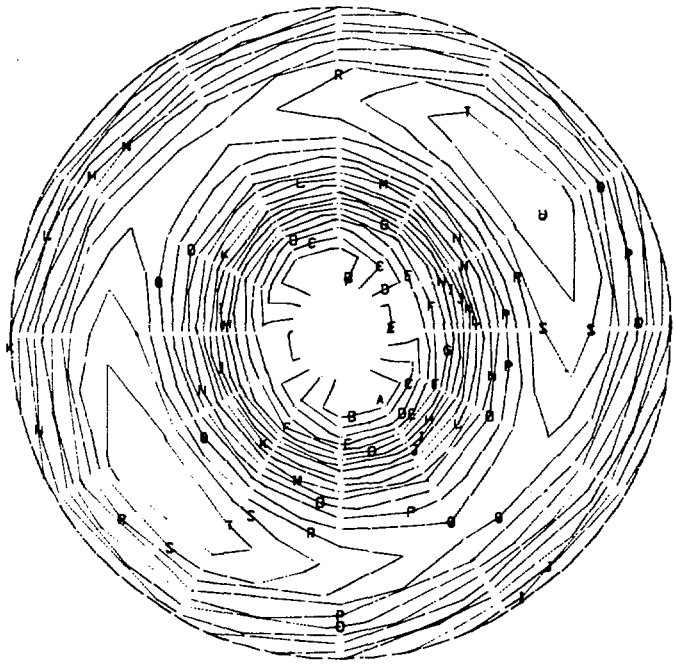

IDENTIFICATION	CONTOUR VALUE
A A A A	5.835E-13
B B B B	5.852E-13
C C C C	5.870E-13
D D D D	5.888E-13
E E E E	5.906E-13
F F F F	5.924E-13
G G G G	5.942E-13
H H H H	5.960E-13
I I I I	5.978E-13
J J J J	5.996E-13
K K K K	6.014E-13
L L L L	6.032E-13
M M M M	6.050E-13
N N N N	6.068E-13
O O O O	6.086E-13
P P P P	6.104E-13
Q Q Q Q	6.121E-13
R R R R	6.139E-13
S S S S	6.157E-13
T T T T	6.175E-13
U U U U	6.193E-13

$t = 0.32 \times 10^5$ yrs
a

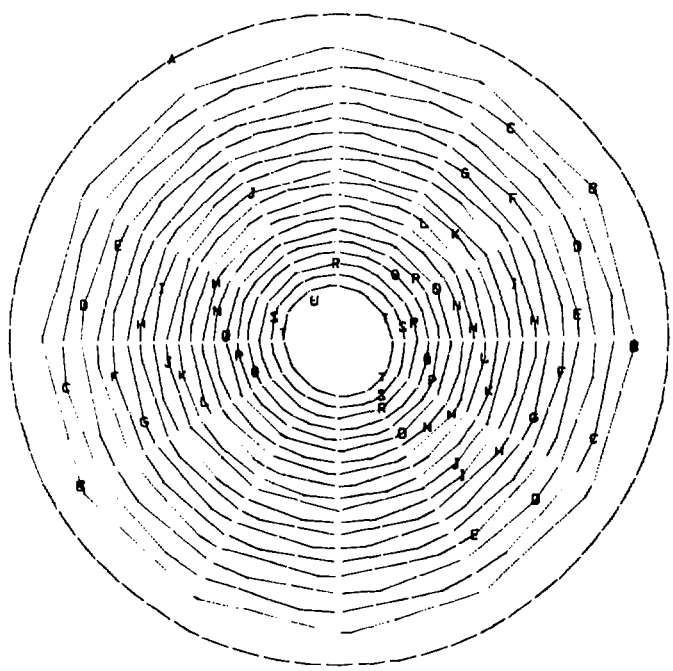

IDENTIFICATION	CONTOUR VALUE
A A A A	5.540E-13
B B B B	5.776E-13
C C C C	6.012E-13
D D D D	6.248E-13
E E E E	6.484E-13
F F F F	6.720E-13
G G G G	6.957E-13
H H H H	7.193E-13
I I I I	7.429E-13
J J J J	7.665E-13
K K K K	7.901E-13
L L L L	8.137E-13
M M M M	8.374E-13
N N N N	8.610E-13
O O O O	8.846E-13
P P P P	9.082E-13
Q Q Q Q	9.318E-13
R R R R	9.554E-13
S S S S	9.790E-13
T T T T	1.003E-12
U U U U	1.026E-12

$t = 4.01 \times 10^5$ yrs
b

Angular Velocity(s^{-1})
FIGURE 32

c. Intermediate cloud

The response of the intermediate cloud to the perturbation at very early times is virtually identical to that of the dispersed cloud described above. The late-time configuration of the intermediate cloud is presented in Figs. 33 - 37. The r-θ plane density contours shown in Fig. 33a indicate the cloud has collapsed to a binary system. The binary configuration is also reflected in the gravitational potential contours of Fig. 34a, b and in the angular velocity contours of Fig. 35a, b. The detailed interpretation of such patterns is differed to the next chapter.

The laboratory velocity vector field of Fig. 36a indicates that this system has almost ceased to lose mass. At this time the system has lost 11% of the original cloud mass. The momentum-density representation of Fig. 36b shows the extent of the bodies, as well as their orbital motion. In the velocity vector field referred to the rotating frame, one observes well-defined vortices centered at angles of approximately 97° and 277°, respectively. The vortex motion is counterclockwise. The initial perturbation favors binary component formation at 105° and 285°, respectively, as shown in Fig. 31a. The drift of the fragments to the 165° and 345° locations shown at this time induces spin in the outer envelope through the viscous coupling. Each body has a spin angular velocity equal to its orbital angular velocity, and the velocity field near the axis indicates that momentum is being transferred between the bodies by the vortices.

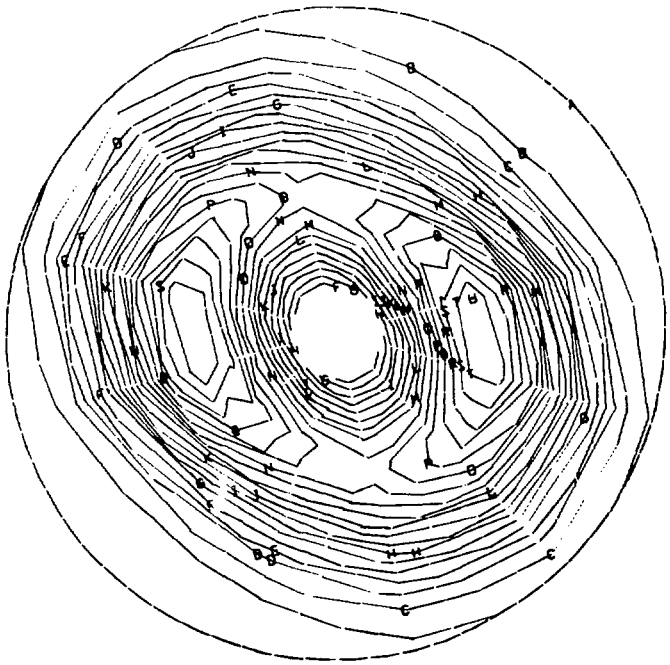

IDENTIFICATION	CONTOUR VALUE
A A A A	3.567E-19
B B B B	1.229E-18
C C C C	2.101E-18
D D D D	2.973E-18
E E E E	3.845E-18
F F F F	4.718E-18
G G G G	5.590E-18
H H H H	6.462E-18
I I I I	7.334E-18
J J J J	8.206E-18
K K K K	9.078E-18
L L L L	9.951E-18
M M M M	1.082E-17
N N N N	1.169E-17
O O O O	1.257E-17
P P P P	1.344E-17
Q Q Q Q	1.431E-17
R R R R	1.518E-17
S S S S	1.606E-17
T T T T	1.693E-17
U U U U	1.780E-17

r-θ Plane
a

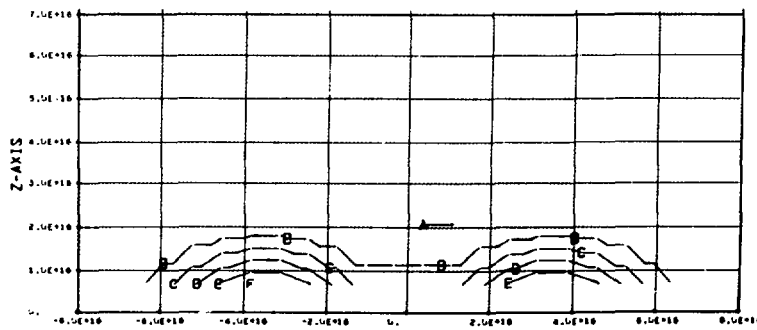

IDENTIFICATION	CONTOUR VALUE
A A A A	9.781E-25
B B B B	3.444E-18
C C C C	6.888E-18
D D D D	1.033E-17
E E E E	1.378E-17
F F F F	1.722E-17

r-z Plane
b

$t = 3.16 \times 10^5$ yrs

Density(g/cm^3)

FIGURE 33

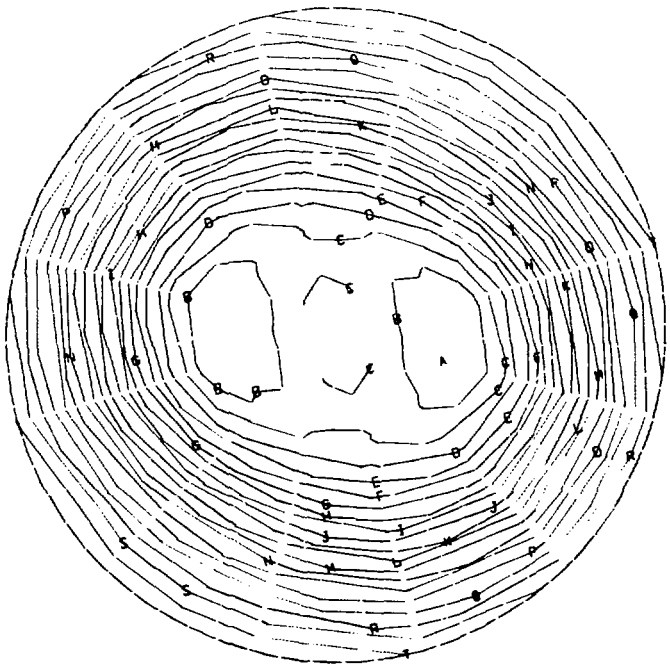

IDENTIFICATION	CONTOUR VALUE
A A A A	-6.413E+09
B B B B	-6.243E+09
C C C C	-6.072E+09
D D D D	-5.901E+09
E E E E	-5.730E+09
F F F F	-5.560E+09
G G G G	-5.389E+09
H H H H	-5.218E+09
I I I I	-5.047E+09
J J J J	-4.877E+09
K K K K	-4.706E+09
L L L L	-4.535E+09
M M M M	-4.364E+09
N N N N	-4.194E+09
O O O O	-4.023E+09
P P P P	-3.852E+09
Q Q Q Q	-3.681E+09
R R R R	-3.511E+09
S S S S	-3.340E+09
T T T T	-3.169E+09
U U U U	-2.998E+09

r-θ Plane
a

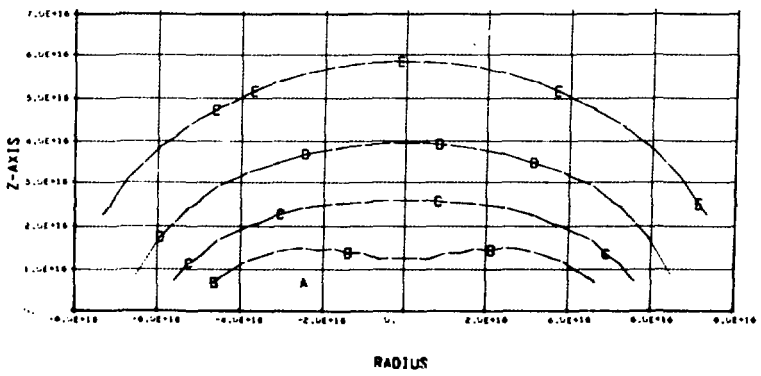

IDENTIFICATION	CONTOUR VALUE
A A A A	-6.413E+09
B B B B	-5.567E+09
C C C C	-4.721E+09
D D D D	-3.875E+09
E E E E	-3.029E+09
F F F F	-2.183E+09

r-z Plane
b

$t = 3.16 \times 10^5$ yrs
Gravitational Potential(ergs/g)
FIGURE 3c

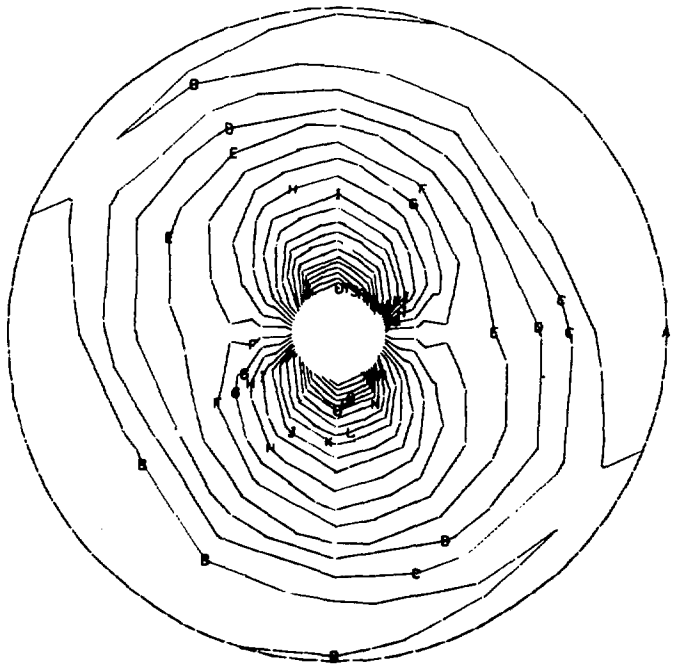

IDENTIFICATION	CONTOUR VALUE
A A A A	6.926E-13
B B B B	7.689E-13
C C C C	8.452E-13
D D D D	9.215E-13
E E E E	9.978E-13
F F F F	1.074E-12
G G G G	1.150E-12
H H H H	1.227E-12
I I I I	1.303E-12
J J J J	1.379E-12
K K K K	1.456E-12
L L L L	1.532E-12
M M M M	1.608E-12
N N N N	1.685E-12
O O O O	1.761E-12
P P P P	1.837E-12
Q Q Q Q	1.913E-12
R R R R	1.990E-12
S S S S	2.066E-12
T T T T	2.142E-12
U U U U	2.219E-12

r-θ Plane
a

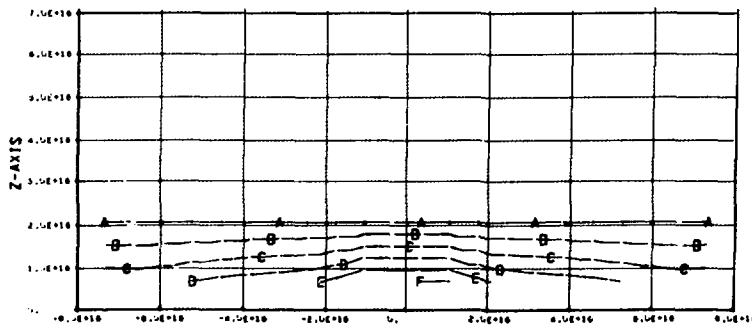

IDENTIFICATION	CONTOUR VALUE
A A A A	0.
B B B B	3.062E-13
C C C C	6.123E-13
D D D D	9.185E-13
E E E E	1.225E-12
F F F F	1.531E-12

r-z Plane
b

$t = 3.16 \times 10^5$ yrs
Angular Velocity(s^{-1})
FIGURE 35

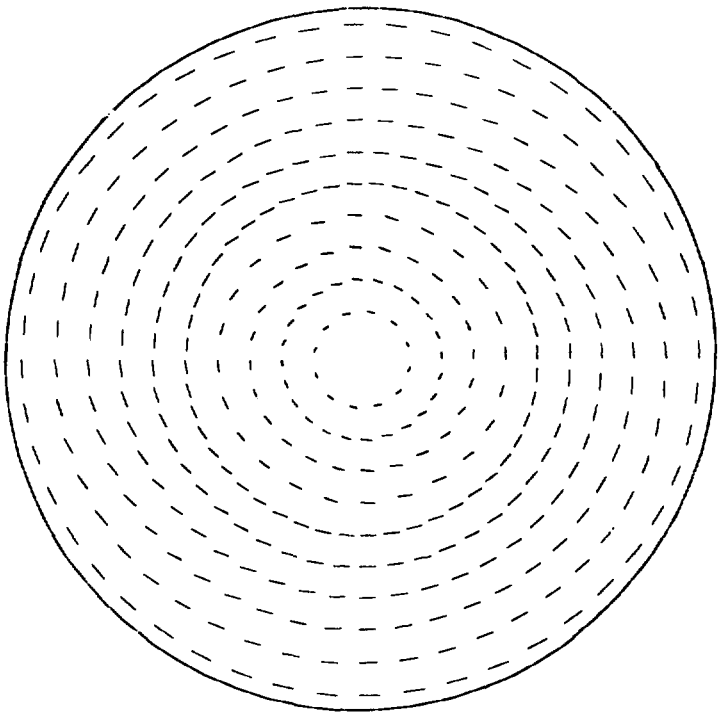

a
Velocity(cm/s)

$u_{min} = -1.38 \times 10^{4}$

$v_{max} = 5.91 \times 10^{4}$

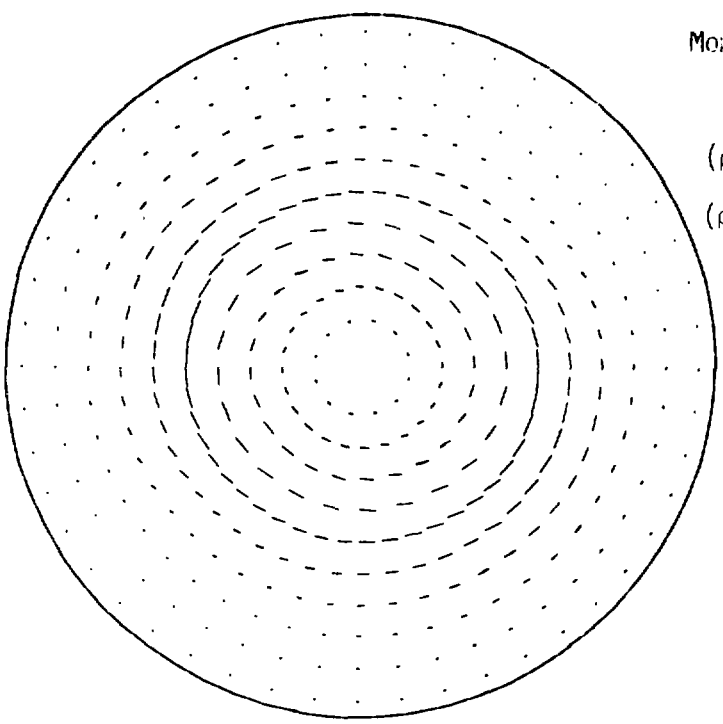

b
Momentum Density($g/cm^2 s$)

$(\rho u)_{min} = -1.11 \times 10^{-13}$

$(\rho v)_{max} = 6.68 \times 10^{-13}$

$t = 3.16 \times 10^{5}$ yrs
Laboratory Frame
FIGURE 36

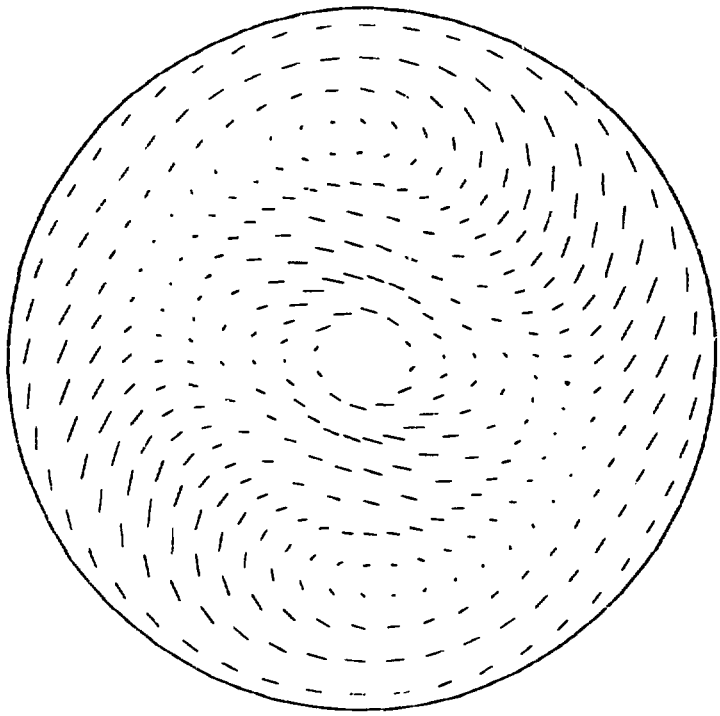

a
Velocity(cm/s)

$u_{min} = -1.38 \times 10^{4}$

$v_{min} = -1.59 \times 10^{4}$

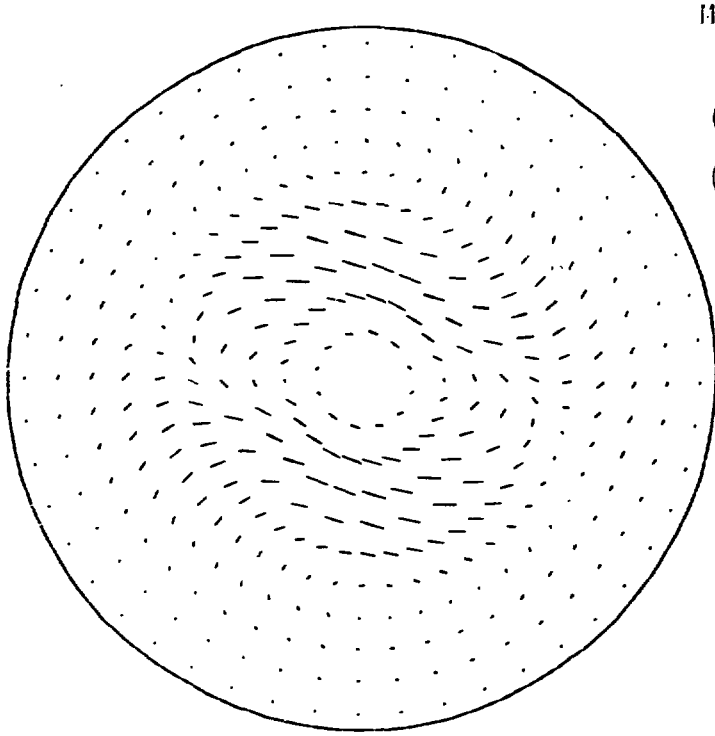

b
Momentum Density($g/cm^2 s$)

$(\rho u)_{min} = -1.11 \times 10^{-13}$

$(\rho v)_{max} = 1.48 \times 10^{-13}$

$t = 3.16 \times 10^{5}$ yrs
Rotating Frame

FIGURE 37

d. Comparison

It is apparent that a cloud must be sufficiently intermediate in order to collapse into a stable toroidal ring, but more work will be required before a precise criterion can be given for this type of collapse. Although the intermediate cloud progressed directly from a uniform-density configuration with a perturbed azimuthal velocity field to a condensed binary system without forming an intermediate toroidal stage, it is never-the-less useful to investigate the stability of toroidal systems as a means for understanding the overall stability of protostellar collapse. Indeed, this investigation is the central theme of the next chapter.

VI. NON-AXISYMMETRIC PERTURBATION OF ROTATING RINGS

A. INTRODUCTION

It has been demonstrated in Chapter V and in the publications discussed in Chapter I that under certain reasonable conditions rotating toroids may exist as an intermediate stage in protostellar evolution. It has also been demonstrated in Chapter V that initial asymmetries can either grow or decay during collapse of the cloud. In this chapter, we develop a quantitative theory of the fragmentation processes in collapsing protostars.

The prediction of protostellar cloud stability can be addressed from two different viewpoints. The most direct approach would be to perform a series of collapse calculations, in which the initial conditions and the initial perturbations are systematically varied. There are, however, serious difficulties with this direct method. If a cloud is in a nonequilibrium state, the initial conditions almost surely can not be characterized by a single dimensionless parameter; so that there are a virtually limitless number of initial conditions to be considered.

The indirect approach involves understanding the response of a set of initially unperturbed toroids to applied perturbations. These calculations are performed for six different representative examples and the dynamics of the fragmentation process are described and illustrated in detail. We develop a theoretical stability curve, which is normalized to the numerical results and allows one to predict the probable modes of fragmentation of arbitrary toroidal systems in terms of a dimensionless parameter characterizing the initial equilibrium conditions. The resulting stability diagram and its interpretation are discussed in Section G of this chapter.

In all problems discussed in this chapter the mass is initially concentrated in toroidal configurations. The initial conditions for each calculation are produced by a preliminary calculation through which a rather coarse set of prescribed conditions is allowed to relax to an equilibrium state. The initial cross section of the rings is approximated by a square region of the calculational mesh, which consists of two radial zones above the plane of symmetry. This study uses systems having three solar masses and an initial angular velocity of $2.45 \times 10^{-12}\ s^{-1}$. For such toroids the gravitational and centrifugal forces are balanced. To vary the properties of the toroids, one changes the entropy variable, A. Throughout this chapter the value of A is expressed in the cgs system of units. These units are omitted in the text for convenience. Depending on the value of A, the forces due to the thermal pressures in the toroid may or may not be in balance with the forces of self-gravity. The initial toroidal configuration is therefore allowed to expand to an equilibrium state before the application of the perturbation. If the gas expands to form a more diffuse ring with a larger cross-sectional area, the average angular velocity of the system decreases and differential rotation develops. By this means one obtains the six unique toroidal configurations that are used in the subsequent fragmentation studies and stability analyses. In all discussions below it will be these toroids that are defined as initial conditions at the time of perturbation. It should be noted that the location of the objects relative to the rotating frame can drift from that favored by the initial perturbation because the average orbital angular velocity of the system must change as the mass configuration adjusts itself during approach to steady state.

In the calculations a 10 x 12 x 5 grid is used. The 12 azimuthal zones divide the upper region into 30° segments. In an r-z plane the cell surfaces are squares 7.0×10^{15} cm on a side. The upper boundary is 3.5×10^{16} cm above the symmetry plane. The inner radial boundary required by the central core and the outer radial boundary are 7.0×10^{15} cm and 7.7×10^{16} cm, respectively, from the axis of rotation.

B. THE PERTURBATIONS

In order to develop a thorough understanding of the response of rotating toroids to non-axisymmetric perturbations, one must characterize not only the toroidal fluid system as previously described but the perturbation as well.

The binary perturbation is applied to the system through the azimuthal velocities in a manner described by the following prescription

$$v \rightarrow v_0 \left[1 + B \sin (2\theta) \right]$$

B is the amplitude of the perturbation; and for all cases described in this work, it has a value of 0.01. If the system is unstable, the asymmetry is rapidly amplified and fragmentation results; however, if the system is stable, the amplitude of the disturbance quickly decays and axial symmetry is restored.

Two higher mode perturbations have been used in developing the stability diagram described subsequently in this chapter. The mode 3 perturbation is given by

$$v \rightarrow v_0 \left[1 + B \sin (3\theta) \right]$$

The mode 6 perturbation is

$$v \rightarrow v_0 \left[1 + B \cos (6\theta) \right]$$

C. COMPACT RINGS

1. Case I

a. Initial conditions

The center of the rotating toroid used in Case I is located 2.77×10^{16} cm from the axis of rotation and has a characteristic cross-sectional radius, a, of 1.0×10^{16} cm. The entropy variable, A, has a value of 5×10^{19}. This toroid is the most compact of any system studied. Other salient properties of the system are summarized in Table I. The initial conditions are graphically represented in Figs. 38 - 41. In Fig. 38a, b the compactness of the ring is evident in both the r-θ and r-z planes. The high concentration of contour lines at the inner and outer circumferences, respectively, indicates sharp density gradients between the toroid and its surroundings. In Fig. 38b one sees that the density in the second computational zone above the reflecting plane is down by a factor of 5 from that in the center of the ring. The gravitational potential well is centered on the ring itself (Fig. 39a) and is the deepest initial well of any toroid used in this study.

The angular velocity distribution in this compact ring does not differ very much from that which would occur if the system were in solid body rotation. The high concentration of contour lines on the inner and outer edges of the ring, shown in Fig. 40a, result because of a numerical technique that sets the velocities in the very low density external regions to zero.

The condition of the toroid can also be surmised from the laboratory velocity vector plots in Fig. 41a. The orbital motion is in a positive sense as one can see by lining up the tails of the vectors. All velocities are contraction velocities that imply the toroid is decreasing in cross-sectional area. In fact it is questionable that a body this compact can be accurately resolved by the calculational mesh. Nevertheless we include this very compact system because of the qualitative information that can be derived from it. The large-scale balance between centrifugal and gravitational forces is illustrated in the momentum-density plot of Fig. 41b. The momentum vectors display no net radial mass motion either toward or away from the axis of rotation.

Table I

Initial Conditions

Case I

$A(cm^4/g^{2/3}\ s^2)$	5.00×10^{19}	M(g)	5.91×10^{33}
a(cm)	1.00×10^{16}	W(ergs)	-5.00×10^{43}
$\rho'_{max}(g/cm^3)$	1.94×10^{-16}	KE(ergs)	1.71×10^{41}
$R_{\rho'_{max}}$ (cm)	2.77×10^{16}	U(ergs)	1.36×10^{43}
$\rho_{max}(g/cm^3)$	1.75×10^{-16}	T(ergs)	1.46×10^{43}
$R_{\rho_{max}}$ (cm)	2.45×10^{16}	E(ergs)	-2.15×10^{43}
t_f(yrs)	0.05×10^{5}	$J(g\ cm^2/s)$	1.19×10^{55}
$\omega(s^{-1})$	2.46×10^{-12}	Θ(°K)	18.8

b. Evolution of the system

In Figs. 42 - 50 the subsequent evolution of the fragmenting toroid is summarized. In Figs. 42a, b the density contours of the fragmenting toroid are displayed for two intermediate times. The short time scale on which the break-up occurs indicates the high degree of instability present in the initial system. The low thermal pressures can not effectively impede the fragmentation, and the initial perturbation is quickly amplified. Rapid evolution of the system can also be related to the local free-fall time estimate given by Eq. (I-1). Since collapse phenomena seem to occur in a few numbers of free-fall times and since the free-fall time for a density of this magnitude is about 0.05×10^5 yrs, it is not surprising that the toroid has fragmented into well-defined components in about 0.76×10^5 yrs. In fact, all of the calculations reported indicate that unstable toroids have come to a stage of complete fragmentation by about fifteen free-fall times.

In Fig. 42b one sees the presence of a higher mode in the density contours at a time of 0.60×10^5 yrs. Although the original perturbation is a pure mode 2, the higher mode has appeared. There are two explanations that one gives to explain the coupling to higher modes. One argument is physical; the other, numerical. First, the nonlinear nature of the equations of motion favors the excitation of a spectrum of modes. Second, the coarseness of the calculation grid can excite higher modes through the presence of truncation errors. Because of the coarseness of resolution, no particular physical significance can be placed on the appearance of the higher mode for this system; and in fact, at the still later time shown in Fig. 47a, b, the fluid has

reverted to the more dominant binary configuration. Figures 43a, b and 48a, b illustrate the corresponding evolution of the gravitational potential. At a time of 0.76×10^5 yrs the well depth of the components is almost twice that of the initial ring.

The interpretation of the angular velocity sequence for this case is less clear than for the more extended, and hence better resolved, components. In Fig. 44a, b the angular velocity of gas falling from the perturbed toroid toward the axis of rotation has increased due to the conservation of angular momentum. Regions of high angular velocity also occur behind the newly formed components as the residual gas in the toroid accelerates toward these new centers of attraction.

The laboratory velocity plots shown at intermediate times in Fig. 45a, b show the details of the velocity field during fragmentation. The velocity vectors on the leading edge (leading in the sense of positive orbital motion) of the components are shortened and turned around by the gravitational attraction of the trailing fragments. The toroidal remnant behind a component now moves in the increased force field of the new center of gravity, and the azimuthal velocities, already large due to the original orbital motion of the ring, are increased. Figure 46a, b shows the same sequence in a momentum density representation so that one can determine patterns of mass transport.

In Fig. 50a, b the late-time velocity fields relative to the laboratory and to the rotating frame, respectively, are shown. In both representations one observes a large positive radial component of velocity. The binary fragments in this system are separating. In Fig. 50b vortices are apparently developing from the complex interplay of frictional and gravitational forces in the wake of the outward moving

components. At these late times the rate and extent of separation of the bodies must be questioned because of the poor resolution of the compact components by the calculational grid. Such a situation can introduce inaccuracies in the solution of the partial differential equations, which accumulate with time.

A manifestation of the inaccuracy in the late time solution for Case I is the lack of energy conservation. The models assume that the processes in protostellar clouds proceed adiabatically. Since no energy balance equation is solved, one does not include the heating effects due to the irreversible viscous dissipation. Therefore, although the total energy should not be precisely conserved, it should be approximately a constant, especially for the collapse of the more dispersed toroids. In most of the other cases described in this chapter the energy conservation is 1 - 2%. At the last time reported in this calculation, however, the total energy of the system has increased by almost 50%.

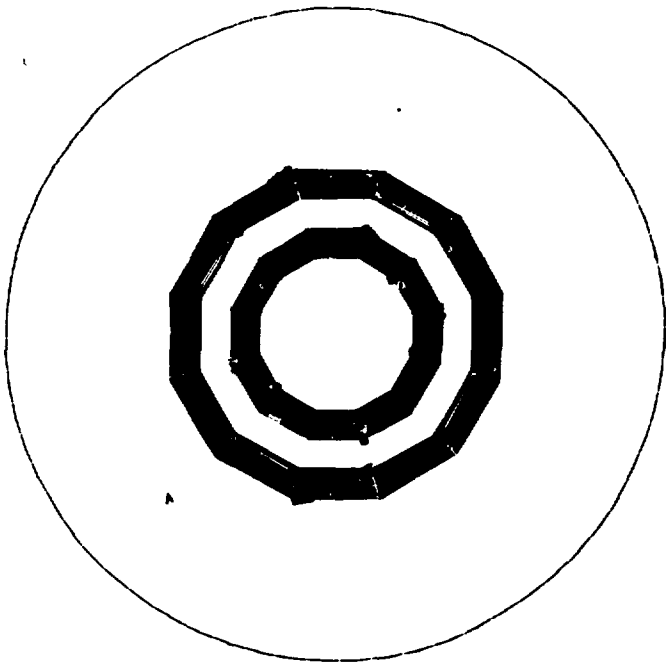

IDENTIFICATION	CONTOUR VALUE
A A A A	1.000E-26
B B B B	8.757E-18
C C C C	1.751E-17
D D D D	2.627E-17
E E E E	3.503E-17
F F F F	4.379E-17
G G G G	5.254E-17
H H H H	6.130E-17
I I I I	7.006E-17
J J J J	7.882E-17
K K K K	8.757E-17
L L L L	9.633E-17
M M M M	1.051E-16
N N N N	1.138E-16
O O O O	1.226E-16
P P P P	1.314E-16
Q Q Q Q	1.401E-16
R R R R	1.489E-16
S S S S	1.576E-16
T T T T	1.664E-16
U U U U	1.751E-16

r-θ Plane
a

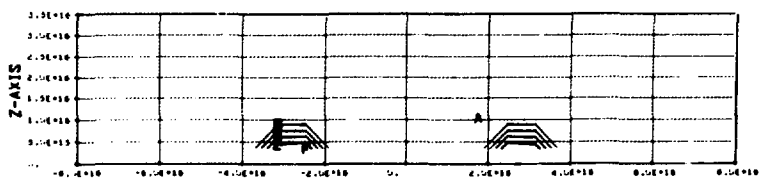

IDENTIFICATION	CONTOUR VALUE
A A A A	1.303E-27
B B B B	3.503E-17
C C C C	7.00[illegible]-17
D D D D	1.051E-16
E E E E	1.401E-16
F F F F	1.751E-16

r-z Plane
b

t = 0

Density(g/cm^3)

FIGURE 38

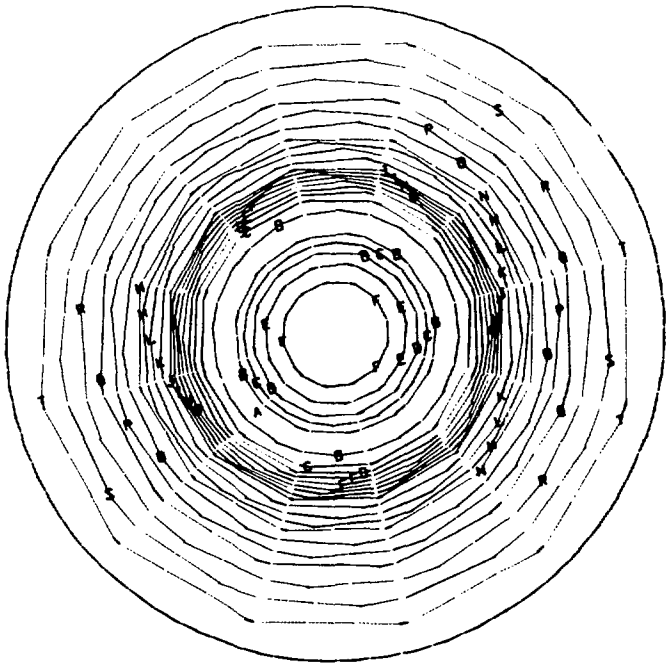

IDENTIFICATION	CONTOUR VALUE
A A A A	-1.768E+10
B B B B	-1.708E+10
C C C C	-1.647E+10
D D D D	-1.587E+10
E E E E	-1.526E+10
F F F F	-1.466E+10
G G G G	-1.405E+10
H H H H	-1.344E+10
I I I I	-1.284E+10
J J J J	-1.223E+10
K K K K	-1.163E+10
L L L L	-1.102E+10
M M M M	-1.042E+10
N N N N	-9.810E+09
O O O O	-9.204E+09
P P P P	-8.599E+09
Q Q Q Q	-7.993E+09
R R R R	-7.387E+09
S S S S	-6.782E+09
T T T T	-6.176E+09
U U U U	-5.571E+09

r-θ Plane
a

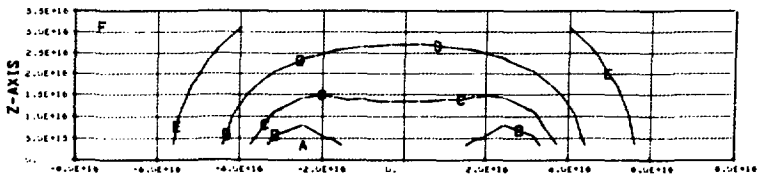

IDENTIFICATION	CONTOUR VALUE
A A A A	-1.768E+10
B B B B	-1.616E+10
C C C C	-1.261E+10
D D D D	-1.008E+10
E E E E	-7.640E+09
F F F F	-6.006E+09

r-z Plane
b

t = 0
Gravitational Potential(ergs/g)
FIGURE 39

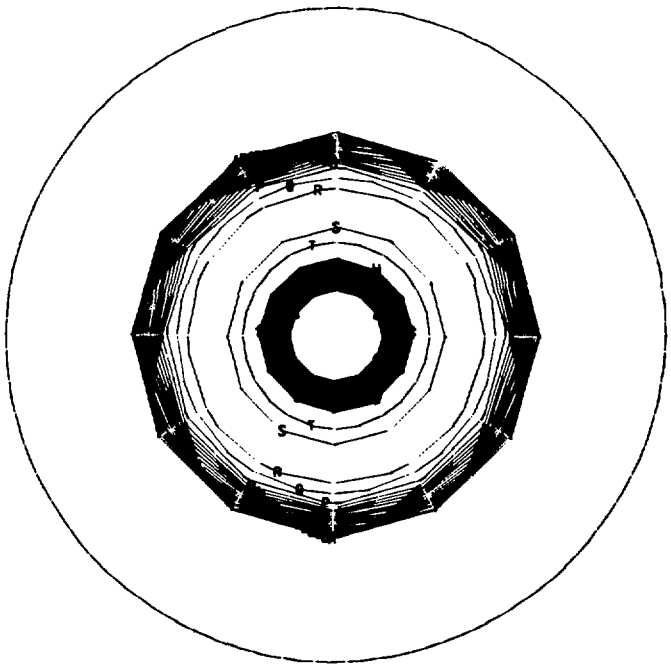

IDENTIFICATION	CONTOUR VALUE
A	0.
B	1.383E-13
C	2.766E-13
D	4.148E-13
E	5.531E-13
F	6.914E-13
G	8.297E-13
H	9.680E-13
I	1.106E-12
J	1.246E-12
K	1.383E-12
L	1.521E-12
M	1.659E-12
N	1.798E-12
O	1.936E-12
P	2.074E-12
Q	2.212E-12
R	2.351E-12
S	2.489E-12
T	2.627E-12
U	2.766E-12

r-θ Plane
a

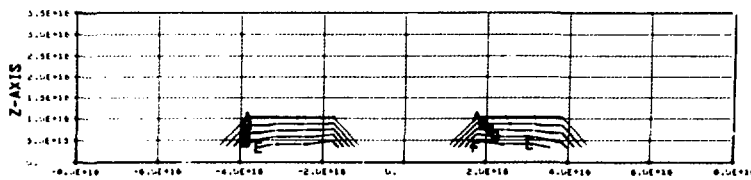

IDENTIFICATION	CONTOUR VALUE
A	0.
B	5.531E-13
C	1.106E-12
D	1.659E-12
E	2.212E-12
F	2.766E-12

r-z Plane
b

t = 0

Angular Velocity(s^{-1})

FIGURE 40

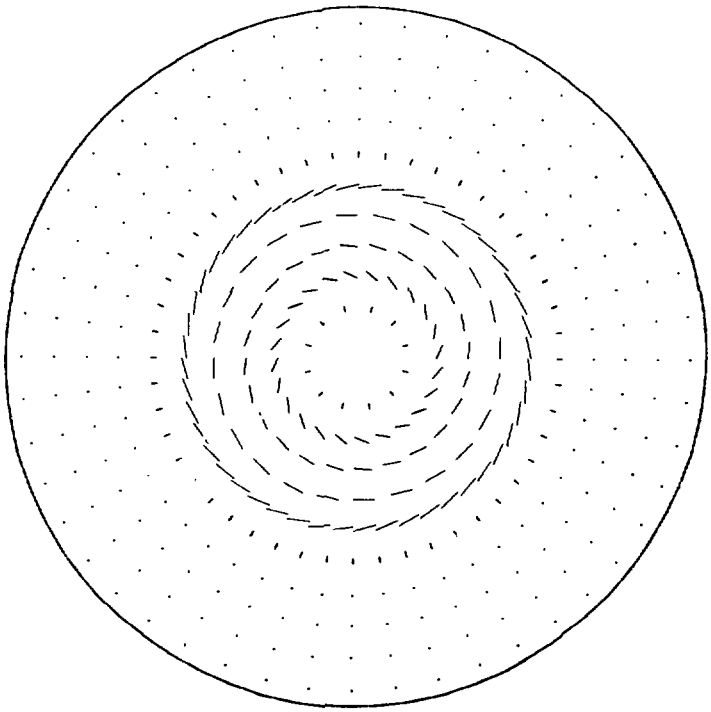

a
Velocity(cm/s)

$u_{max} = 2.17 \times 10^{4}$

$v_{max} = 7.84 \times 10^{4}$

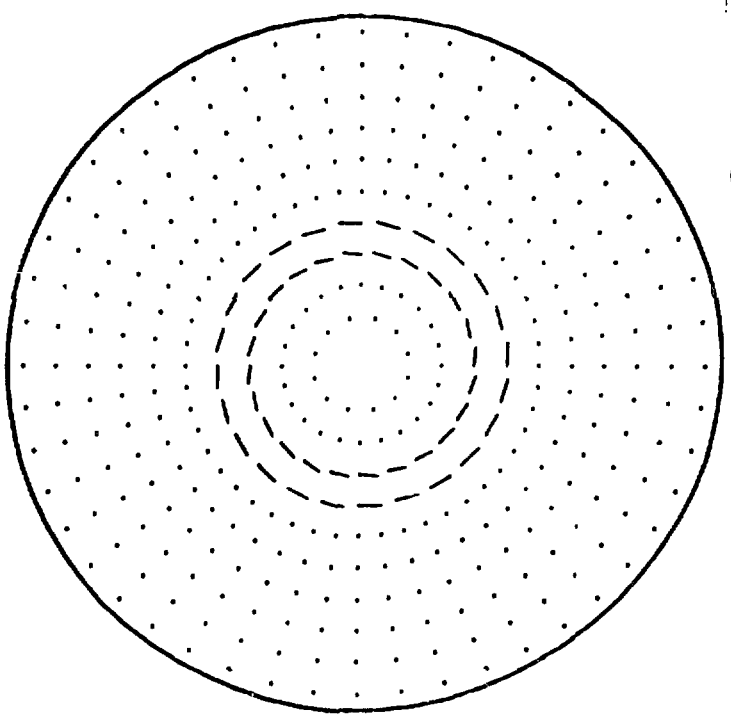

b
Momentum Density(g/cm^2s)

$(\rho u)_{max} = 5.84 \times 10^{-13}$

$(\rho v)_{max} = 1.30 \times 10^{-11}$

t = 0
Laboratory Frame
FIGURE 41

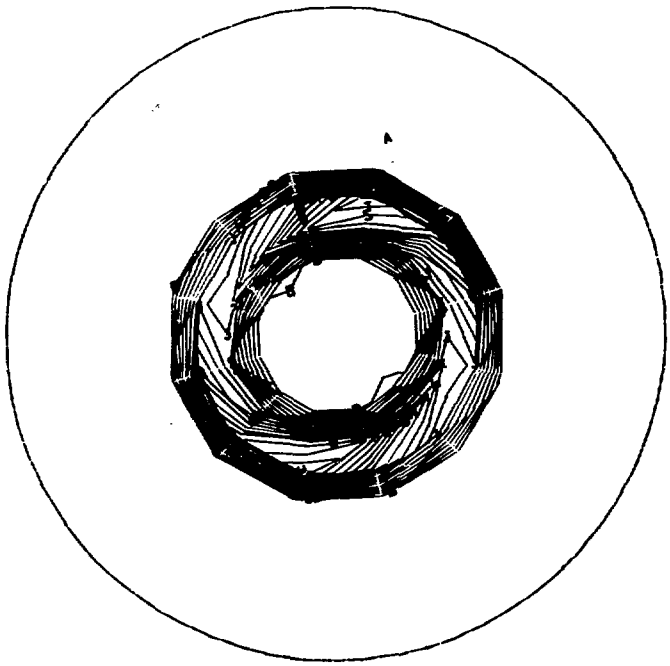

IDENTIFICATION	CONTOUR VALUE
A A A A	7.719E-29
B B B B	1.314E-17
C C C C	2.629E-17
D D D D	3.943E-17
E E E E	5.258E-17
F F F F	6.572E-17
G G G G	7.886E-17
H H H H	9.201E-17
I I I I	1.052E-16
J J J J	1.183E-16
K K K K	1.314E-16
L L L L	1.446E-16
M M M M	1.577E-16
N N N N	1.709E-16
O O O O	1.840E-16
P P P P	1.972E-16
Q Q Q Q	2.103E-16
R R R R	2.234E-16
S S S S	2.366E-16
T T T T	2.497E-16
U U U U	2.629E-16

$t = 0.44 \times 10^5$ yrs
a

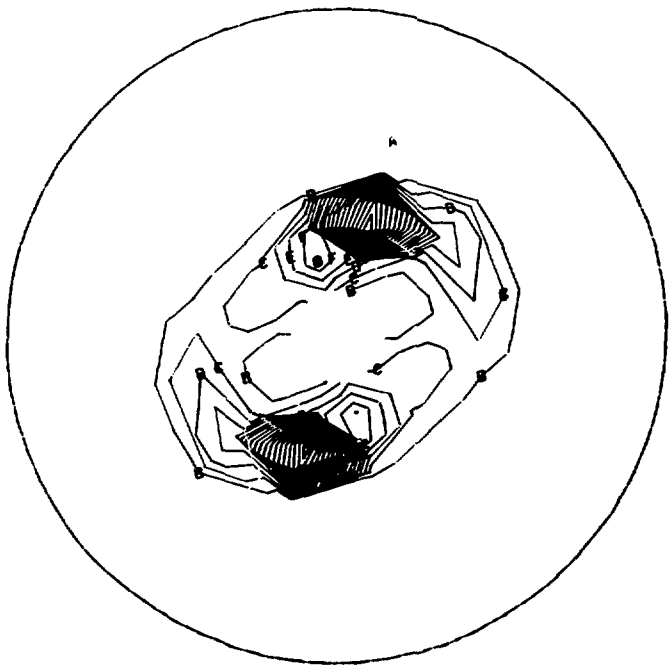

IDENTIFICATION	CONTOUR VALUE
A A A A	5.708E-30
B B B B	2.492E-17
C C C C	4.985E-17
D D D D	7.477E-17
E E E F	9.969E-17
F F F F	1.246E-16
G G G G	1.496E-16
H H H H	1.746E-16
I I I I	1.994E-16
J J J J	2.243E-16
K K K K	2.492E-16
L L L L	2.742E-16
M M M M	2.991E-16
N N N N	3.240E-16
O O O O	3.489E-16
P P P P	3.738E-16
Q Q Q Q	3.988E-16
R R R R	4.237E-16
S S S S	4.486E-16
T T T T	4.735E-16
U U U U	4.985E-16

$t = 0.60 \times 10^5$ yrs
b

Density(g/cm^3)
FIGURE 42

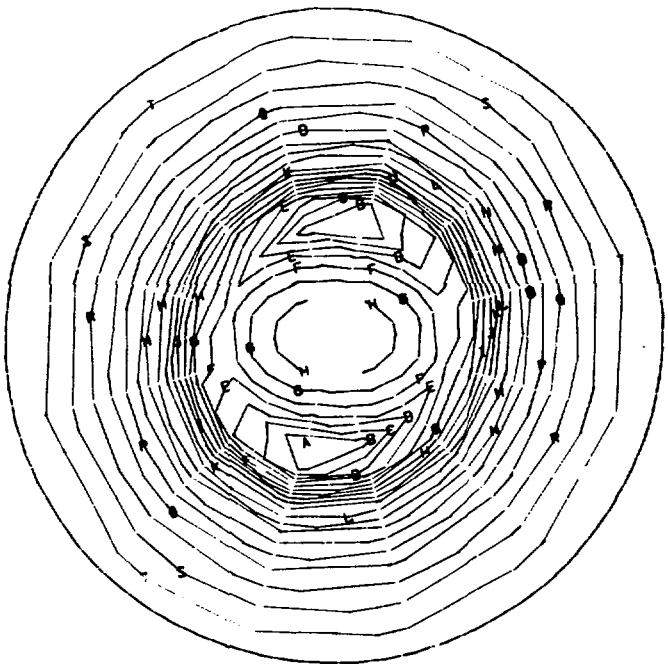

IDENTIFICATION	CONTOUR VALUE
A A A A	-1.929E+10
B B B B	-1.860E+10
C C C C	-1.791E+10
D D D D	-1.721E+10
E E E E	-1.652E+10
F F F F	-1.583E+10
G G G G	-1.514E+10
H H H H	-1.445E+10
I I I I	-1.376E+10
J J J J	-1.307E+10
K K K K	-1.238E+10
L L L L	-1.169E+10
M M M M	-1.099E+10
N N N N	-1.030E+10
O O O O	-9.612E+09
P P P P	-8.921E+09
Q Q Q Q	-8.230E+09
R R R R	-7.539E+09
S S S S	-6.848E+09
T T T T	-6.156E+09
U U U U	-5.465E+09

$t = 0.44 \times 10^5$ yrs
a

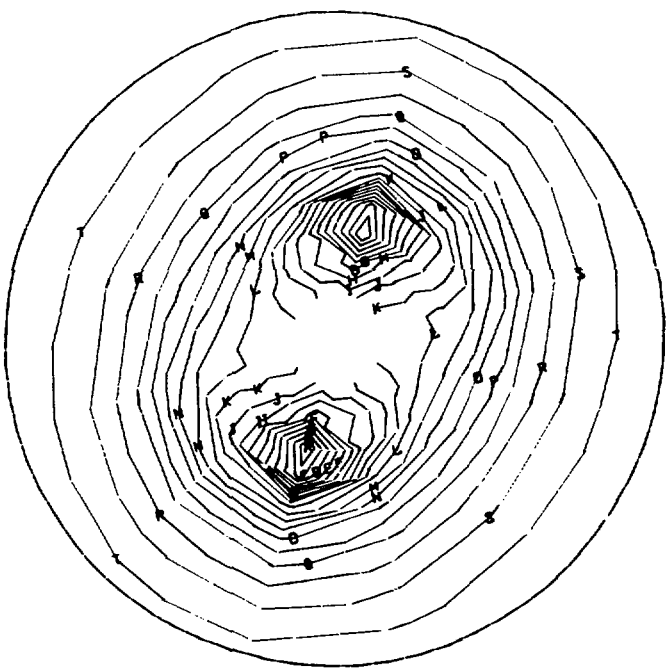

IDENTIFICATION	CONTOUR VALUE
A A A A	-2.562E+10
B B B B	-2.460E+10
C C C C	-2.359E+10
D D D D	-2.257E+10
E E E E	-2.155E+10
F F F F	-2.054E+10
G G G G	-1.952E+10
H H H H	-1.850E+10
I I I I	-1.748E+10
J J J J	-1.647E+10
K K K K	-1.545E+10
L L L L	-1.443E+10
M M M M	-1.342E+10
N N N N	-1.240E+10
O O O O	-1.138E+10
P P P P	-1.037E+10
Q Q Q Q	-9.351E+09
R R R R	-8.334E+09
S S S S	-7.318E+09
T T T T	-6.301E+09
U U U U	-5.284E+09

$t = 0.60 \times 10^5$ yrs
b

Gravitational Potential(ergs/g)
FIGURE 43

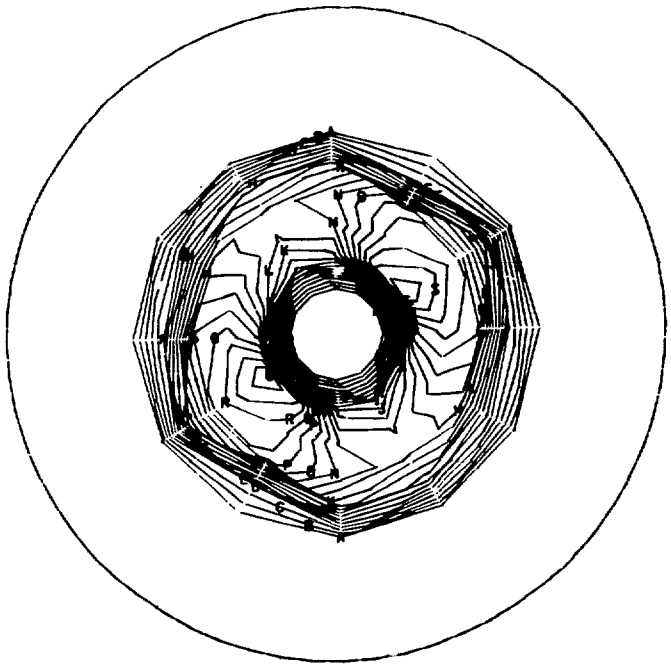

IDENTIFICATION	CONTOUR VALUE
A A A A	0.
B B B B	1.731E-13
C C C C	3.463E-13
D D D D	5.194E-13
E E E E	6.926E-13
F F F F	8.657E-13
G G G G	1.039E-12
H H H H	1.212E-12
I I I I	1.386E-12
J J J J	1.660E-12
K K K K	1.731E-12
L L L L	1.905E-12
M M M M	2.078E-12
N N N N	2.261E-12
O O O O	2.424E-12
P P P P	2.597E-12
Q Q Q Q	2.770E-12
R R R R	2.943E-12
S S S S	3.117E-12
T T T T	3.290E-12
U U U U	3.463E-12

$t = 0.44 \times 10^5$ yrs
a

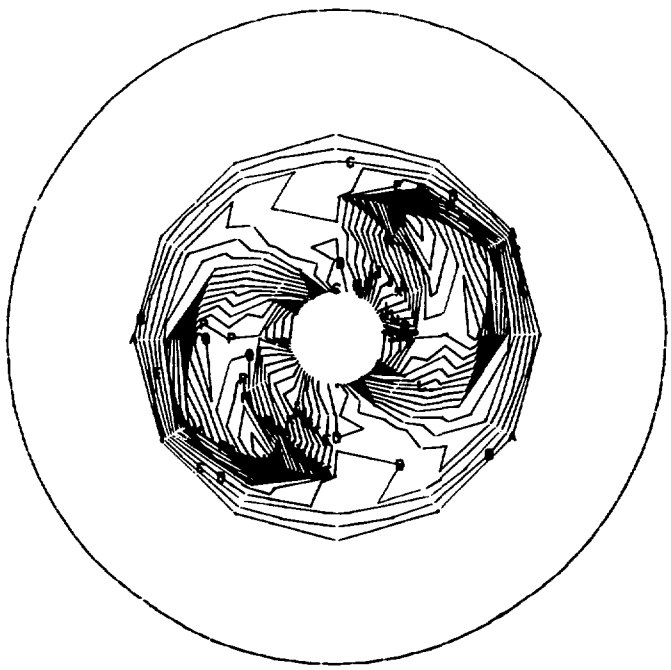

IDENTIFICATION	CONTOUR VALUE
A A A A	0.
B B B B	2.492E-13
C C C C	4.985E-13
D D D D	7.477E-13
E E E E	9.970E-13
F F F F	1.246E-12
G G G G	1.495E-12
H H H H	1.745E-12
I I I I	1.994E-12
J J J J	2.243E-12
K K K K	2.492E-12
L L L L	2.742E-12
M M M M	2.991E-12
N N N N	3.240E-12
O O O O	3.489E-12
P P P P	3.739E-12
Q Q Q Q	3.988E-12
R R R R	4.237E-12
S S S S	4.486E-12
T T T T	4.736E-12
U U U U	4.985E-12

$t = 0.60 \times 10^5$ yrs
b

Angular Velocity(s^{-1})
FIGURE 44

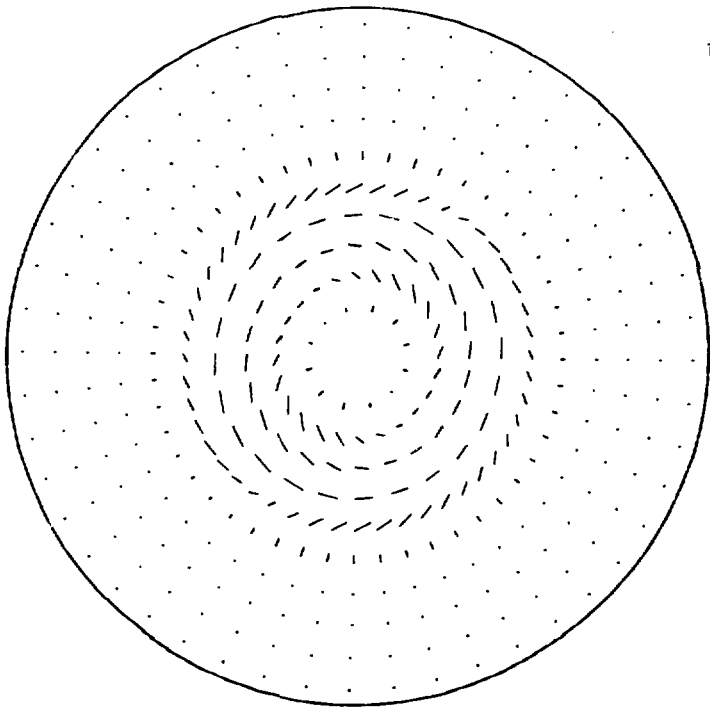

$t = 0.44^{a} \times 10^{5}$ yrs

$u_{max} = 4.12 \times 10^{4}$

$v_{max} = 8.77 \times 10^{4}$

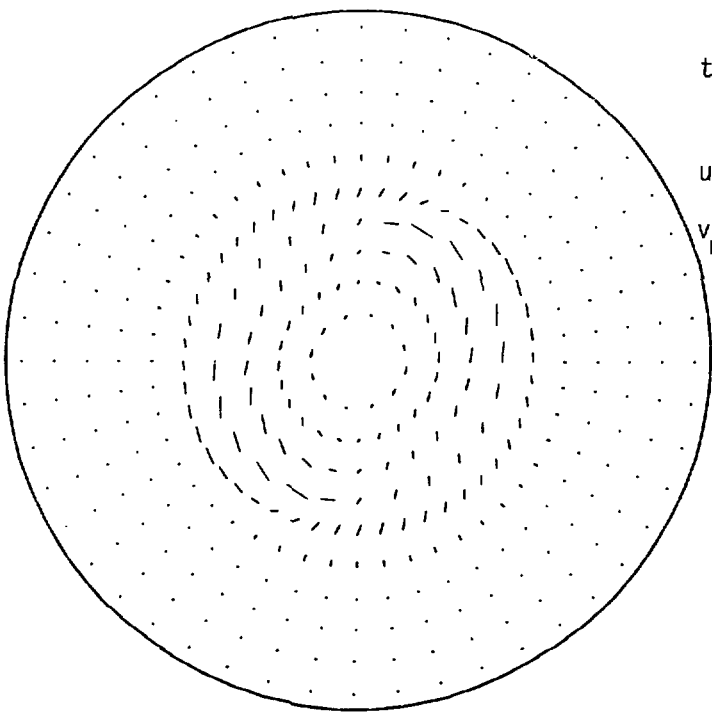

$t = 0.60^{b} \times 10^{5}$ yrs

$u_{min} = -6.56 \times 10^{4}$

$v_{max} = 1.41 \times 10^{5}$

Velocity(cm/s)
Laboratory Frame
FIGURE 45

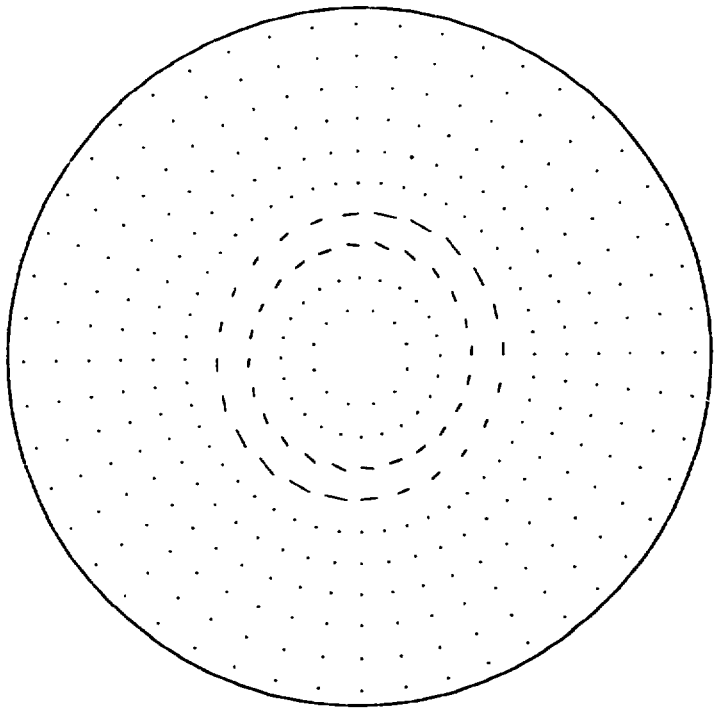

a
$t = 0.44 \times 10^5$ yrs

$(\rho u)_{max} = 2.76 \times 10^{-12}$

$(\rho v)_{max} = 2.06 \times 10^{-11}$

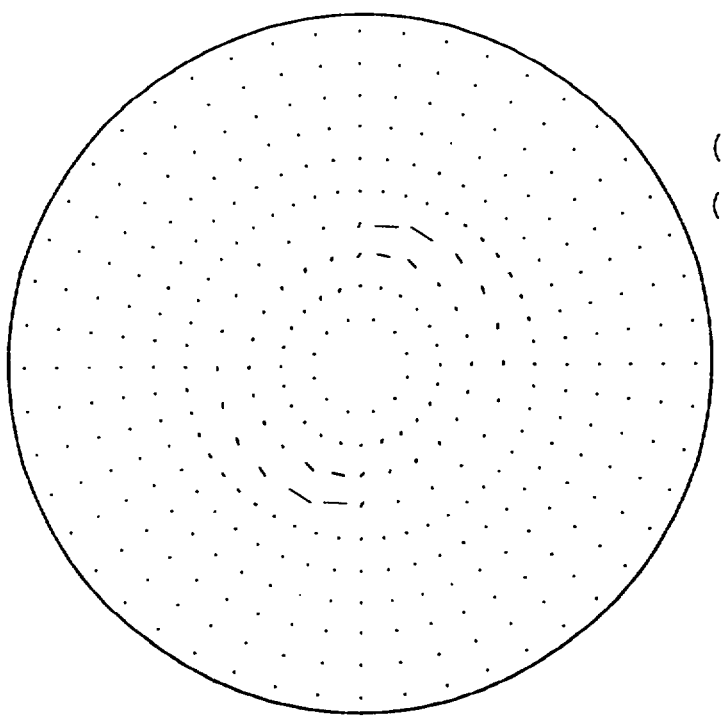

b
$t = 0.60 \times 10^5$ yrs

$(\rho u)_{min} = -8.28 \times 10^{-12}$

$(\rho v)_{max} = 4.03 \times 10^{-11}$

Momentum Density($g/cm^2 s$)
Rotating Frame
FIGURE 46

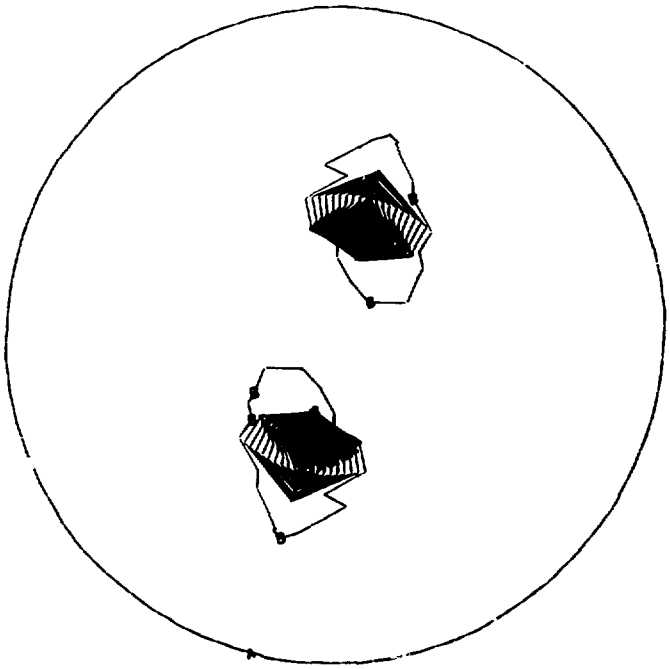

IDENTIFICATION	CONTOUR VALUE
A A A A	3.075E-24
B B B B	4.133E-17
C C C C	8.266E-17
D D D D	1.240E-16
E E E E	1.653E-16
F F F F	2.066E-16
G G G G	2.480E-16
H H H H	2.893E-16
I I I I	3.306E-16
J J J J	3.720E-16
K K K K	4.133E-16
L L L L	4.546E-16
M M M M	4.959E-16
N N N N	5.373E-16
O O O O	5.786E-16
P P P P	6.199E-16
Q Q Q Q	6.613E-16
R R R R	7.026E-16
S S S S	7.439E-16
T T T T	7.852E-16
U U U U	8.266E-16

r-θ Plane
a

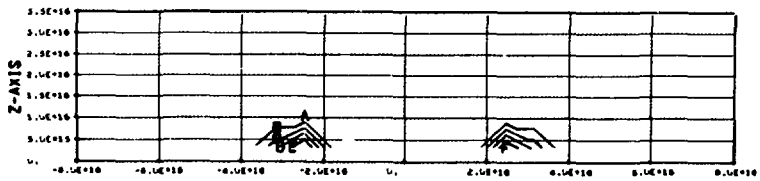

IDENTIFICATION	CONTOUR VALUE
A A A A	2.110E-30
B B B B	1.653E-16
C C C C	3.306E-16
D D D D	4.959E-16
E E E E	6.613E-16
F F F F	8.266E-16

r-z Plane
b

$t = 0.76 \times 10^5$ yrs

Density(g/cm^3)

FIGURE 47

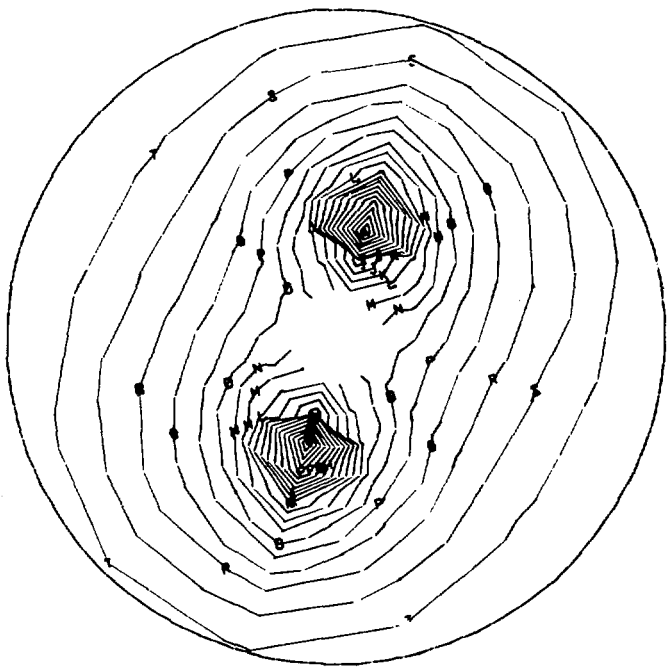

IDENTIFICATION	CONTOUR VALUE
A A A A	-3.088E+10
B B B B	-2.959E+10
C C C C	-2.831E+10
D D D D	-2.702E+10
E E E E	-2.574E+10
F F F F	-2.446E+10
G G G G	-2.316E+10
H H H H	-2.188E+10
I I I I	-2.059E+10
J J J J	-1.931E+10
K K K K	-1.802E+10
L L L L	-1.674E+10
M M M M	-1.546E+10
N N N N	-1.417E+10
O O O O	-1.288E+10
P P P P	-1.159E+10
Q Q Q Q	-1.031E+10
R R R R	-9.023E+09
S S S S	-7.738E+09
T T T T	-6.452E+09
U U U U	-5.166E+09

r-θ Plane
a

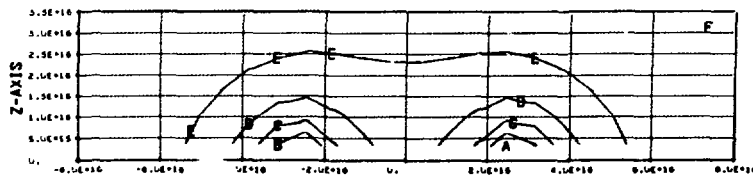

IDENTIFICATION	CONTOUR VALUE
A A A A	-3.088E+10
B B B B	-2.578E+10
C C C C	-2.067E+10
D D D D	-1.557E+10
E E E E	-1.047E+10
F F F F	-5.368E+09

r-z Plane
b

$t = 0.76 \times 10^5$ yrs
Gravitational Potential(ergs/g)
FIGURE 48

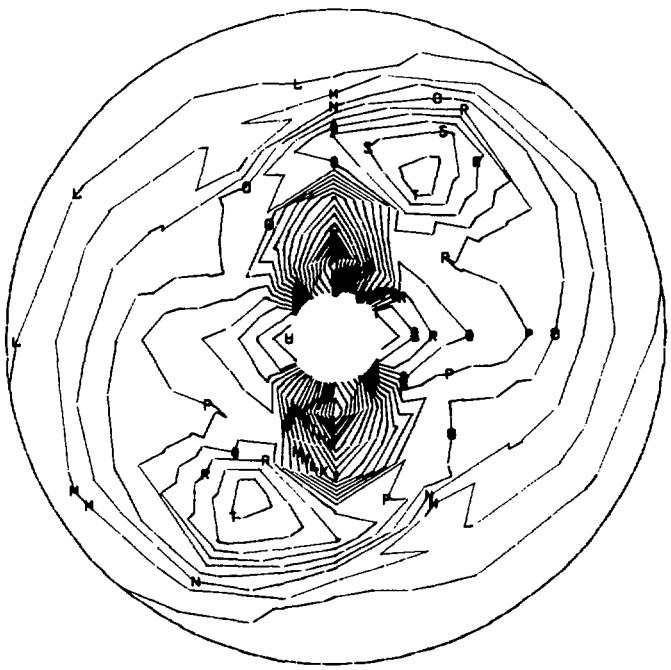

IDENTIFICATION	CONTOUR VALUE
A A A A	-5.799E-12
B B B B	-5.247E-12
C C C C	-4.695E-12
D D D D	-4.143E-12
E E E E	-3.591E-12
F F F F	-3.039E-12
G G G G	-2.487E-12
H H H H	-1.936E-12
I I I I	-1.384E-12
J J J J	-8.318E-13
K K K K	-2.799E-13
L L L L	2.720E-13
M M M M	8.239E-13
N N N N	1.376E-12
O O O O	1.928E-12
P P P P	2.480E-12
Q Q Q Q	3.031E-12
R R R R	3.583E-12
S S S S	4.135E-12
T T T T	4.687E-12
U U U U	5.239E-12

r-θ Plane
a

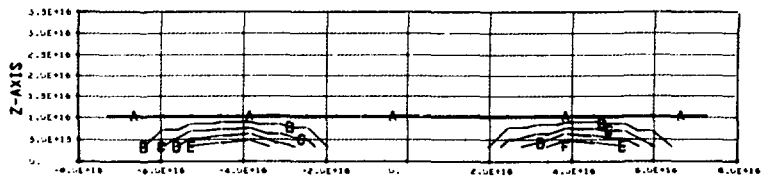

IDENTIFICATION	CONTOUR VALUE
A A A A	0.
B B B B	1.028E-12
C C C C	2.056E-12
D D D D	3.085E-12
E E E E	4.113E-12
F F F F	5.141E-12

r-z Plane
b

$t = 0.76 \times 10^5$ yrs
Angular Velocity(s^{-1})
FIGURE 49

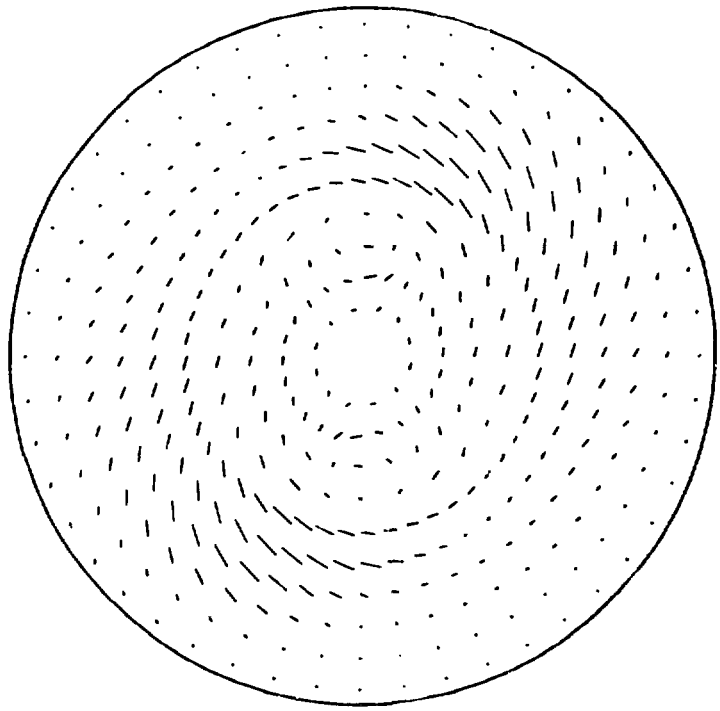

a
Laboratory Frame

$u_{max} = 9.45 \times 10^4$

$v_{max} = 1.91 \times 10^5$

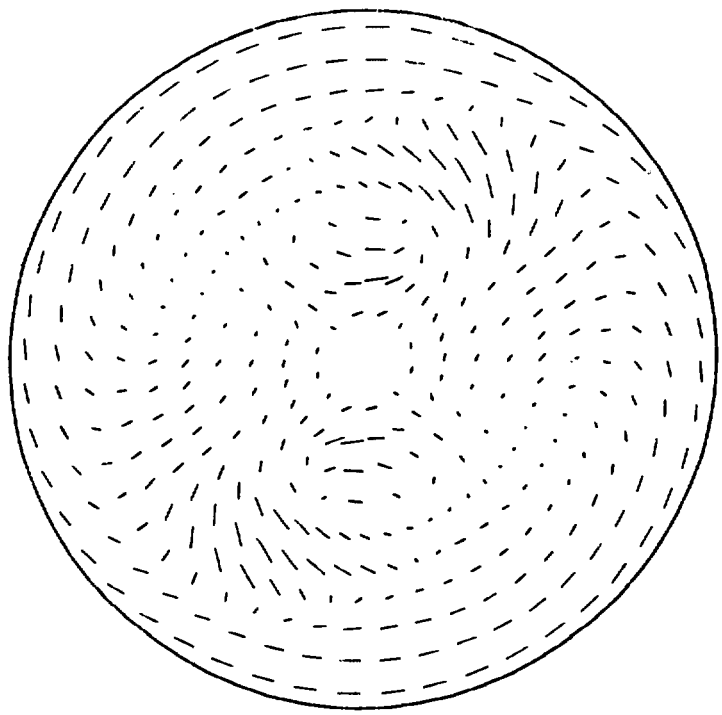

b
Rotating Frame

$u_{max} = 9.45 \times 10^4$

$v_{min} = -1.32 \times 10^5$

$t = 0.76 \times 10^5$ yrs
Velocity(cm/s)
FIGURE 50

2. Case II

a. Initial conditions

The toroid used in Case II, having an A of 7.5×10^{19}, is a more dispersed body than the one used in Case I. The Case II ring has a characteristic cross-sectional radius of 1.60×10^{16} cm. This radius encompasses about 2 linear zone dimensions; so the resolution of the body is greatly improved. The maximum-density contour is 2.85×10^{16} cm from the axis of rotation. Table II presents a summary of the physical properties of the Case II initial conditions.

Figure 51a, b shows the density contours of the system at the time of perturbation. The density in the r-θ plane decreases from a maximum central value of 9.47×10^{-17} g/cm^3 to a value of 4.74×10^{-18} g/cm^3, a factor of 20, in a distance of about 2½ radial zones. The gradient is therefore fairly well resolved by the calculational grid. The cross-sectional area of the toroid is shown in Fig. 51b to be nearly circular. The gravitational potential for the initial configuration is illustrated in Fig. 52a, b. The well is centered on the inner edge of the ring and is broader and less deep than in Case I. The potential contours in the r-z plane are similar to those in Fig. 39b, but are more diffuse, reflecting the more extended and less dense toroid.

During the initialization calculation the larger toroid of Case II develops more differential rotation than its more compact predecessor, as displayed in Fig. 53a, b. In the r-θ plane one sees sharp gradients only on the outer edge of the ring. The density of the gas near the axis of rotation is high enough for the numerical scheme to have turned on the velocities in this region; and because of conservation of angular momentum, the orbiting mass originally in the nonequilibrium toroid

moves with higher angular velocities as it falls toward the z-axis. In the r-z plane the toroid appears to be very nearly in solid body rotation at least in the high density regions.

The laboratory velocity and momentum-density vector fields of Fig. 54a, b support the interpretation of the angular velocity contours given above. In Fig. 54a the velocity field suggests that the toroid will not contract to as poorly a resolved configuration as for Case I. These velocities have almost no radial component except at the outer edge of the toroid where some accretion is indicated. The ring has expanded from its nonequilibrium state, has overshot the steady state configuration due to the linear momentum gained during expansion, and is now slightly recontracting at the outer edge. In the momentum-density vector field, one has a graphic representation of the mass concentration as it is spread over four radial zones.

Table II

Initial Conditions

Case II

$A(cm^4/g^{2/3}\ s^2)$	7.50×10^{19}	M(g)	5.91×10^{33}
a(cm)	1.60×10^{16}	W(ergs)	-4.09×10^{43}
$\rho'_{max}(g/cm^3)$	9.93×10^{-17}	KE(ergs)	1.50×10^{41}
$R'_{\rho_{max}}$ (cm)	2.85×10^{16}	U(ergs)	1.05×10^{43}
$\rho_{max}(g/cm^3)$	9.47×10^{-17}	T(ergs)	1.23×10^{43}
$R_{\rho_{max}}$ (cm)	3.15×10^{16}	E(ergs)	-1.80×10^{43}
t_f(yrs)	0.07×10^{5}	$J(g\ cm^2/s)$	1.19×10^{55}
$\omega(s^{-1})$	2.06×10^{-12}	$\Theta(°K)$	18.7

b. Fragmentation of the toroid

The time scale for the evolution of this system is greater by almost a factor of 3 than the time scale for Case I. The local free-fall time estimate is 0.07×10^5 yrs, and is therefore only greater by some 40%. It is, however, expected that more compact systems will evolve on shorter time scales, since the thermal pressures tending to impede contraction are lower.

In Fig. 55a, b the density contours at $t = 1.10 \times 10^5$ yrs and at $t = 1.27 \times 10^5$ yrs summarize the intermediate stages of mass accretion from the toroid onto the newly formed fragments. The thermal pressures are sufficient to delay the accretion and to produce moderately well-resolved extended binary components. The gravitational potential at these times is shown in Fig. 56a, b. The contours display the evolution and deepening of the new centers of gravitational attraction. The apparent secondary modes in Fig. 56b are artifacts of the interpolation scheme used to obtain the contour lines since the potential field can not respond to instabilities more rapidly than the mass configuration and since the density contours show only the mode 2 perturbation at this time.

c. Spinning components

At the second of the intermediate times reported, $t = 1.27 \times 10^5$ yrs, the components are elongated. This configuration demonstrates graphically one especially noteworthy aspect of the fragmentation dynamics. The perturbation is applied to the initial ring through the azimuthal velocity field. On one side of $\theta = 90°$ the velocities are increased by 1% and on the other side they are retarded by 1%.

Exactly the same perturbation is centered on $\theta = 270°$, but in the following discussion it is only necessary to consider one of the favored centers of accretion. The mass in the region where the velocities are increased feels a greater centrifugal force after the perturbation; and therefore experiences a net outward radial motion. The centrifugal force acting on the gas in the region where velocities have been decreased is reduced, and the mass can move radially inward. This effect results not just because of the 1% change in the angular velocity that arises from the original perturbation, but also because the continued acceleration toward the binary centers of condensation enhance even further the departure of angular velocities from the unperturbed initial values.

The extended body that is forming out of the toroid now encounters more slowly moving mass on its leading edge at a smaller radial distance from the axis of rotation than the radial separation of the center of the object from the axis. The result is a retardation of the azimuthal velocities in regions on the axis side of its center. Exactly the opposite mechanisms work to accelerate regions of the body on the outward side. The fragmenting bodies begin therefore to spin in a co-rotational sense relative to their orbital motion. Many multiple star systems do in fact exhibit co-rotational spins. In a satellite system such as our own solar system, one observes co-rotating bodies. In fact, if retrograde motion is observed one generally hypothesizes that the system resulted from a capture process rather than from fragmentation.[65] Further discussion of retrograde motion is deferred to the next section.

Centrifugal forces are not the only forces that directly influence the development of spin in the fragments. Coriolis forces resist the spin-up of the objects by increasing the angular velocity of the mass segments moving inward and by decreasing the angular velocity of the mass moving outward. In the rotating frame momentum-density vector fields displayed in Fig. 59a, b one sees the co-rotation of the components.

The angular velocity plots presented in Fig. 57a, b illustrate the same phenomenon. In reference to these more complicated configurations it should be emphasized that the contour plots of angular velocity can be somewhat deceptive unless interpreted very carefully. All that these contour plots exhibit are the locations of maximum and minimum angular velocity, and they carry no information about the concurrent magnitudes and directions of radial velocity. As a result it is not possible from these contours alone to determine the position of vortices. Nevertheless, the angular velocity contours prove useful as a means for showing the character of the spin field around the central axis. In particular, they show several consistent trends in the relative angular phasing between the positions of maximum density and those of maximum angular velocity. In the present case, for example, Fig. 57a shows advancing fingers of high spin at the outer trailing edges of the condensing objects. By comparing the contours in this figure at these two intermediate times one observes that the magnitude of the spin is increasing.

Figure 58a, b summarizes the movement of the mass from the toroid to the binary fragments in the momentum density representation of the laboratory frame. In Fig. 60a, b one observes two laboratory momentum-

density vector fields in the r-z plane. At $t = 1.10 \times 10^5$ yrs, most of the momentum flux is radially outward; at $t = 1.27 \times 10^5$ yrs the field is split at the equator, showing the bulging of the body as it begins to spin.

d. Spirals and retrograde satellites

Figure 61a, b shows the density contours for Case II at a time of 1.42×10^5 yrs after the perturbation. The central density of each component has increased to twice that of the initial toroid. In the r-θ plane a spiral structure has developed. The mass in the streamers is gravitationally bound to the nearest component, and it is possible that these regions provide an environment in which satellites could form. Since the binary objects are increasing their spin in a positive sense, it is to be expected that dynamical coupling to adjacent regions of fluid would result in regions of negative spin as a manifestation of conservation of overall angular momentum. The rotating-frame velocity vector field of Fig. 65a substantiates this speculation, since clockwise vortices are developing at angles of 150° and 300° in the respective spirals. Spinning binaries with accompanying mass streamers are therefore a possible alternative to capture processes for initiating retrograde satellite motions. The phenomenon of spirals is considered further in Section D of this chapter.

e. Equatorial distortions

The r-z density contours in Fig. 61b demonstrate the oblate nature of the components. The flattening into the equatorial plane is the result of two physical processes. First, the spinning components bulge equatorially under the action of centrifugal force. Second, the

protostars are modelled as very compressible fluids, which therefore flow along the gravitational potential gradients rather freely. The gas on the axial side of each object senses the field of the companion more strongly than the gas on the outward side of the component centers. The effect is a large tidal distortion. The gravitational potential contours of Fig. 62a, b also depict the tidal elongation of the components toward one another. The angular velocity plots in Fig. 63a, b show the accelerating and deaccelerating effects of accretion. The laboratory velocity and momentum-density vector fields summarized in Fig. 64a, b also illustrate this effect.

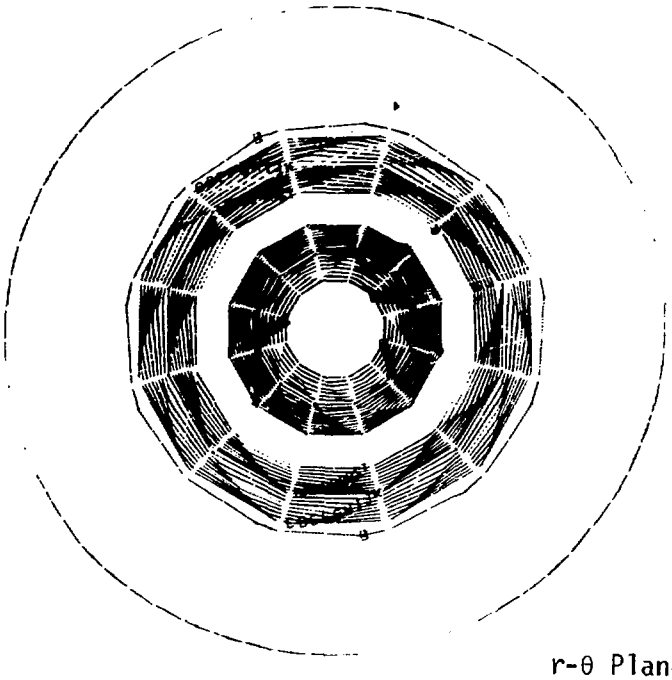

IDENTIFICATION	CONTOUR VALUE
A	1.700E-29
B	4.736E-18
C	9.472E-18
D	1.421E-17
E	1.894E-17
F	2.368E-17
G	2.842E-17
H	3.315E-17
I	3.789E-17
J	4.263E-17
K	4.736E-17
L	5.210E-17
M	5.683E-17
N	6.157E-17
O	6.631E-17
P	7.104E-17
Q	7.578E-17
R	8.052E-17
S	8.525E-17
T	8.999E-17
U	9.472E-17

r-θ Plane
a

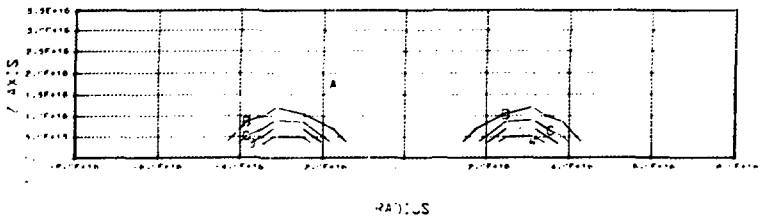

IDENTIFICATION	CONTOUR VALUE
A	1.379E-30
B	1.894E-17
C	3.789E-17
D	5.683E-17
E	7.578E-17
F	9.472E-17

r-z Plane
b

t = C
Density(g/cm^3)
FIGURE 51

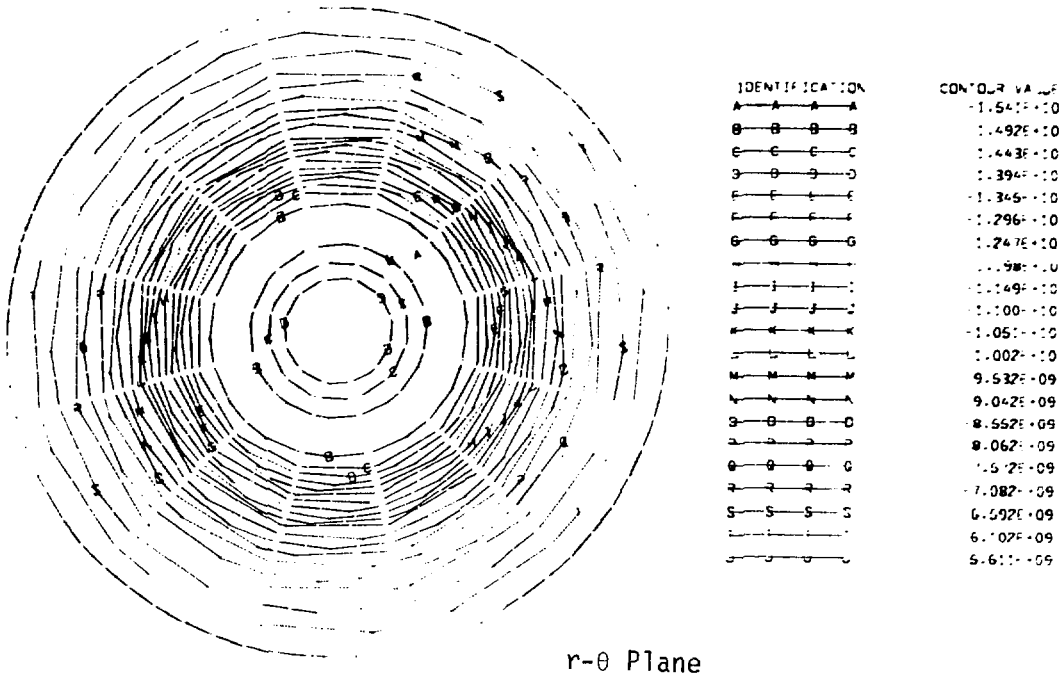

r-θ Plane
a

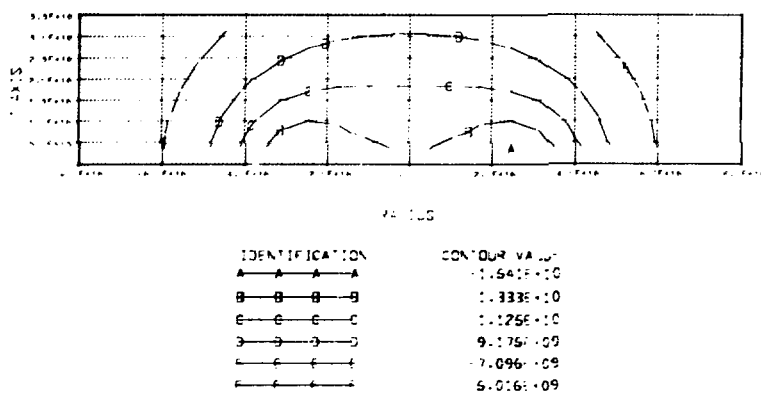

r-z Plane
b

t = 0
Gravitational Potential(ergs/g)
FIGURE 52

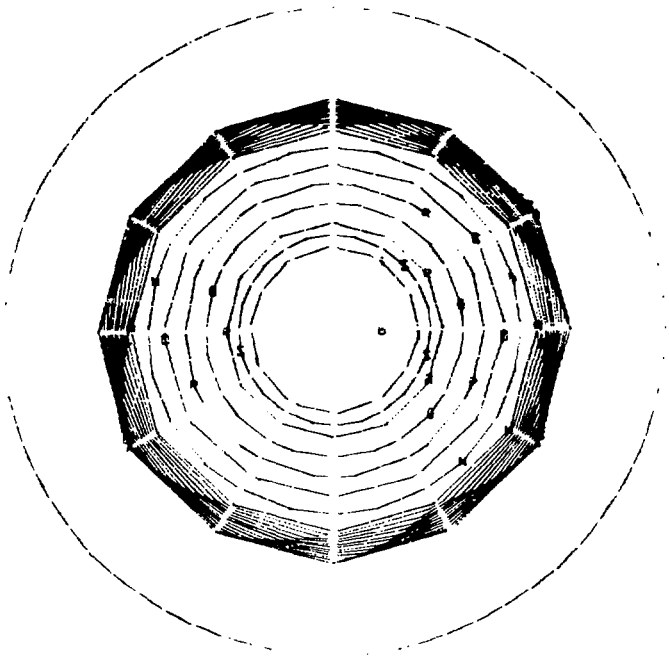

r-θ Plane
a

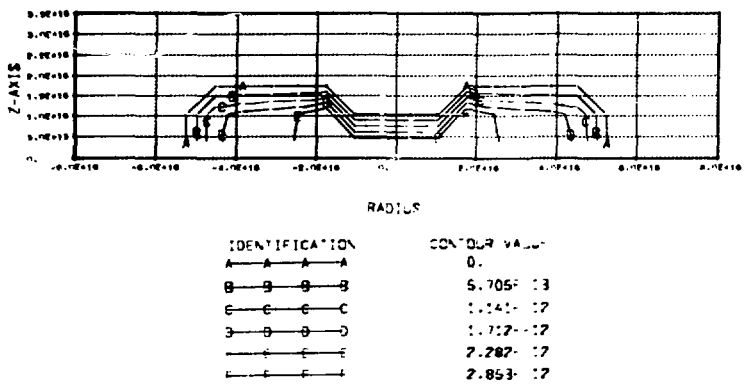

r-z Plane
b

t = 0

Angular Velocity(s^{-1})

FIGURE 53

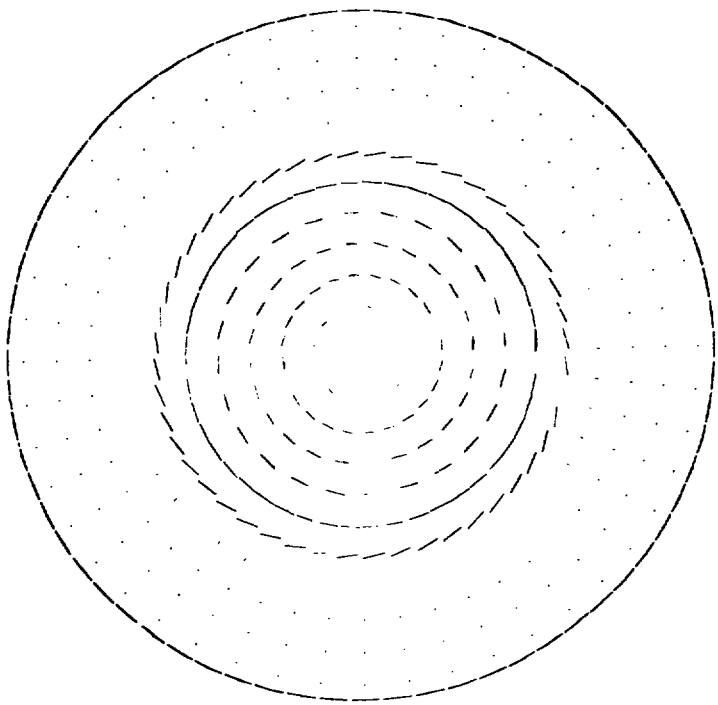

a
Velocity(cm/s)

$u_{min} = -2.00 \times 10^{4}$

$v_{max} = 7.46 \times 10^{4}$

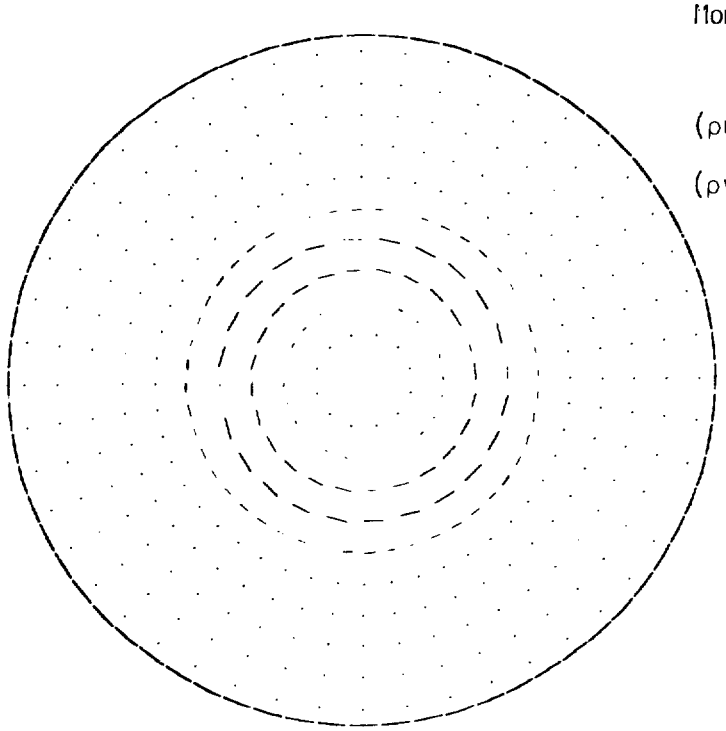

b
Momentum Density($g/cm^2 s$)

$(\rho u)_{min} = -1.23 \times 10^{-13}$

$(\rho v)_{max} = 6.32 \times 10^{-12}$

t = 0
Laboratory Frame
FIGURE 54

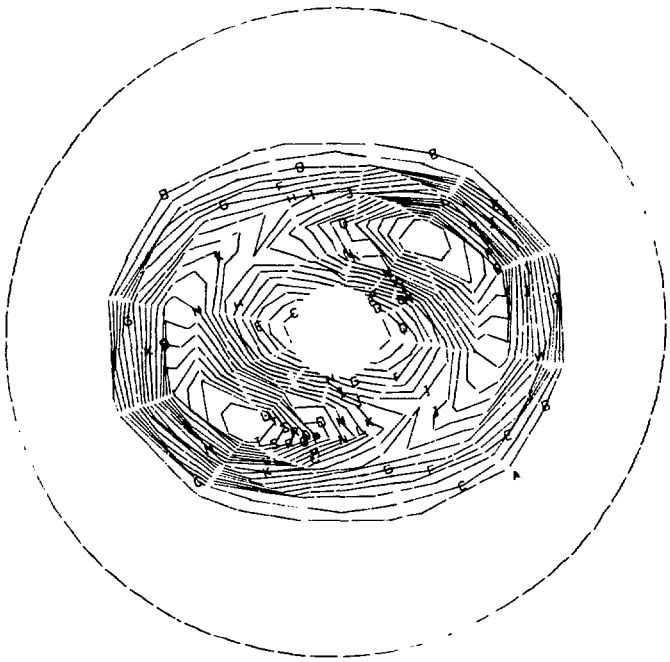

IDENTIFICATION	CONTOUR VALUE
A A A A	8.204E-32
B B B B	5.848E-18
C C C C	1.170E-17
D D D D	1.754E-17
E E E E	2.339E-17
F F F F	2.924E-17
G G G G	3.509E-17
H H H H	4.093E-17
I I I I	4.678E-17
J J J J	5.263E-17
K K K K	5.848E-17
L L L L	6.433E-17
M M M M	7.017E-17
N N N N	7.602E-17
O O O O	8.187E-17
P P P P	8.772E-17
Q Q Q Q	9.356E-17
R R R R	9.941E-17
S S S S	1.053E-16
T T T T	1.111E-16
U U U U	1.170E-16

$t = 1.10 \times 10^5$ yrs
a

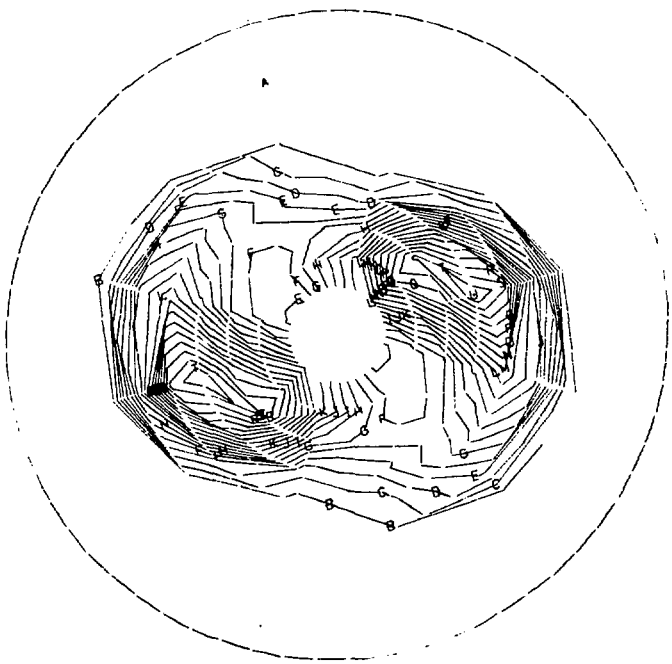

IDENTIFICATION	CONTOUR VALUE
A A A A	6.252E-27
B B B B	6.602E-18
C C C C	1.320E-17
D D D D	1.980E-17
E E E E	2.641E-17
F F F F	3.301E-17
G G G G	3.961E-17
H H H H	4.621E-17
I I I I	5.281E-17
J J J J	5.941E-17
K K K K	6.602E-17
L L L L	7.262E-17
M M M M	7.922E-17
N N N N	8.582E-17
O O O O	9.242E-17
P P P P	9.902E-17
Q Q Q Q	1.056E-16
R R R R	1.122E-16
S S S S	1.188E-16
T T T T	1.254E-16
U U U U	1.320E-16

$t = 1.27 \times 10^5$ yrs
b

Density(g/cm^3)
FIGURE 55

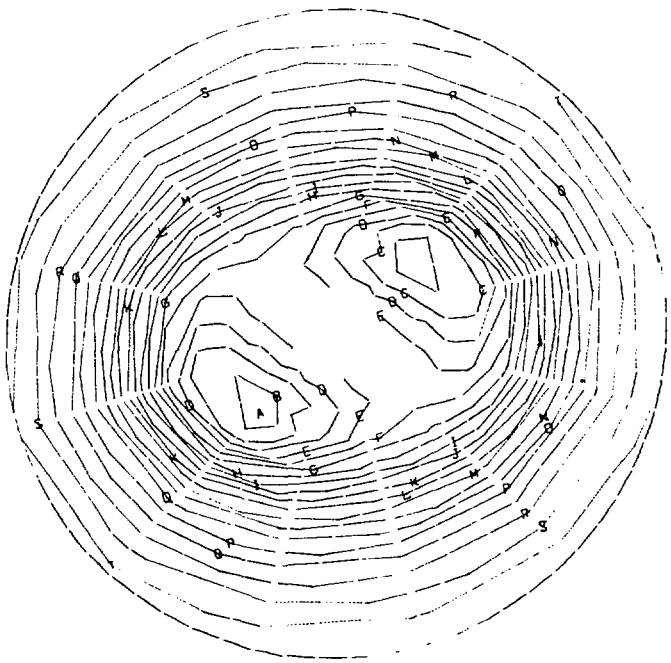

IDENTIFICATION	CONTOUR VALUE
A A A A	-1.629E+10
B B B B	-1.575E+10
C C C C	-1.520E+10
D D D D	-1.465E+10
E E E E	-1.411E+10
F F F F	-1.356E+10
G G G G	-1.302E+10
H H H H	-1.247E+10
I I I I	-1.192E+10
J J J J	-1.138E+10
K K K K	-1.083E+10
L L L L	-1.029E+10
M M M M	-9.741E+09
N N N N	-9.195E+09
O O O O	-8.649E+09
P P P P	-8.103E+09
Q Q Q Q	-7.558E+09
R R R R	-7.012E+09
S S S S	-6.466E+09
T T T T	-5.920E+09
U U U U	-5.374E+09

$t = 1.10 \times 10^5$ yrs

a

IDENTIFICATION	CONTOUR VALUE
A A A A	-1.679E+10
B B B B	-1.622E+10
C C C C	-1.564E+10
D D D D	-1.507E+10
E E E E	-1.449E+10
F F F F	-1.392E+10
G G G G	-1.334E+10
H H H H	-1.277E+10
I I I I	-1.219E+10
J J J J	-1.162E+10
K K K K	-1.104E+10
L L L L	-1.047E+10
M M M M	-9.891E+09
N N N N	-9.315E+09
O O O O	-8.740E+09
P P P P	-8.165E+09
Q Q Q Q	-7.589E+09
R R R R	-7.014E+09
S S S S	-6.439E+09
T T T T	-5.863E+09
U U U U	-5.288E+09

$t = 1.27 \times 10^5$ yrs

b

Gravitational Potential(ergs/g)

FIGURE 56

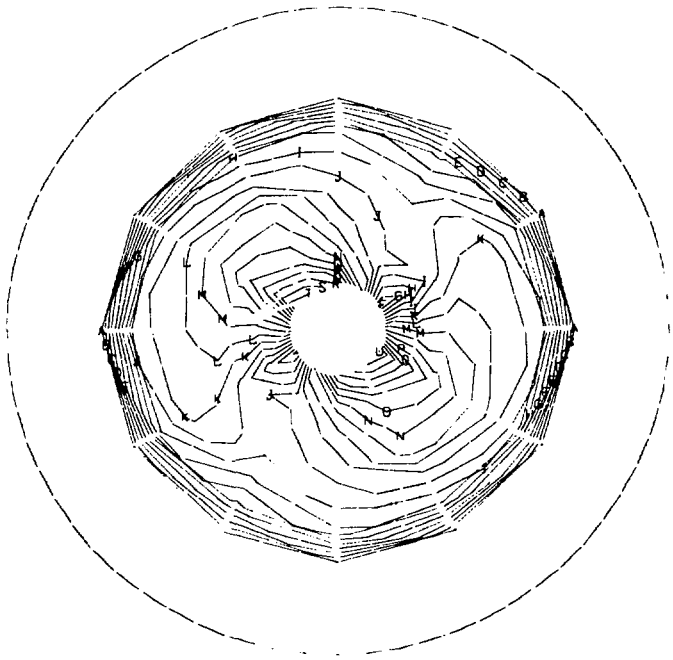

IDENTIFICATION	CONTOUR VALUE
A A A A	0.
B B B B	1.917E-13
C C C C	3.834E-13
D D D D	5.751E-13
E E E E	7.668E-13
F F F F	9.585E-13
G G G G	1.150E-12
H H H H	1.342E-12
I I I I	1.534E-12
J J J J	1.725E-12
K K K K	1.917E-12
L L L L	2.109E-12
M M M M	2.300E-12
N N N N	2.492E-12
O O O O	2.684E-12
P P P P	2.875E-12
Q Q Q Q	3.067E-12
R R R R	3.259E-12
S S S S	3.451E-12
T T T T	3.642E-12
U U U U	3.834E-12

$t = 1.10 \times 10^5$ yrs
a

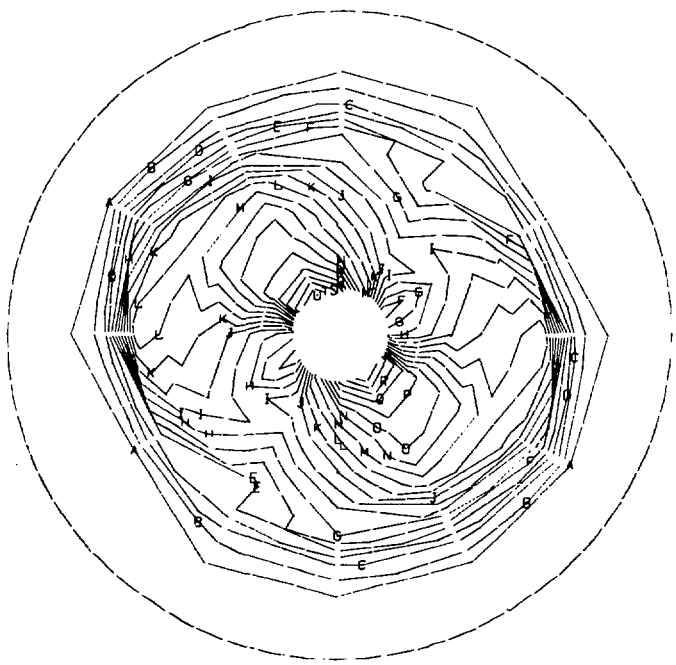

IDENTIFICATION	CONTOUR VALUE
A A A A	0.
B B B B	2.005E-13
C C C C	4.010E-13
D D D D	6.014E-13
E E E E	8.019E-13
F F F F	1.002E-12
G G G G	1.203E-12
H H H H	1.403E-12
I I I I	1.604E-12
J J J J	1.804E-12
K K K K	2.005E-12
L L L L	2.205E-12
M M M M	2.406E-12
N N N N	2.606E-12
O O O O	2.807E-12
P P P P	3.007E-12
Q Q Q Q	3.208E-12
R R R R	3.408E-12
S S S S	3.609E-12
T T T T	3.809E-12
U U U U	4.010E-12

$t = 1.27 \times 10^5$ yrs
b

Angular Velocity(s^{-1})
FIGURE 57

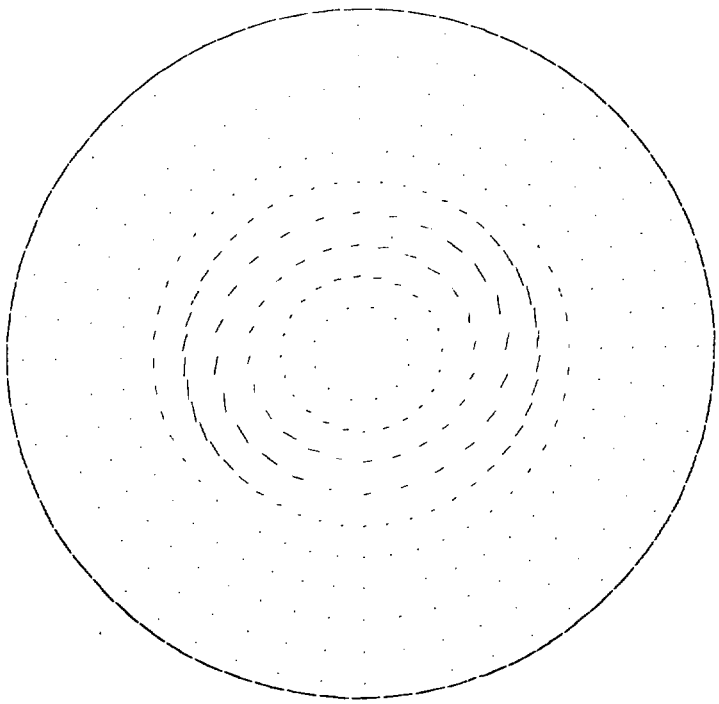

$t = 1.10 \overset{a}{\times} 10^5$ yrs

$(\rho u)_{max} = 1.12 \times 10^{-12}$

$(\rho v)_{max} = 7.19 \times 10^{-12}$

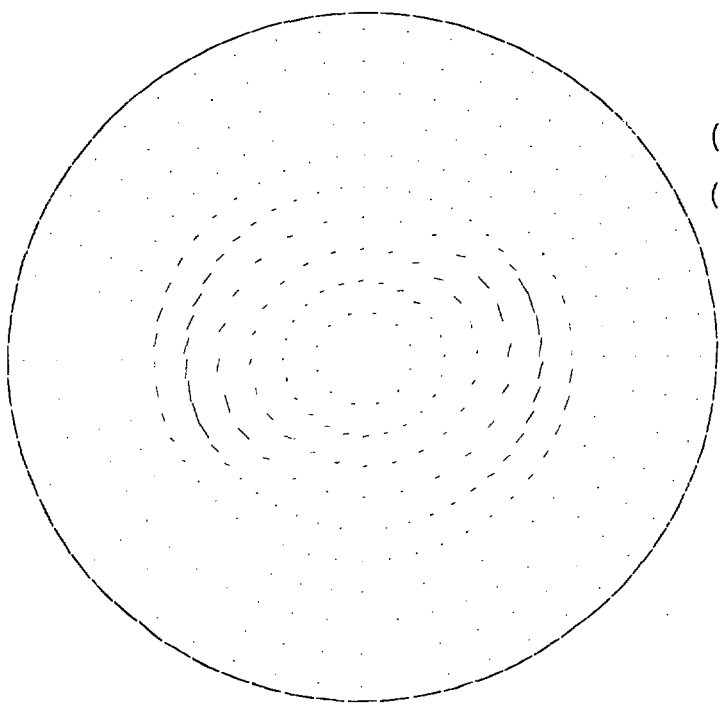

$t = 1.27 \overset{b}{\times} 10^5$ yrs

$(\rho u)_{min} = -2.63 \times 10^{-12}$

$(\rho v)_{max} = 8.51 \times 10^{-12}$

Momentum Density($g/cm^2 s$)
Laboratory Frame
FIGURE 58

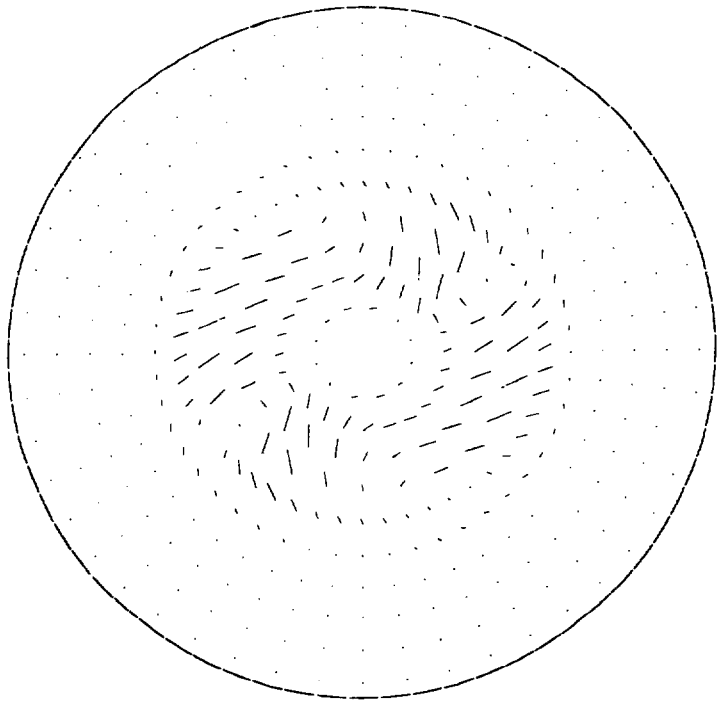

a
$t = 1.10 \times 10^5$ yrs

$(\rho u)_{max} = 1.12 \times 10^{-12}$

$(\rho v)_{max} = 9.14 \times 10^{-13}$

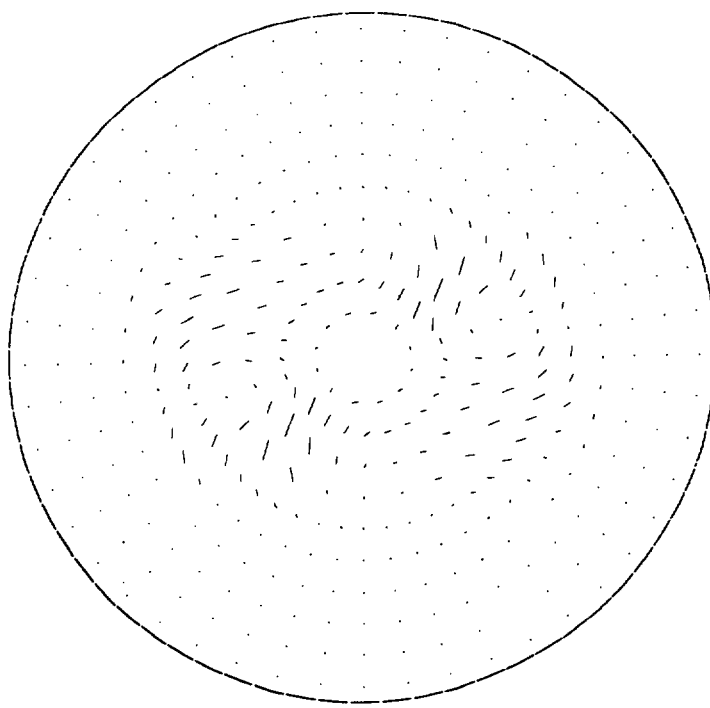

b
$t = 1.27 \times 10^5$ yrs

$(\rho u)_{min} = -2.63 \times 10^{-12}$

$(\rho v)_{min} = -1.13 \times 10^{-12}$

Momentum Density($g/cm^2 s$)
Rotating Frame
FIGURE 59

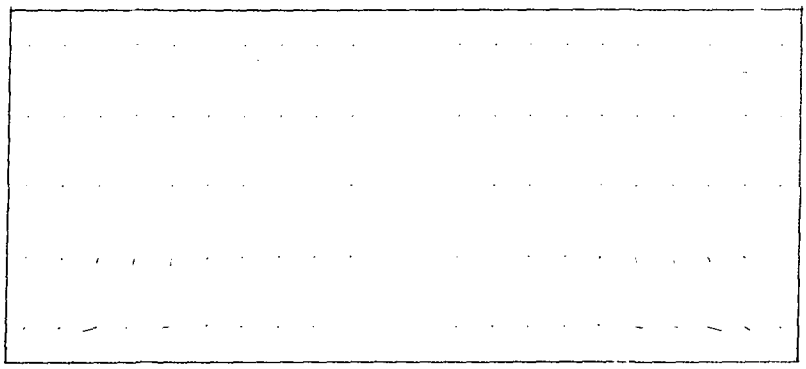

$(\rho u)_{max} = 9.00 \times 10^{-13}$ $(\rho w)_{min} = -3.15 \times 10^{-13}$

$t = 1.10 \times 10^{5}$ yrs
a

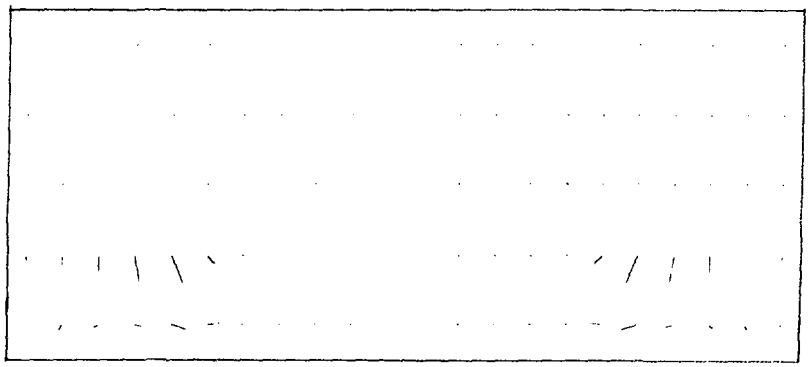

$(\rho u)_{min} = -3.92 \times 10^{-13}$ $(\rho w)_{min} = -3.62 \times 10^{-13}$

$t = 1.27 \times 10^{5}$ yrs
b

r-z Plane
Momentum Density(g/cm^2s)
FIGURE 60

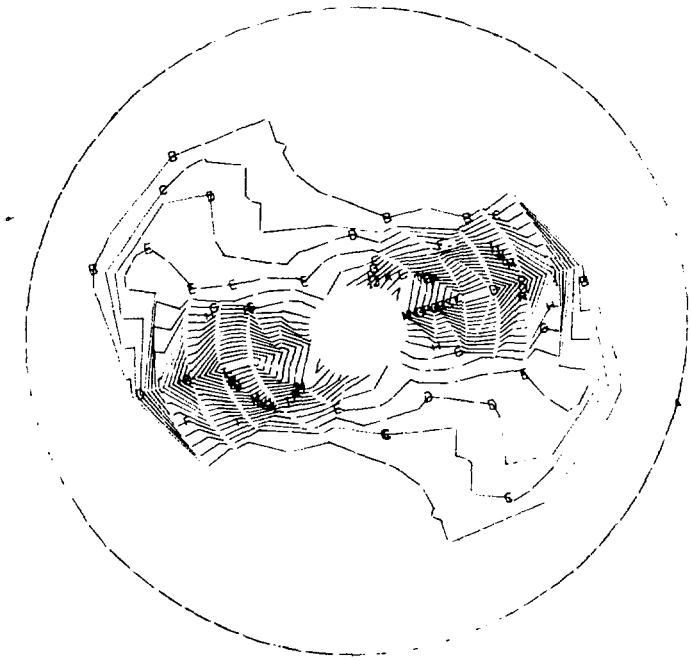

IDENTIFICATION	CONTOUR VALUE
A A A A	9.960E-27
B B B B	9.093E-18
C C C C	1.819E-17
D D D D	2.728E-17
E E E E	3.637E-17
F F F F	4.547E-17
G G G G	5.456E-17
H H H H	6.365E-17
I I I I	7.274E-17
J J J J	8.184E-17
K K K K	9.093E-17
L L L L	1.000E-16
M M M M	1.091E-16
N N N N	1.182E-16
O O O O	1.273E-16
P P P P	1.364E-16
Q Q Q Q	1.455E-16
R R R R	1.546E-16
S S S S	1.637E-16
T T T T	1.728E-16
U U U U	1.819E-16

r-θ Plane
a

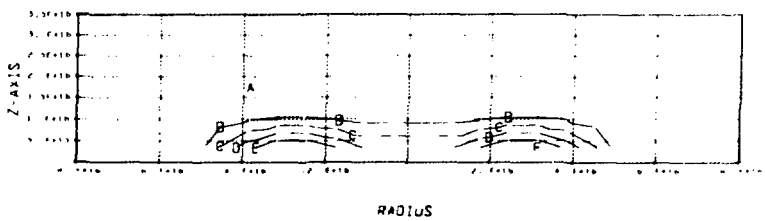

IDENTIFICATION	CONTOUR VALUE
A A A A	1.998E-32
B B B B	3.637E-17
C C C C	7.274E-17
D D D D	1.091E-16
E E E E	1.455E-16
F F F F	1.819E-16

r-z Plane
b

$t = 1.42 \times 10^5$ yrs

Density(g/cm^3)

FIGURE 61

IDENTIFICATION	CONTOUR VALUE
A	-1.889E+10
B	-1.820E+10
C	-1.751E+10
D	-1.683E+10
E	-1.614E+10
F	-1.546E+10
G	-1.477E+10
H	-1.409E+10
I	-1.340E+10
J	-1.271E+10
K	-1.203E+10
L	-1.134E+10
M	-1.066E+10
N	-9.972E+09
O	-9.286E+09
P	-8.601E+09
Q	-7.915E+09
R	-7.230E+09
S	-6.544E+09
T	-5.858E+09
U	-5.173E+09

r-θ Plane
a

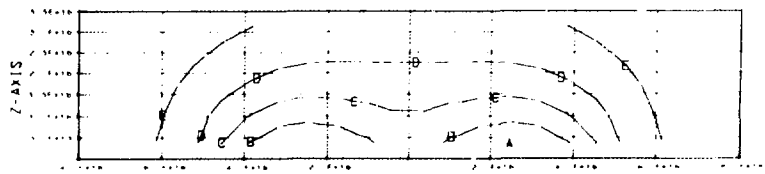

IDENTIFICATION	CONTOUR VALUE
A	-1.889E+10
B	-1.617E+10
C	-1.345E+10
D	-1.074E+10
E	-8.020E+09
F	-5.304E+09

r-z Plane
b

$t = 1.42 \times 10^5$ yrs
Gravitational Potential(ergs/g)
FIGURE 62

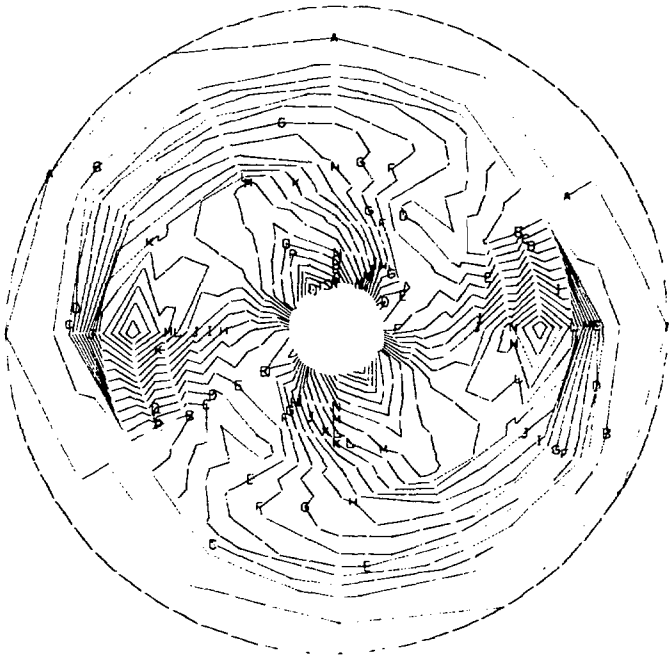

IDENTIFICATION	CONTOUR VALUE
A A A A	0.
B B B B	2.214E-13
C C C C	4.428E-13
D D D D	6.642E-13
E E E E	8.856E-13
F F F F	1.107E-12
G G G G	1.328E-12
H H H H	1.550E-12
I I I I	1.771E-12
J J J J	1.993E-12
K K K K	2.214E-12
L L L L	2.435E-12
M M M M	2.657E-12
N N N N	2.878E-12
O O O O	3.099E-12
P P P P	3.321E-12
Q Q Q Q	3.542E-12
R R R R	3.764E-12
S S S S	3.985E-12
T T T T	4.206E-12
U U U U	4.428E-12

r-θ Plane
a

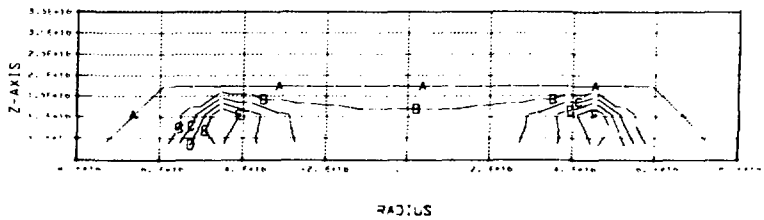

IDENTIFICATION	CONTOUR VALUE
A A A A	0.
B B B B	8.482E-13
C C C C	1.696E-12
D D D D	2.545E-12
E E E E	3.393E-12
F F F F	4.241E-12

r-z Plane
b

$t = 1.42 \times 10^5$ yrs
Angular Velocity(s^{-1})
FIGURE 63

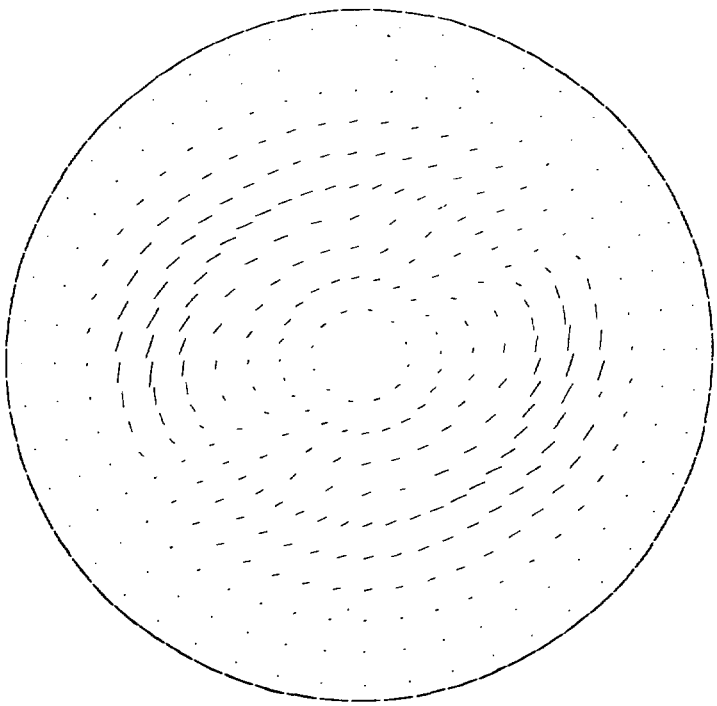

a
Velocity(cm/s)

$u_{min} = -5.46 \times 10^{4}$

$v_{max} = 1.29 \times 10^{5}$

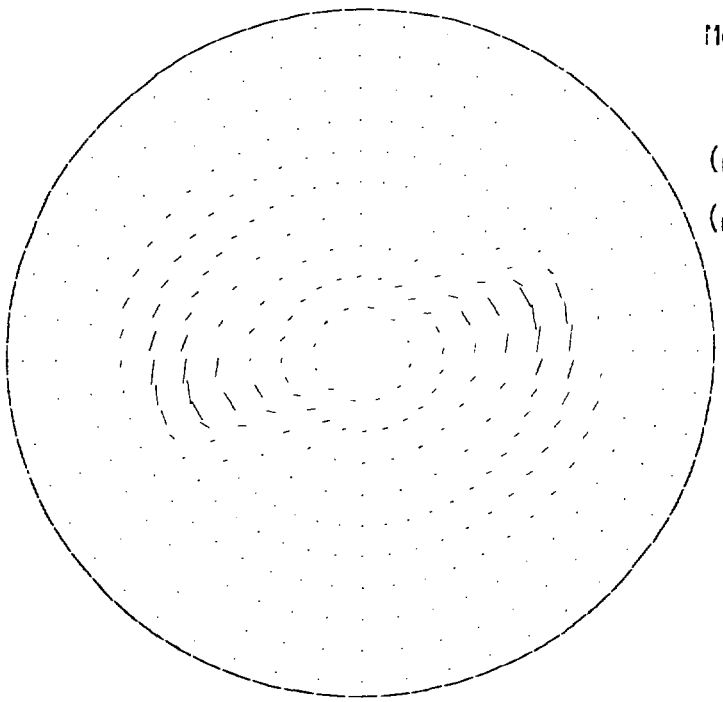

b
Momentum Density($g/cm^2 s$)

$(\rho u)_{min} = -3.03 \times 10^{-12}$

$(\rho v)_{max} = 7.67 \times 10^{-12}$

$t = 1.42 \times 10^{5}$ yrs
Laboratory Frame
FIGURE 64

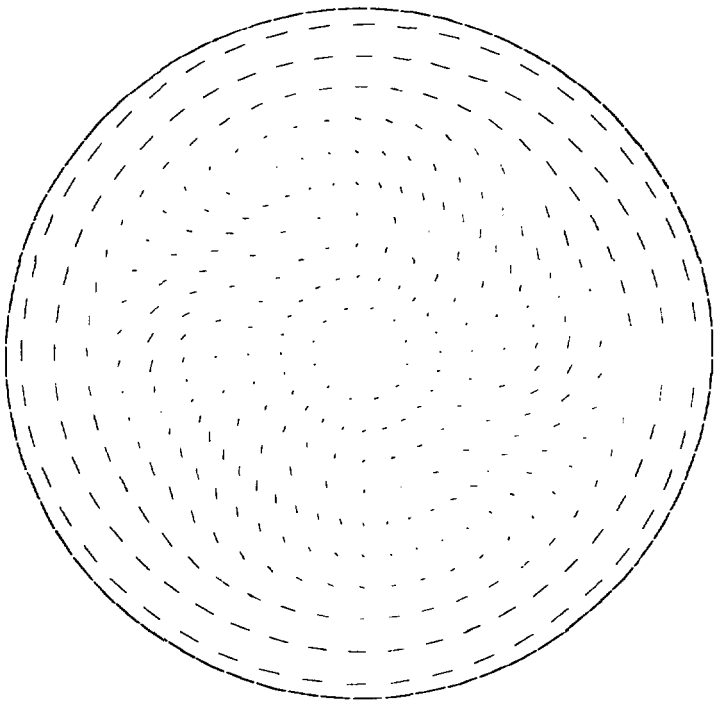

a
Rotating Frame

$u_{min} = -5.46 \times 10^4$

$v_{min} = -1.26 \times 10^5$

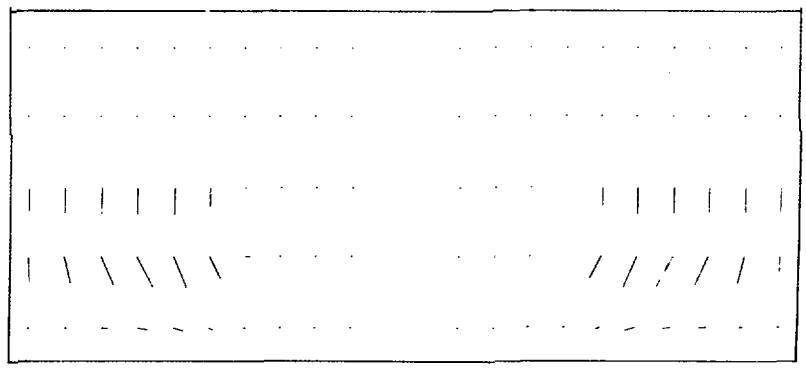

$u_{min} = -1.79 \times 10^4$ $\quad$ $w_{min} = -1.71 \times 10^4$

r-z Plane
b

$t = 1.42 \times 10^5$ yrs
Velocity(cm/s)
FIGURE 65

D. INTERMEDIATE RINGS

1. Case III

a. Initial conditions

The entropy variable for Case III is 8.25×10^{19}, as compared with 7.5×10^{19} in Case II. The ring has a characteristic cross-sectional radius of 1.74×10^{16} cm, approximately two and one-half computational zones. The contour of maximum density lies at a distance of 3.16×10^{16} cm from the axis of rotation. The other physical properties of the initial configuration are presented in Table III.

Figures 66 - 69 graphically summarize the initial conditions of the unperturbed system. The density contours in Fig. 66a, b illustrate the nature of the mass configuration. The original nonequilibrium toroid has expanded under the action of thermal pressures to such an extent that the inner edge has reached the central core of the calculational grid. The density in this region is a factor of 20 below maximum ring density; so the inner boundary wall has minimal effect on the subsequent evolution of the system. In Fig. 66b the r-z contours display a non-circular cross section.

From Fig. 67a, b one estimates that the depth of the gravitational potential well is less than those observed in Cases I and II by approximately 20 percent. The breadth of the Case III well is also greater and the gradients on the inner edge are more gradual. The picture presented is consistent with the density contours described above. The angular velocity contours of Fig. 68a, b show patterns of differential rotation that result because of the action of Coriolis forces working to increase the angular velocity of the gas that falls inward toward the axis of rotation and to decrease the angular velocity of

the gas that expands outward away from it.

With the laboratory velocity and momentum-density vector fields as a monitor of the orbital equilibrium of the fluid, Fig. 69a, b implies that the whole system is still moving slightly outward. It is therefore not in as precise an orbital equilibrium condition as the previous studies have been, but it is very close. Figure 69b demonstrates the greater spatial extent of this ring, showing significant momentum densities distributed over five radial zones.

Table III

Initial Conditions

Case III

$A(cm^4/g^{2/3}\ s^2)$	8.25×10^{19}	M(g)	5.91×10^{33}
a(cm)	1.74×10^{16}	W(ergs)	-3.63×10^{43}
$\rho'_{max}(g/cm^3)$	7.13×10^{-17}	KE(ergs)	1.12×10^{41}
$R_{\rho_{max}}$ (cm)	3.16×10^{16}	U(ergs)	8.98×10^{42}
$\rho_{max}(g/cm^3)$	7.13×10^{-17}	T(ergs)	9.84×10^{42}
$R_{\rho_{max}}$ (cm)	3.15×10^{16}	E(ergs)	-1.74×10^{43}
t_f(yrs)	0.08×10^{5}	J(g cm^2/s)	1.19×10^{55}
$\omega(s^{-1})$	1.64×10^{-12}	Θ(°K)	17.0

b. Intermediate fragmentation and higher modes

The intermediate stages of the growth of the perturbation are shown in Figs. 70 - 73. The time scale within which the dynamical processes proceed is lengthened as expected by the increased thermal pressures resisting fragmentation. At $t = 1.45 \times 10^5$ yrs the density contours of Fig. 70a show well-defined dual centers of attraction associated with large toroidal remnants on both the leading and the

trailing edges. By the time shown in Fig. 70b, t = 1.61 x 10^5 yrs, each element of this structure has itself fragmented to form a two-part system. The split configuration is only a transient intermediate state that returns to the binary structure, as shown at a later time in Fig. 74a. The split configuration is nevertheless significant because it appears at a fairly advanced time in a well-resolved physical system. Its appearance is the result of the nonlinear physical models rather th n of inaccuracies arising from coarse calculational zoning. The elongation of the centers of gravity in Fig. 71b indicates the response of the potential field to the quaternary configuration. The angular velocity contours in Fig. 72a, b show the characteristic pattern described previously in Section C.

In the rotating-frame momentum-density sequence of Fig. 73a, b, one again observes the development of co-rotational spin in the components. By comparing the configuration of the vectors in Fig. 73a and Fig. 73b, one has a graphic illustration of the time dependent transport of mass and momentum from the remnant regions at approximately 80° and 260° to the binary fragments.

c. Spirals

In Fig. 74a the density contours at t = 1.77 x 10^5 yrs show that a spiral structure has developed from the residual toroidal gas. The r-z contours in Fig. 74b indicate tidal bulging on the inner surfaces of the components similar to that observed for Case II. The gravitational potential contours in Fig. 75a, b are radially elongated, showing the response of the field to the density distribution.

The structure in the angular velocity contours discussed for Case II is present in Fig. 76a, albeit not so dramatically. The laboratory velocity and momentum-density vector fields are shown in Fig. 77a, b. In the velocity vector field the regions in the trailing spirals where accretion increases the already large orbital velocities of the toroidal remnant are clearly contrasted with the regions on the leading edge of the components where the gravitational attraction reduces the original orbital velocities of the residual gas. The momentum density representation indicates the location of the binary fragments and outlines the spiral structure of the system. The retrograde velocity vortices at 90° and 270°, respectively, in Fig. 78a are similar to the ones discussed for the Case II binary spirals. The spin of the components is shown at late time in Fig. 78b.

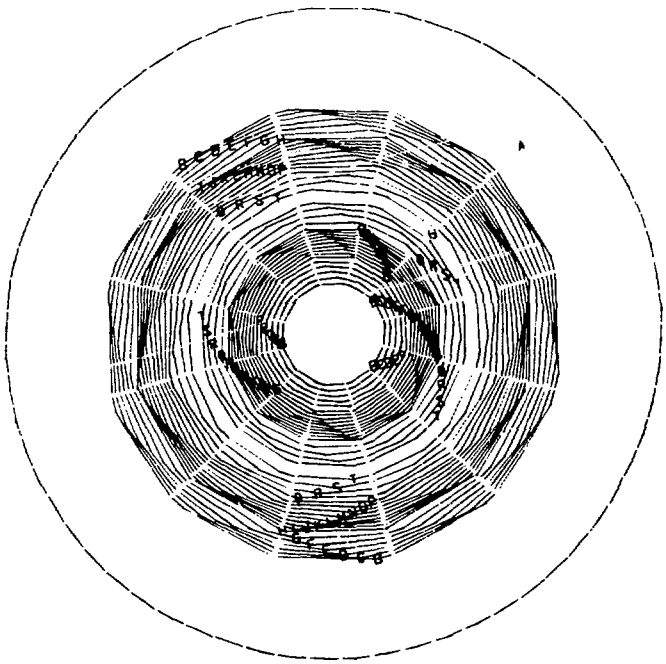

IDENTIFICATION	CONTOUR VALUE
A A A A	9.655E-29
B B B B	3.565E-18
C C C C	7.131E-18
D D D D	1.070E-17
E E E E	1.426E-17
F F F F	1.783E-17
G G G G	2.139E-17
H H H H	2.496E-17
I I I I	2.852E-17
J J J J	3.209E-17
K K K K	3.565E-17
L L L L	3.922E-17
M M M M	4.279E-17
N N N N	4.635E-17
O O O O	4.992E-17
P P P P	5.348E-17
Q Q Q Q	5.705E-17
R R R R	6.061E-17
S S S S	6.418E-17
T T T T	6.774E-17
U U U U	7.131E-17

r-θ Plane
a

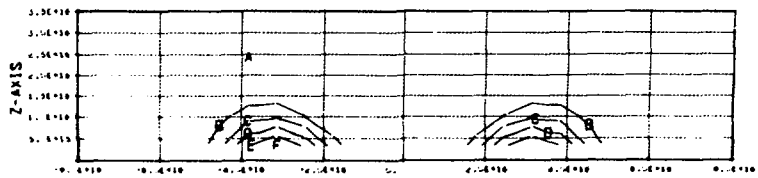

IDENTIFICATION	CONTOUR VALUE
A A A A	5.181E-30
B B B B	1.426E-17
C C C C	2.852E-17
D D D D	4.279E-17
E E E E	5.705E-17
F F F F	7.131E-17

r-z Plane
b

t = 0

Density(g/cm^3)

FIGURE 66

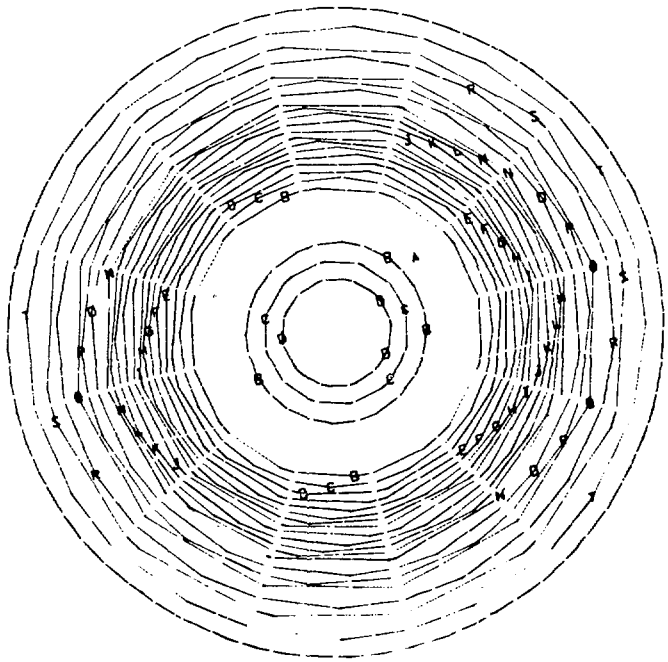

IDENTIFICATION	CONTOUR VALUE
A A A A	-1.368E+10
B B B B	-1.328E+10
C C C C	-1.288E+10
D D D D	-1.248E+10
E E E E	-1.208E+10
F F F F	-1.168E+10
G G G G	-1.128E+10
H H H H	-1.088E+10
I I I I	-1.048E+10
J J J J	-1.008E+10
K K K K	-9.683E+09
L L L L	-9.283E+09
M M M M	-8.883E+09
N N N N	-8.483E+09
O O O O	-8.082E+09
P P P P	-7.682E+09
Q Q Q Q	-7.282E+09
R R R R	-6.882E+09
S S S S	-6.482E+09
T T T T	-6.082E+09
U U U U	-5.682E+09

r-θ Plane
a

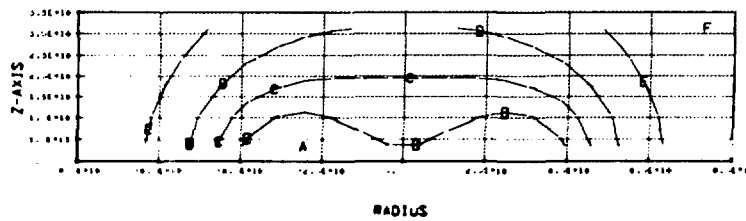

IDENTIFICATION	CONTOUR VALUE
A A A A	-1.368E+10
B B B B	-1.195E+10
C C C C	-1.022E+10
D D D D	-8.495E+09
E E E E	-6.765E+09
F F F F	-5.035E+09

r-z Plane
b

t = 0
Gravitational Potential(ergs/g)
FIGURE 67

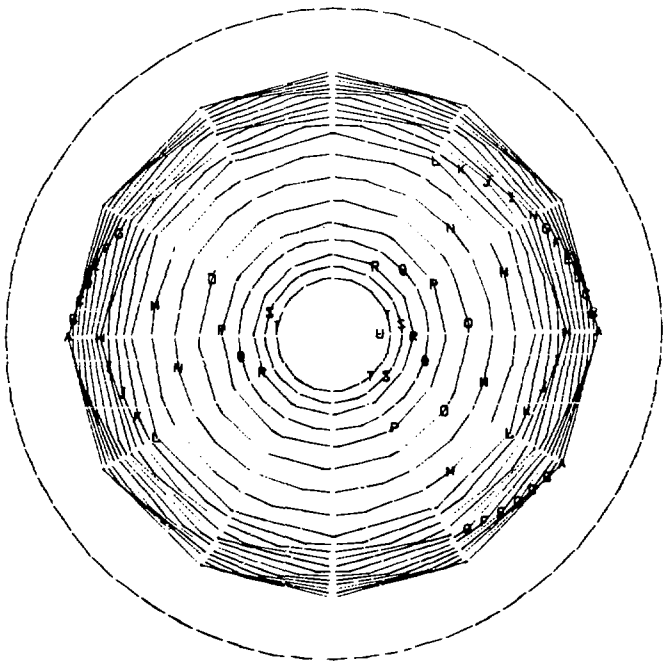

IDENTIFICATION	CONTOUR VALUE
A	0.
B	1.284E-13
C	2.568E-13
D	3.852E-13
E	5.135E-13
F	6.419E-13
G	7.703E-13
H	8.987E-13
I	1.027E-12
J	1.155E-12
K	1.284E-12
L	1.412E-12
M	1.541E-12
N	1.669E-12
O	1.797E-12
P	1.926E-12
Q	2.054E-12
R	2.183E-12
S	2.311E-12
T	2.439E-12
U	2.568E-12

r-θ Plane
a

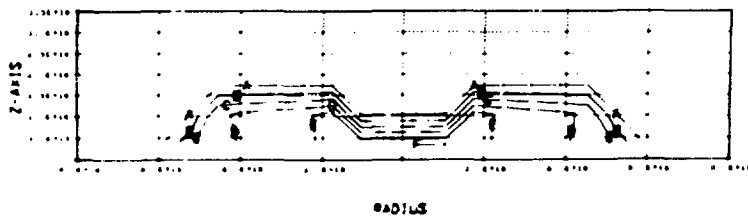

IDENTIFICATION	CONTOUR VALUE
A	0.
B	5.135E-13
C	1.027E-12
D	1.541E-12
E	2.054E-12
F	2.568E-12

r-z Plane
b

t = 0

Angular Velocity(s^{-1})

FIGURE 68

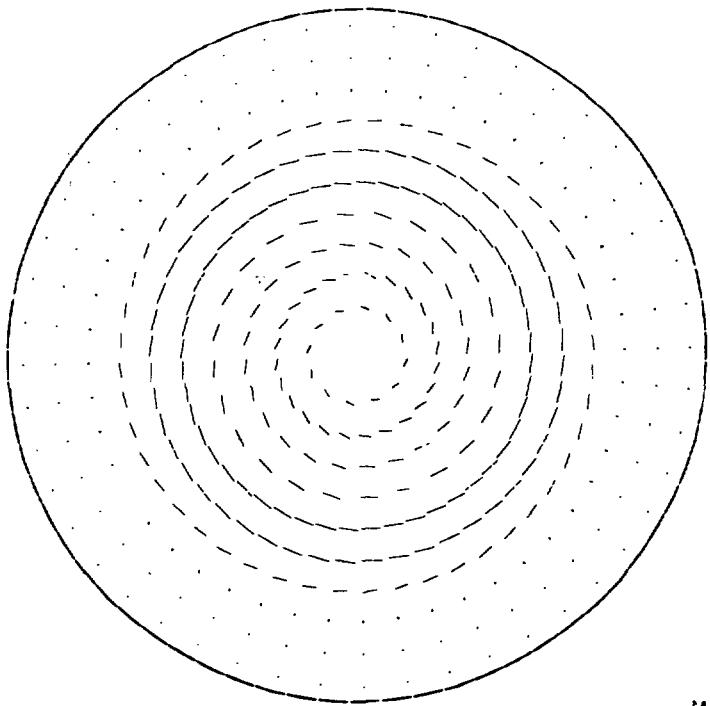

a
Velocity(cm/s)

$u_{max} = 9.46 \times 10^{3}$

$v_{max} = 6.46 \times 10^{4}$

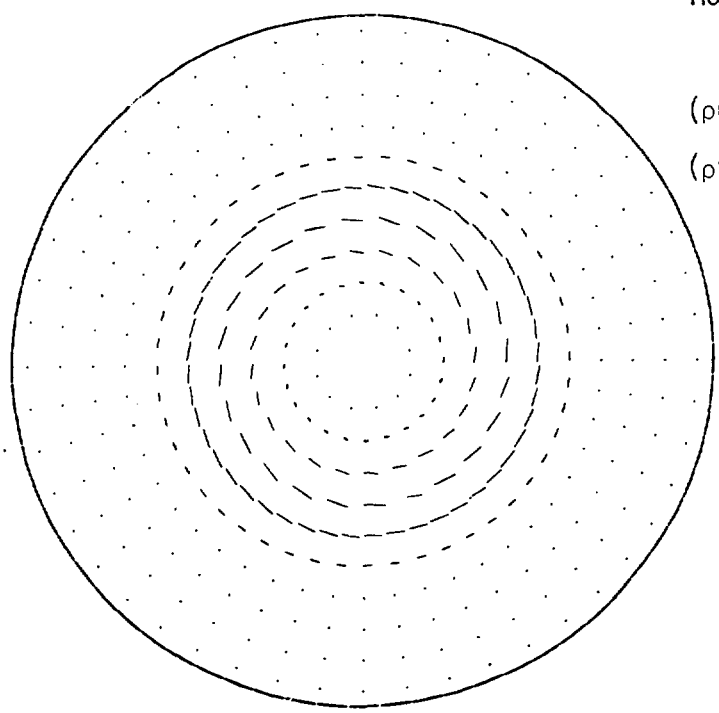

b
Momentum Density(g/cm^2s)

$(\rho u)_{max} = 3.26 \times 10^{-13}$

$(\rho v)_{max} = 3.98 \times 10^{-12}$

t = 0
Laboratory Frame
FIGURE 69

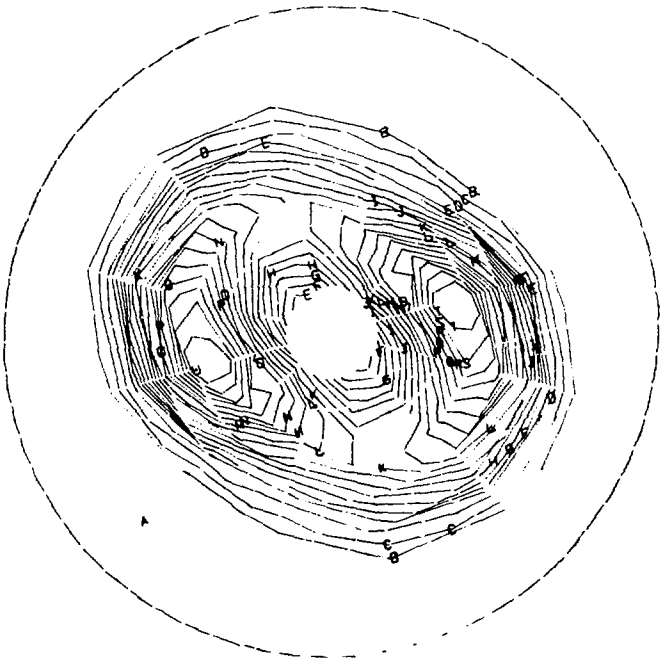

IDENTIFICATION	CONTOUR VALUE
A A A A	5.278E-32
B B B B	4.674E-18
C C C C	9.347E-18
D D D D	1.402E-17
E E E E	1.869E-17
F F F F	2.337E-17
G G G G	2.804E-17
H H H H	3.271E-17
I I I I	3.739E-17
J J J J	4.206E-17
K K K K	4.674E-17
L L L L	5.141E-17
M M M M	5.608E-17
N N N N	6.076E-17
O O O O	6.543E-17
P P P P	7.010E-17
Q Q Q Q	7.478E-17
R R R R	7.945E-17
S S S S	8.412E-17
T T T T	8.880E-17
U U U U	9.347E-17

$t = 1.45 \times 10^5$ yrs
a

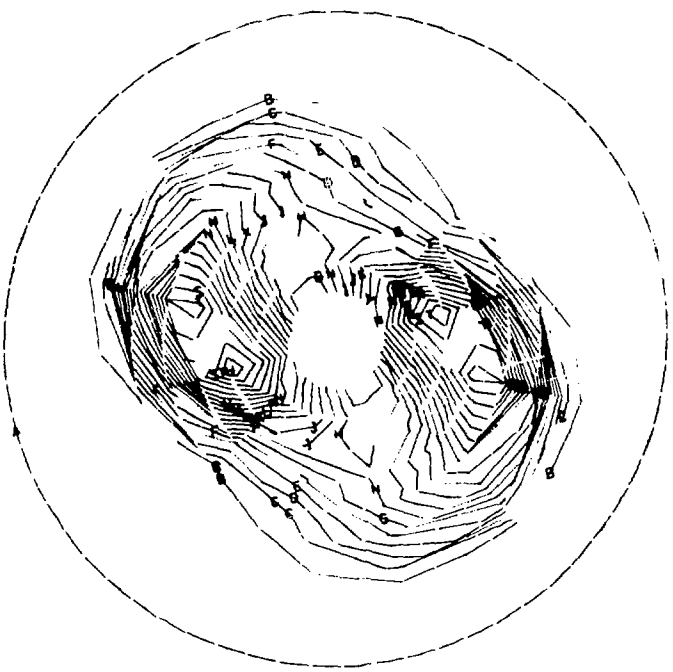

IDENTIFICATION	CONTOUR VALUE
A A A A	1.000E-26
B B B B	4.955E-18
C C C C	9.911E-18
D D D D	1.487E-17
E E E E	1.982E-17
F F F F	2.478E-17
G G G G	2.973E-17
H H H H	3.469E-17
I I I I	3.964E-17
J J J J	4.460E-17
K K K K	4.955E-17
L L L L	5.451E-17
M M M M	5.946E-17
N N N N	6.442E-17
O O O O	6.938E-17
P P P P	7.433E-17
Q Q Q Q	7.929E-17
R R R R	8.424E-17
S S S S	8.920E-17
T T T T	9.415E-17
U U U U	9.911E-17

$t = 1.61 \times 10^5$ yrs
b

Density(g/cm^3)
FIGURE 70

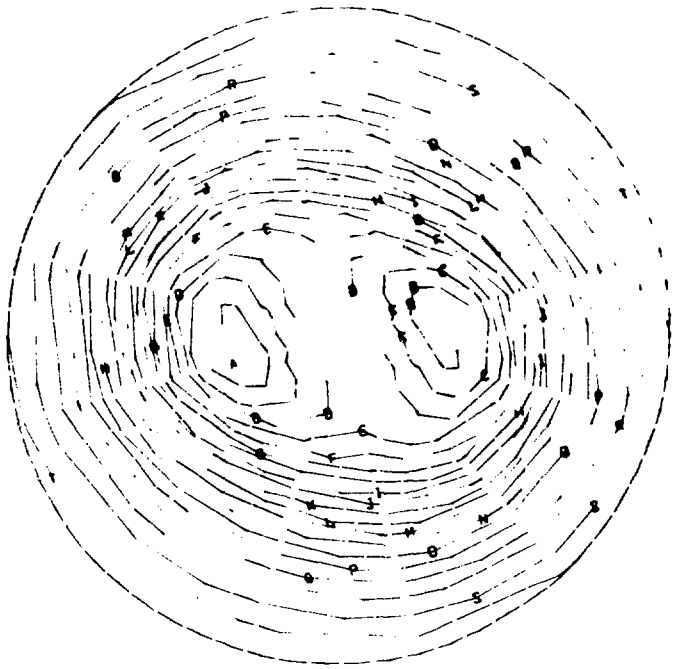

IDENTIFICATION	CONTOUR VALUE
A A A A	-1.556E+10
B B B B	-1.505E+10
C C C C	-1.454E+10
D D D D	-1.403E+10
E E E E	-1.352E+10
F F F F	-1.301E+10
G G G G	-1.250E+10
H H H H	-1.199E+10
I I I I	-1.148E+10
J J J J	-1.097E+10
K K K K	-1.046E+10
L L L L	-9.963E+09
M M M M	-9.443E+09
N N N N	-8.933E+09
O O O O	-8.423E+09
P P P P	-7.913E+09
Q Q Q Q	-7.403E+09
R R R R	-6.893E+09
S S S S	-6.383E+09
T T T T	-5.873E+09
U U U U	-5.363E+09

$t = 1.45 \times 10^5$ yrs

a

IDENTIFICATION	CONTOUR VALUE
A A A A	-1.576E+10
B B B B	-1.524E+10
C C C C	-1.471E+10
D D D D	-1.419E+10
E E E E	-1.367E+10
F F F F	-1.314E+10
G G G G	-1.262E+10
H H H H	-1.210E+10
I I I I	-1.157E+10
J J J J	-1.105E+10
K K K K	-1.053E+10
L L L L	-1.000E+10
M M M M	-9.482E+09
N N N N	-8.958E+09
O O O O	-8.435E+09
P P P P	-7.912E+09
Q Q Q Q	-7.389E+09
R R R R	-6.865E+09
S S S S	-6.342E+09
T T T T	-5.819E+09
U U U U	-5.296E+09

$t = 1.61 \times 10^5$ yrs

b

Gravitational Potential(ergs/g)

FIGURE 71

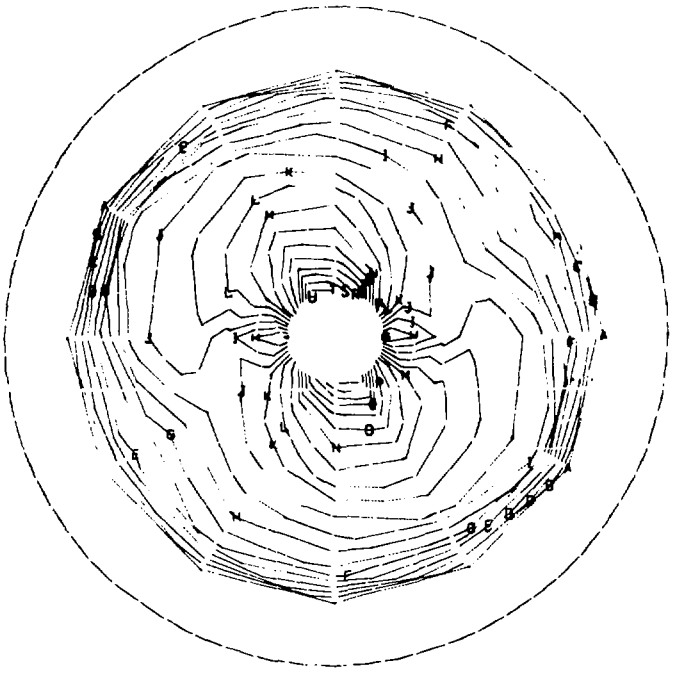

IDENTIFICATION	CONTOUR VALUE
A A A A	0.
B B B B	1.941E-13
C C C C	3.882E-13
D D D D	5.823E-13
E E E E	7.764E-13
F F F F	9.705E-13
G G G G	1.165E-12
H H H H	1.359E-12
I I I I	1.553E-12
J J J J	1.747E-12
K K K K	1.941E-12
L L L L	2.135E-12
M M M M	2.329E-12
N N N N	2.523E-12
O O O O	2.717E-12
P P P P	2.912E-12
Q Q Q Q	3.106E-12
R R R R	3.300E-12
S S S S	3.494E-12
T T T T	3.688E-12
U U U U	3.882E-12

$t = 1.45 \times 10^5$ yrs

a

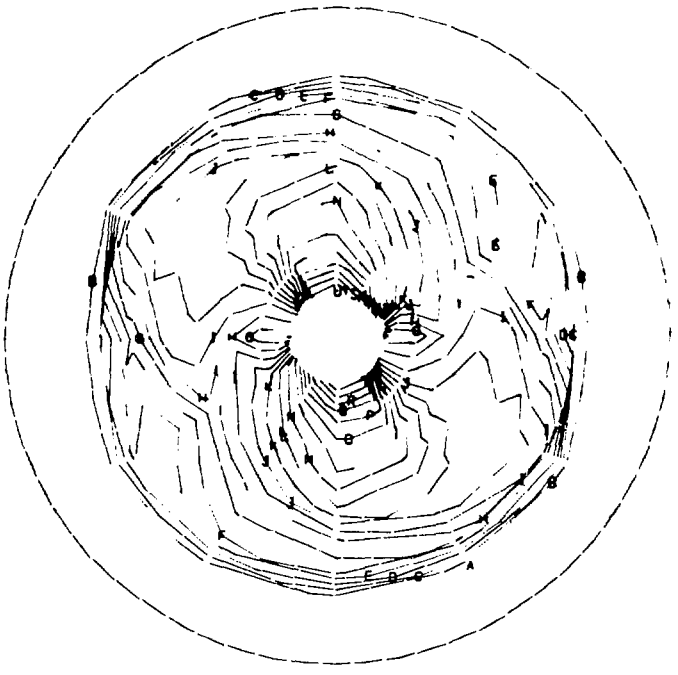

IDENTIFICATION	CONTOUR VALUE
A A A A	-2.886E-16
B B B B	2.018E-13
C C C C	4.040E-13
D D D D	6.061E-13
E E E E	8.083E-13
F F F F	1.010E-12
G G G G	1.213E-12
H H H H	1.415E-12
I I I I	1.617E-12
J J J J	1.819E-12
K K K K	2.021E-12
L L L L	2.223E-12
M M M M	2.426E-12
N N N N	2.628E-12
O O O O	2.830E-12
P P P P	3.032E-12
Q Q Q Q	3.234E-12
R R R R	3.436E-12
S S S S	3.638E-12
T T T T	3.840E-12
U U U U	4.042E-12

$t = 1.61 \times 10^5$ yrs

b

Angular Velocity(s^{-1})

FIGURE 72

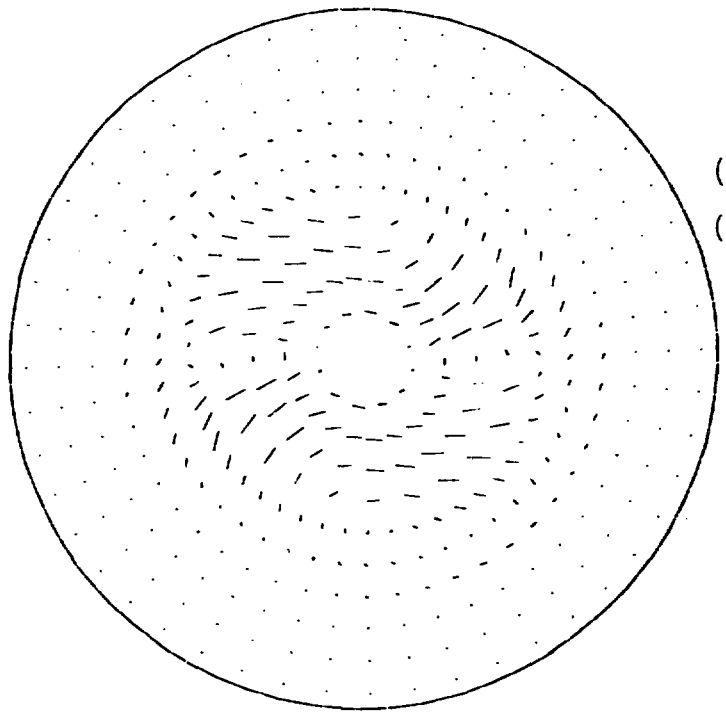

a
$t = 1.45 \times 10^5$ yrs

$(\rho u)_{min} = -9.99 \times 10^{-13}$

$(\rho v)_{max} = 8.92 \times 10^{-13}$

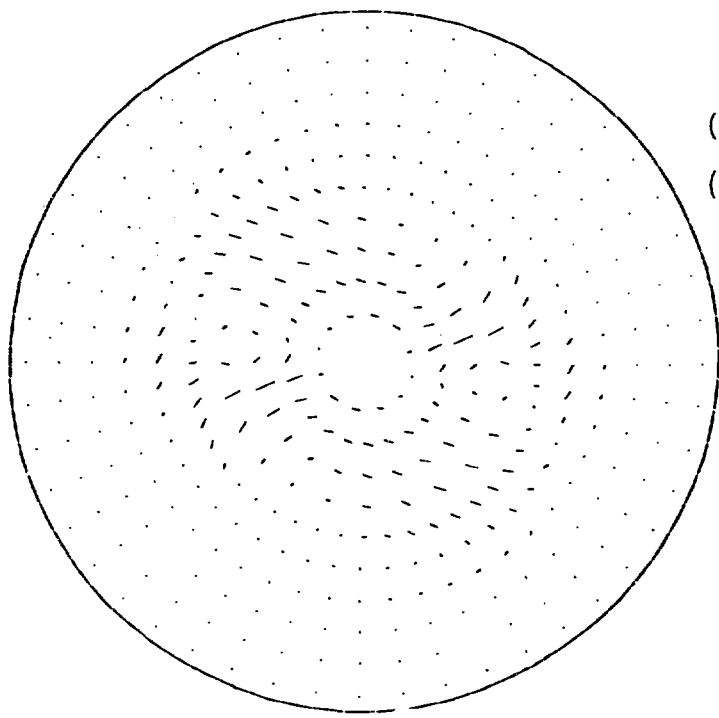

b
$t = 1.61 \times 10^5$ yrs

$(\rho u)_{min} = -2.02 \times 10^{-12}$

$(\rho v)_{max} = 9.42 \times 10^{-13}$

Momentum Density(g/cm^2s)
Rotating Frame
FIGURE 73

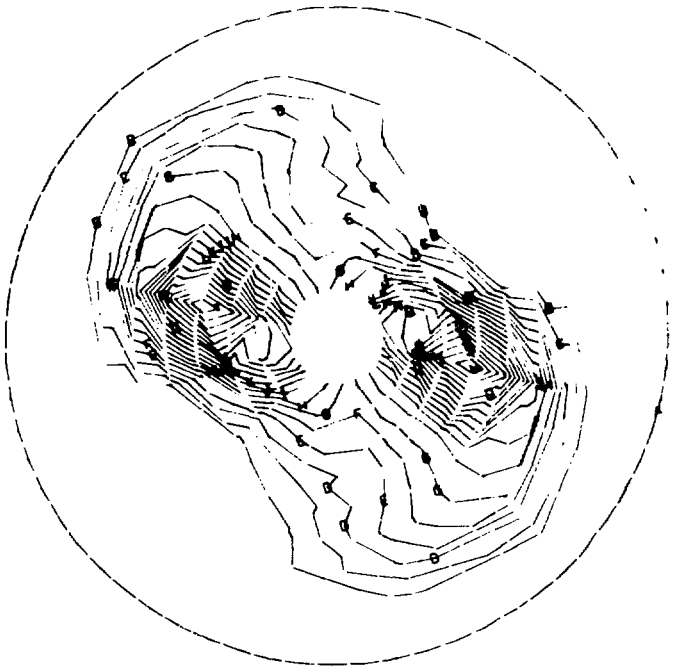

IDENTIFICATION	CONTOUR VALUE
A	1.010E-26
B	6.362E-18
C	1.272E-17
D	1.909E-17
E	2.545E-17
F	3.181E-17
G	3.817E-17
H	4.454E-17
I	5.090E-17
J	5.726E-17
K	6.362E-17
L	6.999E-17
M	7.635E-17
N	8.271E-17
O	8.907E-17
P	9.544E-17
Q	1.018E-16
R	1.082E-16
S	1.145E-16
T	1.209E-16
U	1.272E-16

r-θ Plane
a

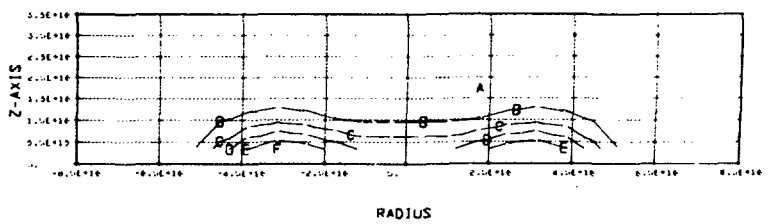

IDENTIFICATION	CONTOUR VALUE
A	7.591E-32
B	2.545E-17
C	5.090E-17
D	7.635E-17
E	1.018E-16
F	1.272E-16

r-z Plane
b

$t = 1.77 \times 10^5$ yrs
Density(g/cm^3)
FIGURE 74

IDENTIFICATION	CONTOUR VALUE
A A A A	-1.674E+10
B B B B	-1.616E+10
C C C C	-1.558E+10
D D D D	-1.501E+10
E E E E	-1.443E+10
F F F F	-1.385E+10
G G G G	-1.327E+10
H H H H	-1.269E+10
I I I I	-1.211E+10
J J J J	-1.153E+10
K K K K	-1.096E+10
L L L L	-1.038E+10
M M M M	-9.799E+09
N N N N	-9.221E+09
O O O O	-8.642E+09
P P P P	-8.064E+09
Q Q Q Q	-7.485E+09
R R R R	-6.907E+09
S S S S	-6.328E+09
T T T T	-5.750E+09
U U U U	-5.172E+09

r-θ Plane
a

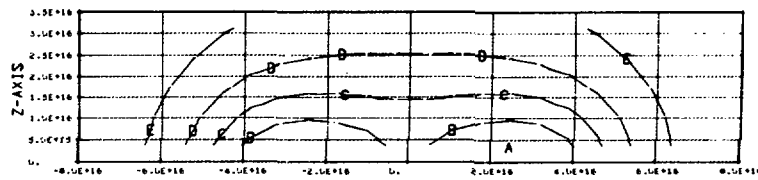

IDENTIFICATION	CONTOUR VALUE
A A A A	-1.674E+10
B B B B	-1.445E+10
C C C C	-1.216E+10
D D D D	-9.868E+09
E E E E	-7.577E+09
F F F F	-5.286E+09

r-z Plane
b

$t = 1.77 \times 10^5$ yrs
Gravitational Potential(ergs/g)
FIGURE 75

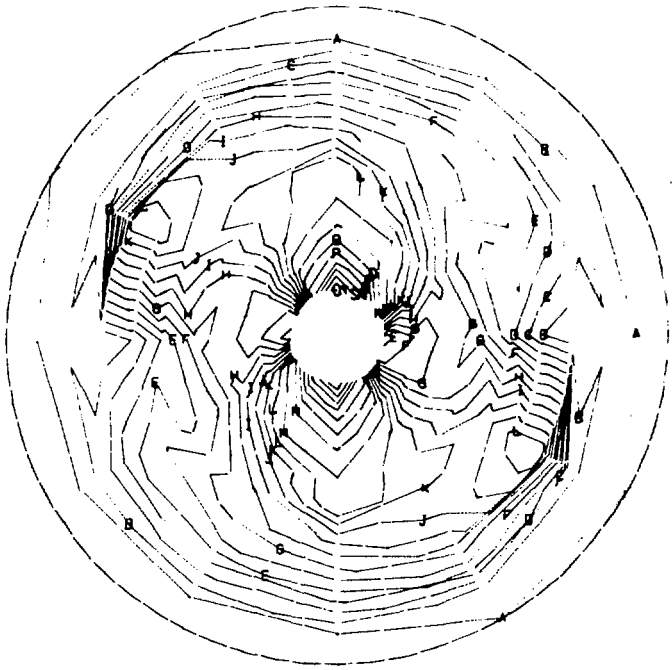

IDENTIFICATION	CONTOUR VALUE
A—A—A—A	0.
B—B—B—B	2.112E-13
C—C—C—C	4.225E-13
D—D—D—D	6.337E-13
E—E—E—E	8.449E-13
F—F—F—F	1.056E-12
G—G—G—G	1.267E-12
H—H—H—H	1.479E-12
I—I—I—I	1.690E-12
J—J—J—J	1.901E-12
K—K—K—K	2.112E-12
L—L—L—L	2.324E-12
M—M—M—M	2.535E-12
N—N—N—N	2.746E-12
O—O—O—O	2.967E-12
P—P—P—P	3.168E-12
Q—Q—Q—Q	3.380E-12
R—R—R—R	3.591E-12
S—S—S—S	3.802E-12
T—T—T—T	4.013E-12
U—U—U—U	4.225E-12

r-θ Plane
a

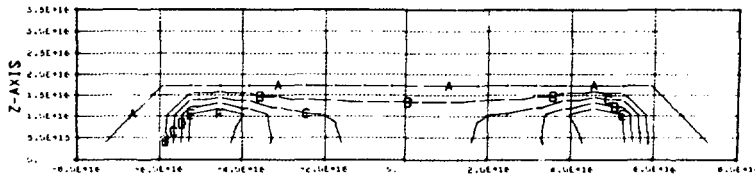

IDENTIFICATION	CONTOUR VALUE
A—A—A—A	0.
B—B—B—B	5.700E-13
C—C—C—C	1.140E-12
D—D—D—D	1.710E-12
E—E—E—E	2.280E-12
F—F—F—F	2.850E-12

r-z Plane
b

$t = 1.77 \times 10^5$ yrs
Angular Velocity(s^{-1})
FIGURE 76

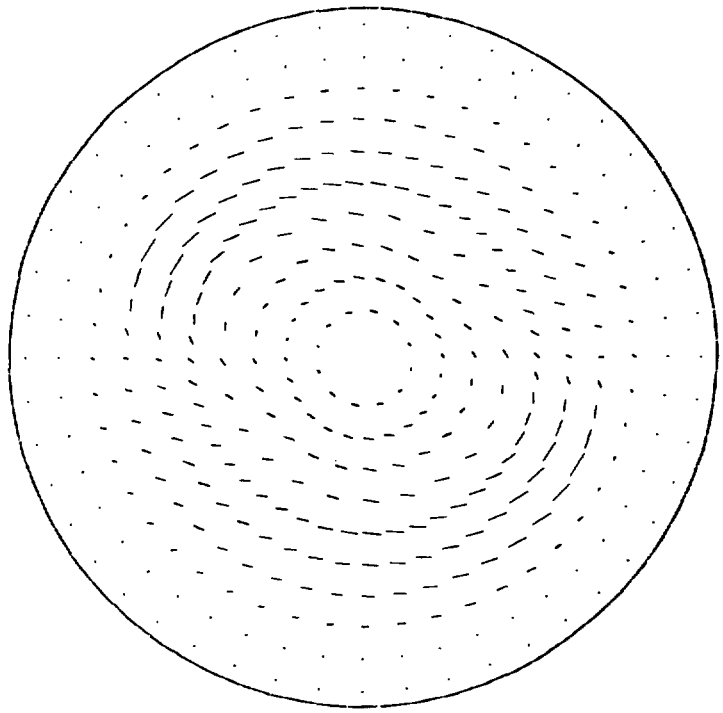

a
Velocity(cm/s)

$u_{min} = -4.78 \times 10^{4}$

$v_{max} = 1.07 \times 10^{5}$

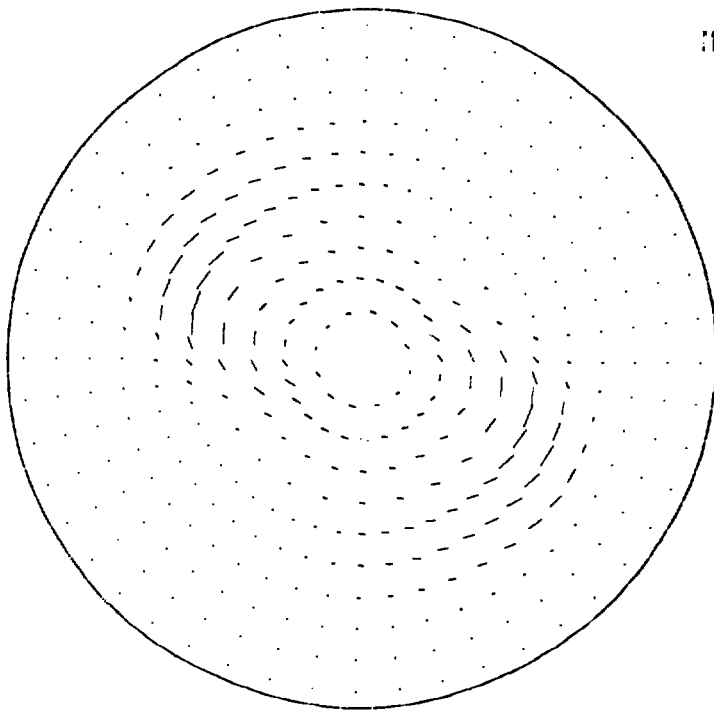

b
Momentum Density($g/cm^2 s$)

$(\rho u)_{min} = -2.19 \times 10^{-12}$

$(\rho v)_{max} = 5.63 \times 10^{-12}$

$t = 1.77 \times 10^{5}$ yrs
Laboratory Frame
FIGURE 77

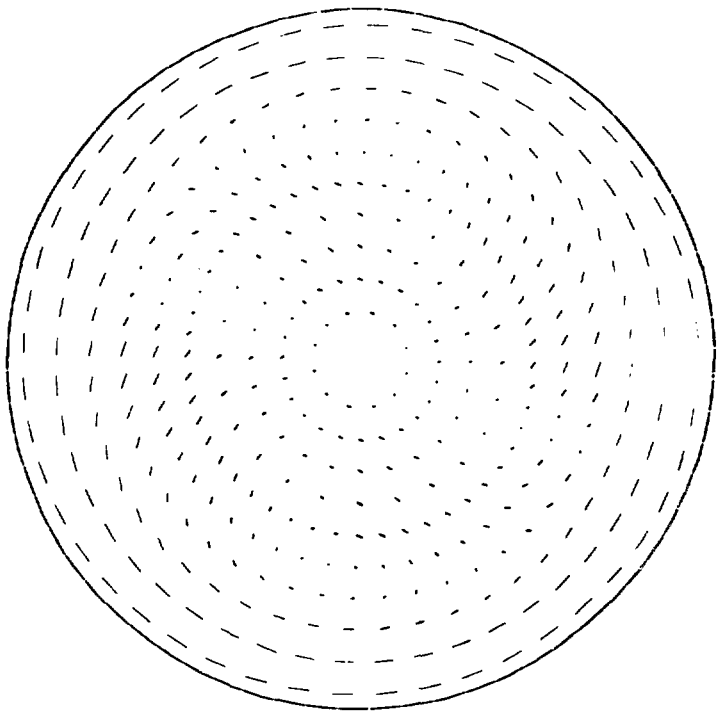

a
Velocity(cm/s)

$u_{min} = -4.78 \times 10^{4}$

$v_{min} = -1.16 \times 10^{5}$

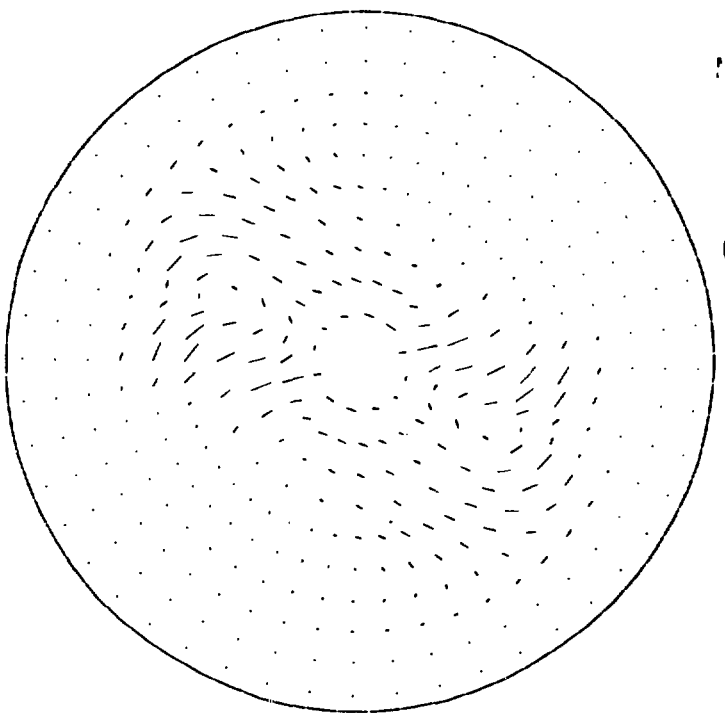

b
Momentum Density(g/cm^2s)

$(\rho u)_{min} = -2.19 \times 10^{-12}$

$(\rho v)_{max} = 1.21 \times 10^{-12}$

$t = 1.77 \times 10^{5}$ yrs
Rotating Frame
FIGURE 78

2. Case IV

a. Initial conditions

The entropy variable for Case IV has a value of 9.0×10^{19}. The characteristic cross-sectional radius of the ring is 1.80×10^{16} cm, and the maximum density contour is located at a distance of 3.01×10^{16} cm from the axis of rotation. Other relevant system parameters summarizing the initial conditions are listed in Table IV.

The graphic representations of the properties of the Case IV ring are presented in Figs. 79 - 82. The system is qualitatively similar to that of Case III.

Table IV

Initial Conditions

Case IV

$A(cm^4/g^{2/3}\ s^2)$	9.00×10^{19}	M(g)	5.91×10^{33}
a(cm)	1.80×10^{16}	W(ergs)	-3.68×10^{43}
$\rho'_{max}(g/cm^3)$	6.70×10^{-17}	KE(ergs)	1.17×10^{41}
$R_{\rho'_{max}}$ (cm)	3.01×10^{16}	U(ergs)	9.41×10^{42}
$\rho_{max}(g/cm^3)$	6.65×10^{-17}	T(ergs)	1.06×10^{43}
$R_{\rho_{max}}$ (cm)	3.15×10^{16}	E(ergs)	-1.66×10^{43}
t_f(yrs)	0.08×10^{5}	J(g cm^2/s)	1.19×10^{55}
$\omega(s^{-1})$	1.75×10^{-12}	$\Theta(°K)$	17.7

b. Evolution of the system

The qualitative features of the evolution of this system under a mode 2 perturbation are very similar to those described in the Case III discussion. The dynamical time scale is not significantly longer for Case IV. The free-fall time estimate for both cases is approximately 0.08×10^5 yrs. The contour plots and vector fields summarizing the evolution of the Case IV system are presented in Figs. 83 - 92. The Case IV toroid is the only system that has been subjected to mode 2, mode 3, and mode 6 perturbations, as will be discussed in a subsequent section.

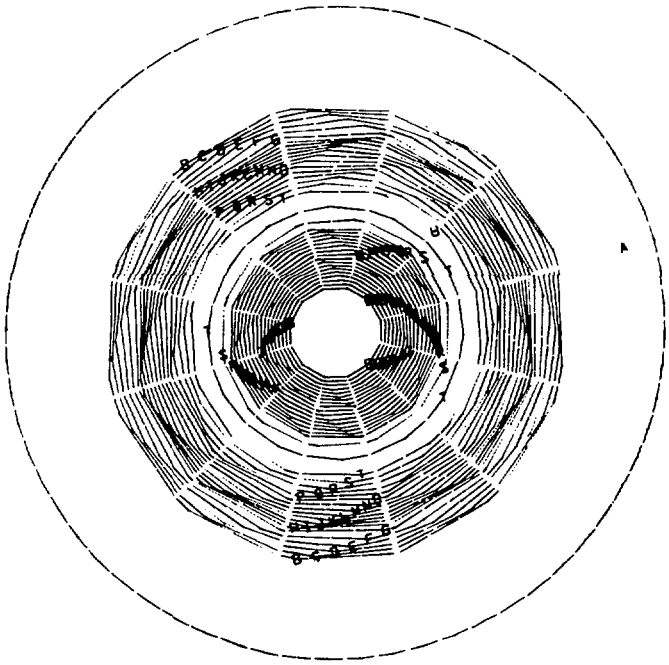

IDENTIFICATION	CONTOUR VALUE
A—A—A—A	2.149E-30
B—B—B—B	3.326E-18
C—C—C—C	6.652E-18
D—D—D—D	9.979E-18
E—E—E—E	1.330E-17
F—F—F—F	1.663E-17
G—G—G—G	1.996E-17
H—H—H—H	2.328E-17
I—I—I—I	2.661E-17
J—J—J—J	2.994E-17
K—K—K—K	3.326E-17
L—L—L—L	3.659E-17
M—M—M—M	3.991E-17
N—N—N—N	4.324E-17
O—O—O—O	4.657E-17
P—P—P—P	4.989E-17
Q—Q—Q—Q	5.322E-17
R—R—R—R	5.655E-17
S—S—S—S	5.987E-17
T—T—T—T	6.320E-17
U—U—U—U	6.652E-17

r-θ Plane
a

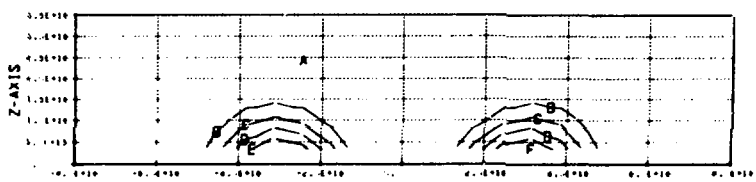

IDENTIFICATION	CONTOUR VALUE
A—A—A—A	1.081E-31
B—B—B—B	1.330E-17
C—C—C—C	2.661E-17
D—D—D—D	3.991E-17
E—E—E—E	5.322E-17
F—F—F—F	6.652E-17

r-z Plane
b

t = 0
Density(g/cm^3)
FIGURE 79

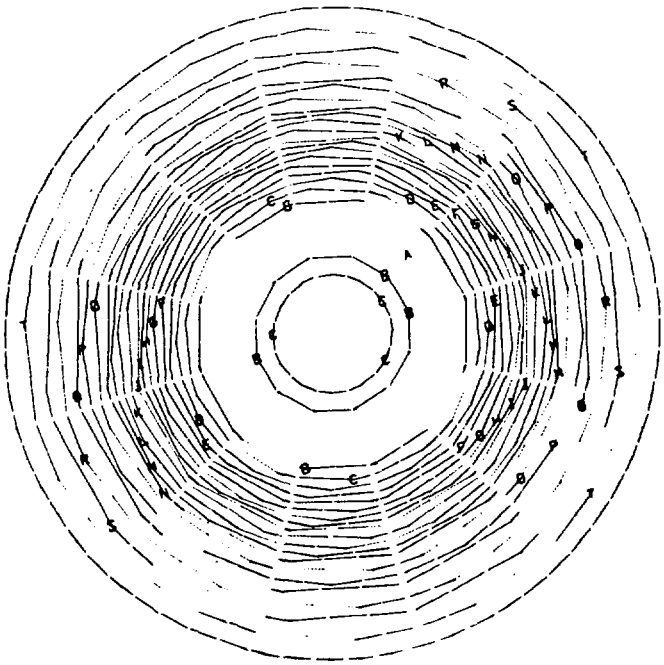

IDENTIFICATION	CONTOUR VALUE
A A A A	-1.408E+10
B B B B	-1.366E+10
C C C C	-1.323E+10
D D D D	-1.281E+10
E E E E	-1.239E+10
F F F F	-1.197E+10
G G G G	-1.155E+10
H H H H	-1.113E+10
I I I I	-1.071E+10
J J J J	-1.029E+10
K K K K	-9.865E+09
L L L L	-9.444E+09
M M M M	-9.023E+09
N N N N	-8.602E+09
O O O O	-8.181E+09
P P P P	-7.760E+09
Q Q Q Q	-7.339E+09
R R R R	-6.918E+09
S S S S	-6.496E+09
T T T T	-6.075E+09
U U U U	-5.654E+09

r-θ Plane
a

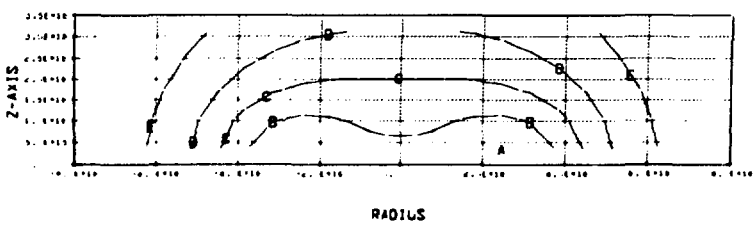

IDENTIFICATION	CONTOUR VALUE
A A A A	-1.408E+10
B B B B	-1.227E+10
C C C C	-1.046E+10
D D D D	-8.647E+09
E E E E	-6.837E+09
F F F F	-5.028E+09

r-z Plane
b

t = 0
Gravitational Potential(ergs/g)
FIGURE 80

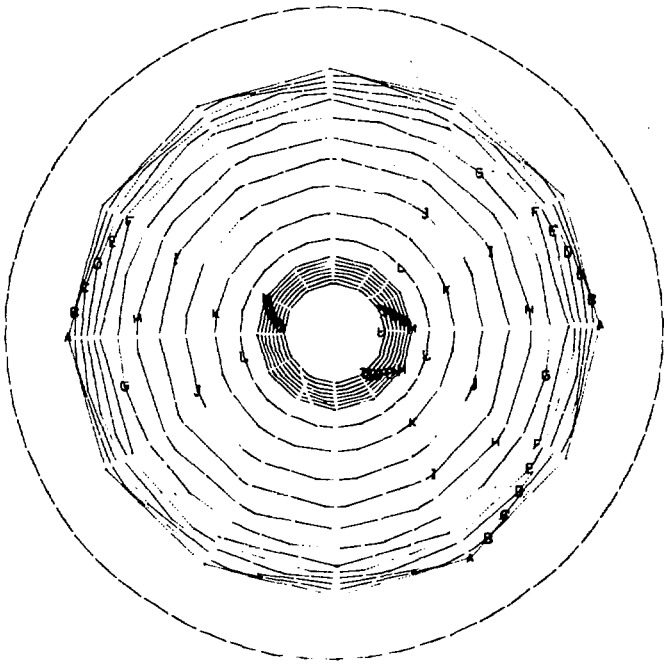

IDENTIFICATION	CONTOUR VALUE
A A A A	0.
B B B B	2.082E-13
C C C C	4.163E-13
D D D D	6.245E-13
E E E E	8.326E-13
F F F F	1.041E-12
G G G G	1.249E-12
H H H H	1.457E-12
I I I I	1.665E-12
J J J J	1.873E-12
K K K K	2.082E-12
L L L L	2.290E-12
M M M M	2.498E-12
N N N N	2.706E-12
O O O O	2.914E-12
P P P P	3.122E-12
Q Q Q Q	3.330E-12
R R R R	3.539E-12
S S S S	3.747E-12
T T T T	3.955E-12
U U U U	4.163E-12

r-θ Plane
a

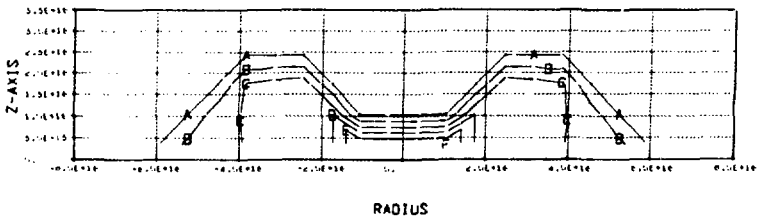

IDENTIFICATION	CONTOUR VALUE
A A A A	0.
B B B B	8.326E-13
C C C C	1.665E-12
D D D D	2.498E-12
E E E E	3.330E-12
F F F F	4.163E-12

r-z Plane
b

t = 0

Angular Velocity(s^{-1})

FIGURE 81

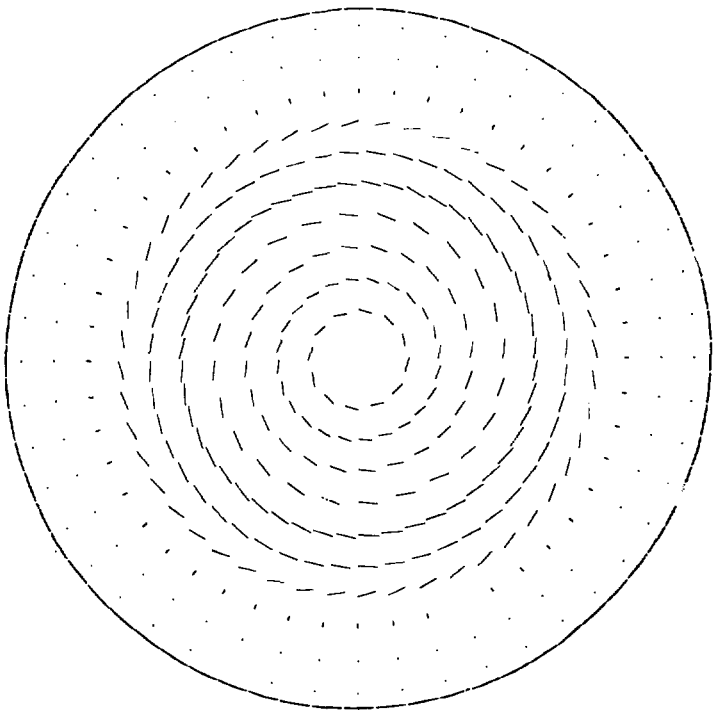

a
Velocity(cm/s)

$u_{min} = -1.55 \times 10^{4}$

$v_{max} = 6.55 \times 10^{4}$

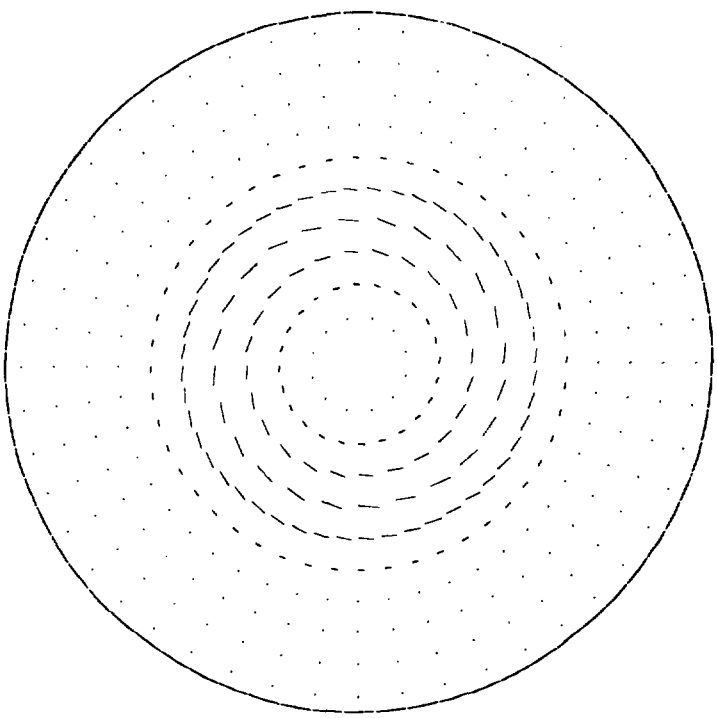

b
Momentum Density(g/cm^2s)

$(\rho u)_{max} = 3.99 \times 10^{-13}$

$(\rho v)_{max} = 4.06 \times 10^{-12}$

t = 0
Laboratory Frame
FIGURE 82

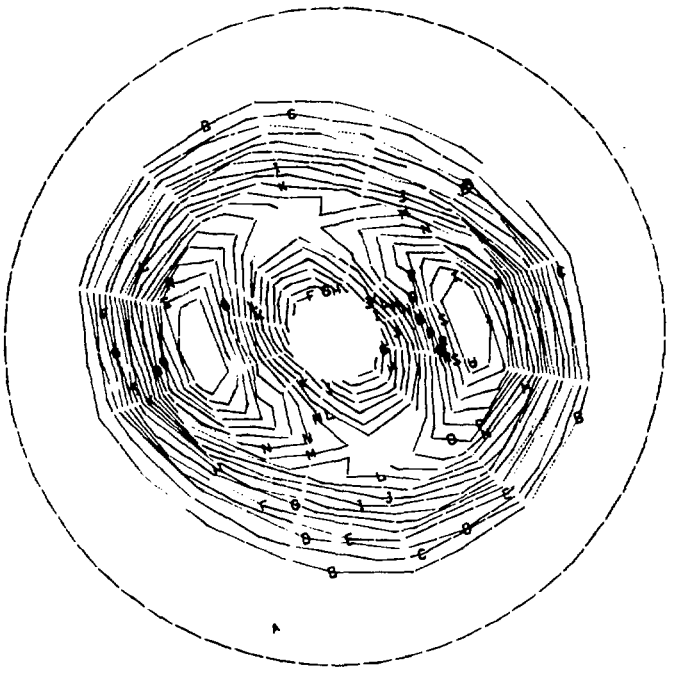

IDENTIFICATION	CONTOUR VALUE
A—A—A—A	2.124E-30
B—B—B—B	3.575E-18
C—C—C—C	7.149E-18
D—D—D—D	1.072E-17
E—E—E—E	1.430E-17
F—F—F—F	1.787E-17
G—G—G—G	2.145E-17
H—H—H—H	2.502E-17
I—I—I—I	2.860E-17
J—J—J—J	3.217E-17
K—K—K—K	3.575E-17
L—L—L—L	3.932E-17
M—M—M—M	4.289E-17
N—N—N—N	4.647E-17
O—O—O—O	6.004E-17
P—P—P—P	5.362E-17
Q—Q—Q—Q	5.719E-17
R—R—R—R	6.077E-17
S—S—S—S	6.434E-17
T—T—T—T	6.792E-17
U—U—U—U	7.149E-17

$t = 1.48 \times 10^5$ yrs
a

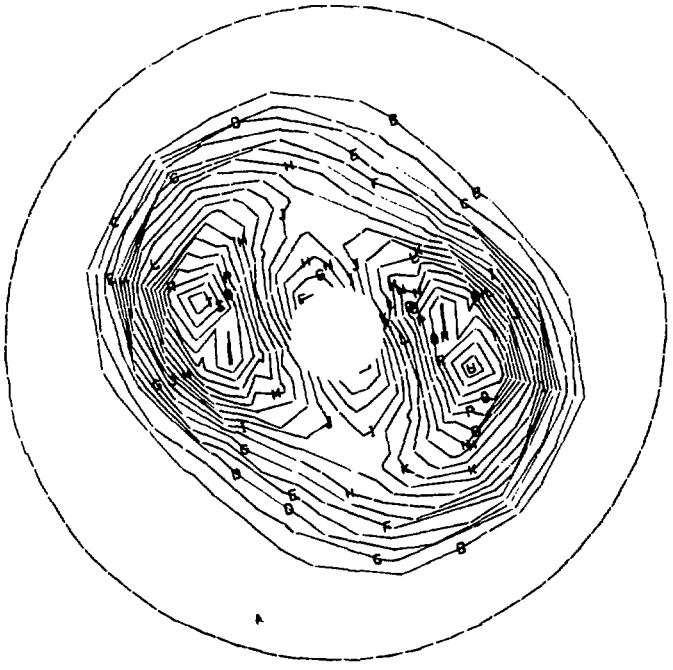

IDENTIFICATION	CONTOUR VALUE
A—A—A—A	2.120E-30
B—B—B—B	4.469E-18
C—C—C—C	8.938E-18
D—D—D—D	1.341E-17
E—E—E—E	1.788E-17
F—F—F—F	2.235E-17
G—G—G—G	2.682E-17
H—H—H—H	3.128E-17
I—I—I—I	3.575E-17
J—J—J—J	4.022E-17
K—K—K—K	4.469E-17
L—L—L—L	4.916E-17
M—M—M—M	5.363E-17
N—N—N—N	5.810E-17
O—O—O—O	6.257E-17
P—P—P—P	6.704E-17
Q—Q—Q—Q	7.151E-17
R—R—R—R	7.598E-17
S—S—S—S	8.045E-17
T—T—T—T	8.491E-17
U—U—U—U	8.938E-17

$t = 1.64 \times 10^5$ yrs
b

Density(g/cm^3)
FIGURE 83

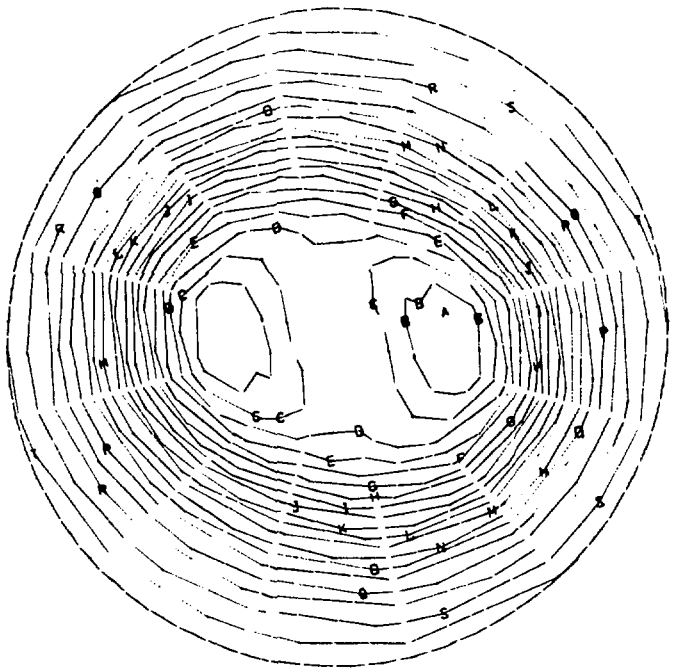

IDENTIFICATION	CONTOUR VALUE
A A A A	-1.448E+10
B B B B	-1.403E+10
C C C C	-1.358E+10
D D D D	-1.312E+10
E E E E	-1.267E+10
F F F F	-1.222E+10
G G G G	-1.176E+10
H H H H	-1.131E+10
I I I I	-1.086E+10
J J J J	-1.040E+10
K K K K	-9.950E+09
L L L L	-9.497E+09
M M M M	-9.043E+09
N N N N	-8.590E+09
O O O O	-8.137E+09
P P P P	-7.684E+09
Q Q Q Q	-7.231E+09
R R R R	-6.778E+09
S S S S	-6.324E+09
T T T T	-5.871E+09
U U U U	-5.418E+09

$t = 1.48 \times 10^5$ yrs
a

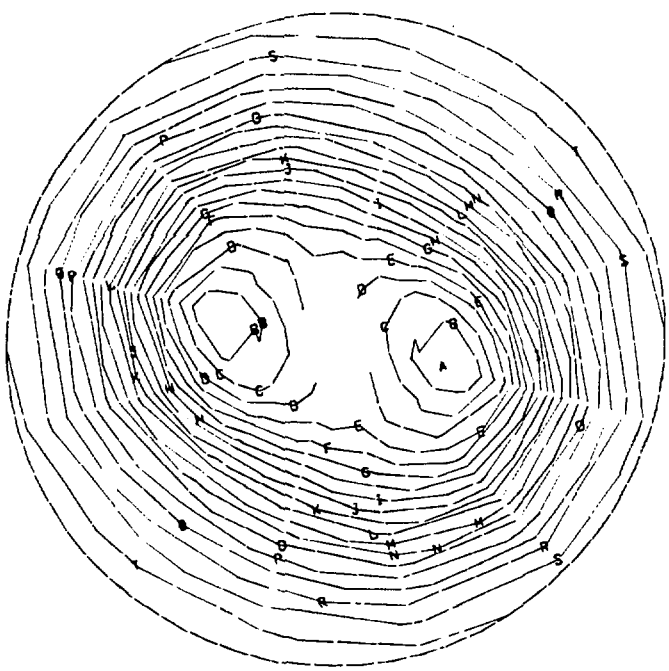

IDENTIFICATION	CONTOUR VALUE
A A A A	-1.535E+10
B B B B	-1.485E+10
C C C C	-1.435E+10
D D D D	-1.385E+10
E E E E	-1.335E+10
F F F F	-1.285E+10
G G G G	-1.235E+10
H H H H	-1.185E+10
I I I I	-1.135E+10
J J J J	-1.085E+10
K K K K	-1.035E+10
L L L L	-9.849E+09
M M M M	-9.349E+09
N N N N	-8.849E+09
O O O O	-8.349E+09
P P P P	-7.849E+09
Q Q Q Q	-7.349E+09
R R R R	-6.849E+09
S S S S	-6.349E+09
T T T T	-5.849E+09
U U U U	-5.349E+09

$t = 1.64 \times 10^5$ yrs
b

Gravitational Potential(ergs/g)
FIGURE 84